

**NAVAL POSTGRADUATE SCHOOL**  
**Monterey, California**



19980414 127

**THESIS**

**DTIC QUALITY INSPECTED 4**

**COMPARISON OF LOS ALAMOS NATIONAL  
LABORATORY (LANL) PARALLEL OCEAN  
PROGRAM (POP) MODEL FIELDS WITH  
PACIFIC SURFACE DRIFTER  
MEASUREMENTS**

by

Michael R. Lemon

September, 1997

Thesis Advisor:

Julie L. McClean

Thesis Co-advisor:

Jeffrey D. Paduan

**Approved for public release; distribution is unlimited.**

# REPORT DOCUMENTATION PAGE

Form Approved OMB No. 0704-0188

Public reporting burden for this collection of information is estimated to average 1 hour per response, including the time for reviewing instruction, searching existing data sources, gathering and maintaining the data needed, and completing and reviewing the collection of information. Send comments regarding this burden estimate or any other aspect of this collection of information, including suggestions for reducing this burden, to Washington Headquarters Services, Directorate for Information Operations and Reports, 1215 Jefferson Davis Highway, Suite 1204, Arlington, VA 22202-4302, and to the Office of Management and Budget, Paperwork Reduction Project (0704-0188) Washington DC 20503.

1. AGENCY USE ONLY (Leave blank)	2. REPORT DATE September 1997	3. REPORT TYPE AND DATES COVERED Master's Thesis	
4. TITLE AND SUBTITLE COMPARISON OF LOS ALAMOS NATIONAL LABORATORY (LANL) PARALLEL OCEAN PROGRAM (POP) MODEL FIELDS WITH PACIFIC SURFACE DRIFTER MEASUREMENTS		5. FUNDING NUMBERS	
6. AUTHOR(S) Michael R. Lemon			
7. PERFORMING ORGANIZATION NAME(S) AND ADDRESS(ES) Naval Postgraduate School Monterey CA 93943-5000		8. PERFORMING ORGANIZATION REPORT NUMBER	
9. SPONSORING/MONITORING AGENCY NAME(S) AND ADDRESS(ES)		10. SPONSORING/MONITORING AGENCY REPORT NUMBER	
11. SUPPLEMENTARY NOTES The views expressed in this thesis are those of the author and do not reflect the official policy or position of the Department of Defense or the U.S. Government.			
12a. DISTRIBUTION/AVAILABILITY STATEMENT Approved for public release; distribution is unlimited.		12b. DISTRIBUTION CODE	
13. ABSTRACT (maximum 200 words) Model fields from the Los Alamos National Laboratory (LANL) Parallel Ocean Program (POP) 1/6 degree global circulation model are compared to measurements from over 1300 satellite-tracked surface drifters that were deployed in the tropical Pacific (20N to 20S), between 1979 and 1994, during the TOGA Pan-Pacific Current Study. Geographic averages of 5-day averaged drifter velocity estimates for 2-deg. latitude x 8-deg. longitude bins are compared to similarly binned 3-day model snapshots from September 1992 to October 1994. Eulerian comparisons of the model mean velocities and their observed counterparts show that the model u mean is slightly higher in the equatorial region, while the model v mean is 50% greater in this region. Model SST mean values are 20% less than observed values in the eastern equatorial Pacific. Model variability is about 20% less than the observed quantity in equatorial regions, and 50% less poleward of 10S and 10N. Both model and observed velocity and SST covariance fields imply a net heat convergence toward the equator with the largest values in the region of instability waves north of the equator. Model velocity fields are used to produce simulated Lagrangian trajectories for uniform and non-uniform deployment strategies. Autocorrelation, time and length scales, diffusivity, and polarization are calculated and ensemble-averaged by 5 deg. latitude bands for comparison with drifter-based Lagrangian statistics. Time and length scales are too long and diffusivities too low compared to observations, but data sampling in the simulated fields was biased by trajectories that overlap current regimes. These differences, in both Eulerian and Lagrangian comparisons, may be related to the lack of a surface mixed layer, inadequate representation of wind forcing, still too coarse grid resolution, and deficiencies in simulating the mean structure of the density field in the model. They are also partly related to lack of weighted averages to account for non-uniform drifter sampling.			
14. SUBJECT TERMS numerical modeling, surface drifters, tropical Pacific		15. NUMBER OF PAGES 127	16. PRICE CODE
17. SECURITY CLASSIFICATION OF REPORT Unclassified	18. SECURITY CLASSIFICATION OF THIS PAGE Unclassified	19. SECURITY CLASSIFICATION OF ABSTRACT Unclassified	20. LIMITATION OF ABSTRACT UL

NSN 7540-01-280-5500

Standard Form 298 (Rev. 2-89)  
Prescribed by ANSI Std. Z39-18 298-102



Approved for public release; distribution is unlimited.

**COMPARISON OF LOS ALAMOS NATIONAL LABORATORY (LANL)  
PARALLEL OCEAN PROGRAM (POP) MODEL VELOCITY FIELDS  
WITH PACIFIC SURFACE DRIFTER MEASUREMENTS**

Michael R. Lemon  
Lieutenant, NOAA Corps  
B.S., Humboldt State University, 1986

Submitted in partial fulfillment  
of the requirements for the degree of

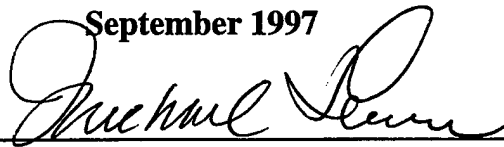
**MASTER OF SCIENCE IN PHYSICAL OCEANOGRAPHY**

from the

**NAVAL POSTGRADUATE SCHOOL**

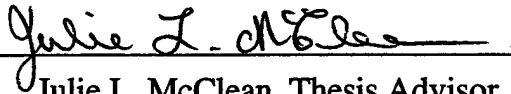
**September 1997**

Author:

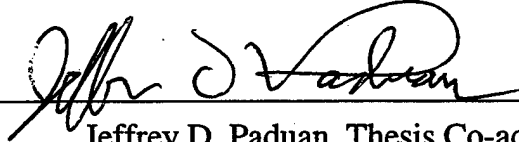


Michael R. Lemon

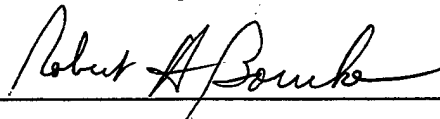
Approved by:



Julie L. McClean, Thesis Advisor



Jeffrey D. Paduan, Thesis Co-advisor



Robert H. Bourke, Chairman, Department of Oceanography



## ABSTRACT

Model fields from the Los Alamos National Laboratory (LANL) Parallel Ocean Program (POP)  $1/6^\circ$  global circulation model are compared to measurements from over 1300 satellite-tracked surface drifters that were deployed in the tropical Pacific ( $20^\circ\text{N}$  to  $20^\circ\text{S}$ ), between 1979 and 1994, during the TOGA Pan-Pacific Current Study. Geographic averages of 5-day averaged drifter velocity estimates for  $2^\circ$  latitude  $\times$   $8^\circ$  longitude bins are compared to similarly binned 3-day model snapshots from September 1992 to October 1994.

Eulerian comparisons of the model mean velocities and their observed counterparts show that the model  $u$  mean is slightly higher in the equatorial region, while the model  $v$  mean is 50% greater in the this region. Model SST mean values are 20% less than observed values in the eastern equatorial Pacific. Model variability is about 20% less than the observed quantity in equatorial regions, and 50% less poleward of  $10^\circ\text{S}$  and  $10^\circ\text{N}$ . Both model and observed velocity and SST covariance fields imply a net heat convergence toward the equator with the largest values in the region of instability waves north of the equator.

Model velocity fields are used to produce simulated Lagrangian trajectories for uniform and non-uniform deployment strategies. Autocorrelation, time and length scales, diffusivity, and polarization are calculated and

ensemble averaged by  $5^\circ$  latitude bands for comparison with drifter-based Lagrangian statistics. Time and length scales are too long and diffusivities are too low compared to observations, but data sampling in the simulated fields was biased by trajectories that overlap current regimes.

These differences, in both Eulerian and Lagrangian comparisons, may be related to the lack of a surface mixed layer, inadequate representation of wind forcing, still too coarse grid resolution, and deficiencies in simulating the mean structure of the density field in the model. They are also partly related to lack of weighted averages to account for non-uniform drifter sampling.

## TABLE OF CONTENTS

I.	INTRODUCTION.....	1
II.	OVERVIEW OF TROPICAL PACIFIC OCEAN CIRCULATION: MEAN AND VARIABILITY.....	5
III.	MODEL OUTPUT AND DRIFTER DATA SET.....	13
	A. MODEL DESCRIPTION.....	13
	1. Computational Grid.....	13
	2. Initialization and Forcing.....	14
	3. Output Fields.....	15
	4. Inertial Oscillations and Aliasing.....	15
	5. Previous POP Studies.....	16
	B. DRIFTER DATA SET.....	19
	1. Satellite-Tracked Drifter Description.....	19
	2. Temporal and Spatial Extent of Data.....	20
	3. Sources of Error.....	20
	4. Relevant Drifter Studies.....	22
IV.	EULERIAN RESULTS.....	31
	A. MEAN FIELDS.....	31
	1. Mean Zonal Velocity.....	31
	2. Mean Meridional Velocity.....	32
	3. Mean Velocity Vectors.....	34
	4. Mean SST.....	35
	B. VARIABILITY.....	36
	1. Variability of Zonal Velocity.....	36
	2. Variability of Meridional Velocity.....	37
	3. Variability of Total (u and v) Velocity.....	38
	4. Variability of SST.....	39
	C. DIVERGENCE AND RELATIVE VORTICITY.....	39
	1. Divergence.....	39
	2. Relative Vorticity.....	41
	D. COVARIANCE FIELDS.....	41
	1. Covariance of u and v: $\langle u'v' \rangle$ .....	41
	2. Covariance of Velocity and SST.....	42
V.	LAGRANGIAN STATISTICS.....	57
	A. LAGRANGIAN AUTOCOVARIANCE.....	59
	B. INTEGRAL TIME AND LENGTH SCALES.....	61
	C. DIFFUSIVITY.....	63
	D. POLARIZATION.....	65
VI.	CONCLUSIONS AND RECOMMENDATIONS.....	97
	A. CONCLUSIONS.....	97
	B. RECOMMENDATIONS.....	100
	APPENDIX. RUNGE-KUTTA METHOD OF TRAJECTORY GENERATION.....	105
	LIST OF REFERENCES.....	111
	INITIAL DISTRIBUTION LIST.....	115



## ACKNOWLEDGEMENT

The drifter data used in this analysis was collected as part of the World Ocean Circulation Experiment (WOCE) Pan-Pacific Current Study. The model output was originally produced by the Los Alamos National Laboratory (LANL) Advanced Computing Center for comparison with TOPEX/POSEIDON, and was generously made available by Dr. Richard Smith. Thanks to Dr. Peter Niiler and Sharon Lukas of Scripps Institution of Oceanography for providing the drifter data and aiding in its interpretation, and to Dr. Matt Maltrud of LANL for helpful discussions with the model output. This research was supported by NSF grant OCE-9633049 and by the CHAMMP (Computer Hardware, Advanced Mathematics, Model Physics) program of the US Department of Energy.

I would like to express my sincere gratitude and appreciation to my thesis co-advisors, Dr. Julie L. McClean and Dr. Jeffrey D. Paduan, for their support, encouragement, and involvement. Other members of the Oceanography Department faculty I would like to thank and recognize are Dr. Wieslaw Maslowski, Dr. Pierre-Marie Poulain, Dr. Bert Semtner, Dr. Robin Tokmakian, and Dr. Yuxia Zhang, for advice and assistance. I am particularly indebted to Mike Cook, of the Oceanography Department staff, for his generosity and patience. Special thanks to Pete Braccio and Arlene Bird of the Oceanography Department staff, and to Eldor Magat, Hiram

Cooke, and Dr. Matthew Koebe of the Computer Center staff.

Finally, I am most appreciative of my wife, Maryann, and my sons, Kyle and Elias, for their support and patience.

## I. INTRODUCTION

High-resolution eddy-resolving models have shown increasing realism over the past decade, contributing to our understanding of ocean circulation and its variability (Hurlburt et al., 1992; Semtner and Chervin, 1992; Smith et al., 1992; Bryan et al., 1995; Bleck et al., 1995; Semtner 1997; Maltrud et al., 1997). Validation of these models is obtained by comparing the model output with high-quality data sets, such as those collected during the World Ocean Circulation Experiment (WOCE) and from satellites. Prior to, and during WOCE, reliable surface drifter technology in the Pacific Ocean has produced current and temperature measurements over spatial and temporal scales sufficient for statistical comparisons with high resolution models, providing a measure of the model's ability to reproduce the observed mean flow and variability (Niiler et al., 1997).

In the Pacific, surface drifter measurements have been collected by several investigators over the past two decades. In the early eighties, McNally (1981, 1983) deployed drifters in the mid-latitudes of the North Pacific, while Hansen and Paul (1984) used them to study currents associated with barotropic instability waves in the eastern equatorial Pacific.

In 1987, as part of the Tropical Ocean and Global Atmosphere (TOGA) Program, surface drifters were deployed

across the entire Tropical Ocean basin to directly measure the circulation of the tropical Pacific, and to investigate temporal variability over scales from intraseasonal to interannual. This *Pan-Pacific Current Study* (Niiler et al., 1997) became part of the WOCE program objective to deploy several thousand drifters worldwide, providing a global surface data set of sea surface temperature, velocity, and atmospheric pressure. The study involved the deployment of over 1300 satellite-tracked surface drifting buoys, drogued to 15 m, in the tropical Pacific between January 1988 and December 1994, between 20°S and 20°N. The data set spans the 1991-92-93 El Niño, the 1988 La Niña, and three normal seasonal cycles. This data set was used for both Eulerian and Lagrangian analyses, and has been characterized as appropriate for comparison with OGCM's of the tropical Pacific which have been forced with 1988-1994 atmospheric fluxes.

Key studies of surface drifter tracks conducted from this data set, using Lagrangian statistical analyses, include a description of the seasonal variability of the equatorial Pacific, in Reverdin et al. (1994), and the interannual variability of the equatorial Pacific, in Frankignoul et al. (1996). Studies of this data set using Eulerian analysis include Niiler et al., (1997), and estimates of horizontal divergence and vertical velocity in the equatorial Pacific, presented in Poulain (1993).

The objective of this study is to calculate and compare the observed Eulerian and Lagrangian drifter statistics from the tropical Pacific with those from the Los Alamos National Laboratory (LANL) Parallel Ocean Program (POP) model. Eulerian averages in  $2^\circ$  latitude by  $8^\circ$  longitude sub-regions are compared directly, while a fourth-order Runge-Kutta scheme is used to generate trajectories from model velocity fields, from which Lagrangian statistics are calculated and related to their drifter-based counterparts. Comparison results are used to characterize inconsistencies for further model refinement.

This study is organized as follows. An overview of the tropical Pacific is presented in Section II. Descriptions of the drifter data set and model output, along with background summaries of model and drifter investigations are presented in Section III. Drifter and model comparisons of time mean circulation, temperature fields, and variability are presented in Section IV. Section V describes temporal and spatial scales, measures of angular momentum and polarization, and diffusivities as a result of Lagrangian statistics. Section VI presents conclusions and recommendations.



## II. OVERVIEW OF TROPICAL PACIFIC OCEAN CIRCULATION: MEAN AND VARIABILITY

To familiarize the reader with the area of the ocean studied, and as a basis for understanding later results, an overview of the observed mean circulation and its variability in the tropical Pacific Ocean ( $20^{\circ}\text{S}$  to  $20^{\circ}\text{N}$ ) is presented.

The mean zonal surface circulation of the tropical Pacific Ocean is characterized by alternating bands of eastward- and westward-flowing currents (Figure 1) which are forced by the large-scale wind field. The North Equatorial Current (NEC) and South Equatorial Current (SEC) form the equatorward arms of the subtropical gyres, and flow westward in the general area of the northern and southern Trades (Figure 2), respectively. Between these two currents ( $3^{\circ}\text{N}$  to  $10^{\circ}\text{N}$ ), the eastward flowing North Equatorial Countercurrent (NECC) is observed to flow counter to the prevailing winds. Also flowing eastward is the subsurface Equatorial Undercurrent (EUC). The major part of the NEC curves to the northwest at about  $150^{\circ}\text{E}$ , past the Phillipines and Taiwan, to eventually feed the western boundary, the Kuroshio Current. The SEC, extending from about  $3^{\circ}\text{N}$  to  $10^{\circ}\text{S}$ , flows from South America to the western Pacific; as it approaches Australia, the SEC bifurcates near  $18^{\circ}\text{S}$ , with the southern branch feeding the East Australia Current and the northern branch continuing through the Solomon Sea, crossing into the

Northern Hemisphere to feed the NECC and the EUC in the western tropical Pacific (Figure 3). A weak, eastward flowing South Equatorial Countercurrent (SECC) usually exists west of the International Dateline (IDL) at about  $10^{\circ}\text{S}$ .

The NEC and SEC are directly wind-driven and are therefore strongly seasonal, reaching maximum velocity during winter in their respective Hemispheres. In the mid-Pacific, the major part of the NEC lies between about  $8^{\circ}\text{N}$  to  $20^{\circ}\text{N}$ , and carries about 45 Sv with a maximum speed of about 0.3 m/s in February. The SEC is strongest in August, at about 0.6 m/s, with a transport of about 27 Sv, decreasing to 7 Sv in February. The NECC varies seasonally in strength and position. From February to April the northwest monsoon prevents the SEC from feeding the NECC, so that the NECC is restricted to  $4^{\circ}\text{N}$  to  $6^{\circ}\text{N}$  with a volume transport of 15 Sv and maximum speeds below 0.2 m/s. East of  $110^{\circ}\text{W}$  the NECC disappears altogether. From May to January the NECC flows between  $5^{\circ}\text{N}$  and  $10^{\circ}\text{N}$  with speeds of 0.5 m/s. The annual mean transport of the NECC decreases uniformly with longitude, from 45 Sv west of  $135^{\circ}\text{E}$  to 10 Sv east of the Galapagos Islands. Maximum velocities of the SECC occur during the Northwest Monsoon (the cause of the wind stress minimum, February to April). Typical surface speeds are below 0.3 m/s at  $170^{\circ}\text{E}$ , yielding a transport of about 10 Sv. In both Monsoon seasons the strength of the SECC decreases rapidly east of the IDL, and may be altogether absent from the

eastern Pacific (Tomczak and Godfrey, 1994).

Mean meridional circulation in the tropical Pacific is driven by poleward Ekman drift in the surface layers and equatorward motion at the depth of the thermocline. This circulation implies equatorial upwelling which can be measured from the divergence of the horizontal currents as measured with satellite tracked drifters (Philander, 1990).

With the exception of a band of relatively warmer surface water in the eastern tropical Pacific, just north of the equator, mean sea surface temperatures (SST) are higher in the western tropical Pacific than in the east. The eastward flow of the NECC coincides with this band of warmer surface water in the eastern Pacific. SST in the eastern tropical Pacific are at a maximum during the northern spring, when the trade winds relax, and are at a minimum during the northern summer and fall when the trades are strongest (Apel, 1987). The expanse of very warm water in the western equatorial region has annual mean values exceeding  $29.5^{\circ}\text{C}$  between New Guinea and the Solomon Islands. Annual means above  $29.0^{\circ}\text{C}$  occur between about  $10^{\circ}\text{N}$  and  $5^{\circ}\text{S}$ , in the vicinity of the Solomon Sea, and extend eastward to about  $170^{\circ}\text{W}$ . The thermal equator follows the Intertropical Convergence Zone (ITCZ) from  $5^{\circ}\text{N}$  in the west to about  $15^{\circ}\text{N}$  in the east, with annual means of about  $27^{\circ}\text{C}$ . (Tomczak and Godfrey, 1994).

Variability relevant to this study spans temporal scales

from intraseasonal to interannual. The interannual perturbation of the ocean-atmosphere known as the El Niño Southern Oscillation (ENSO) is a major component of the tropical Pacific variability, and is initiated by reversals of the easterly Trade winds in the western Pacific. These westerly wind bursts produce reversals of the westward flowing SEC across the basin. West of the dateline the reversals are in response to direct wind forcing while to the east they are caused by the passage of remotely wind-forced equatorial Kelvin waves with phase speeds of 2-3 m/s (McPhaden, 1993). These surface flows produce an eastward expansion of the western Pacific warm pool; the redistribution of warm water zonally flattens the east-west slope of the thermocline, weakening the baroclinic zonal pressure gradient and the EUC driven by it. ENSO tends to be phase locked to the annual cycle, with the largest SST anomalies occurring over the equatorial cold tongue region in the month of December (Yang et al., 1977).

The intraseasonal variability addressed here spans temporal scales of 20 to 100 days, typified by barotropic and baroclinic instabilities associated with shear zones. The weakening or disappearance of the EUC impacts the generation of 20- to 30-day barotropic instability waves that are normally generated in the shear zone between the northern flank of the EUC and the SEC. These waves have westward phase velocity, wavelengths of about 1000 km, and have been

documented along 5°N in the shear zone between the SEC and the NECC by Perigaud (1990) using Geosat data. Westward propagating waves were documented with periods of 50-90 days and wavelengths of 630-950 km, along 12°N, in the shear zone between the NECC and the NEC, using the same data set.

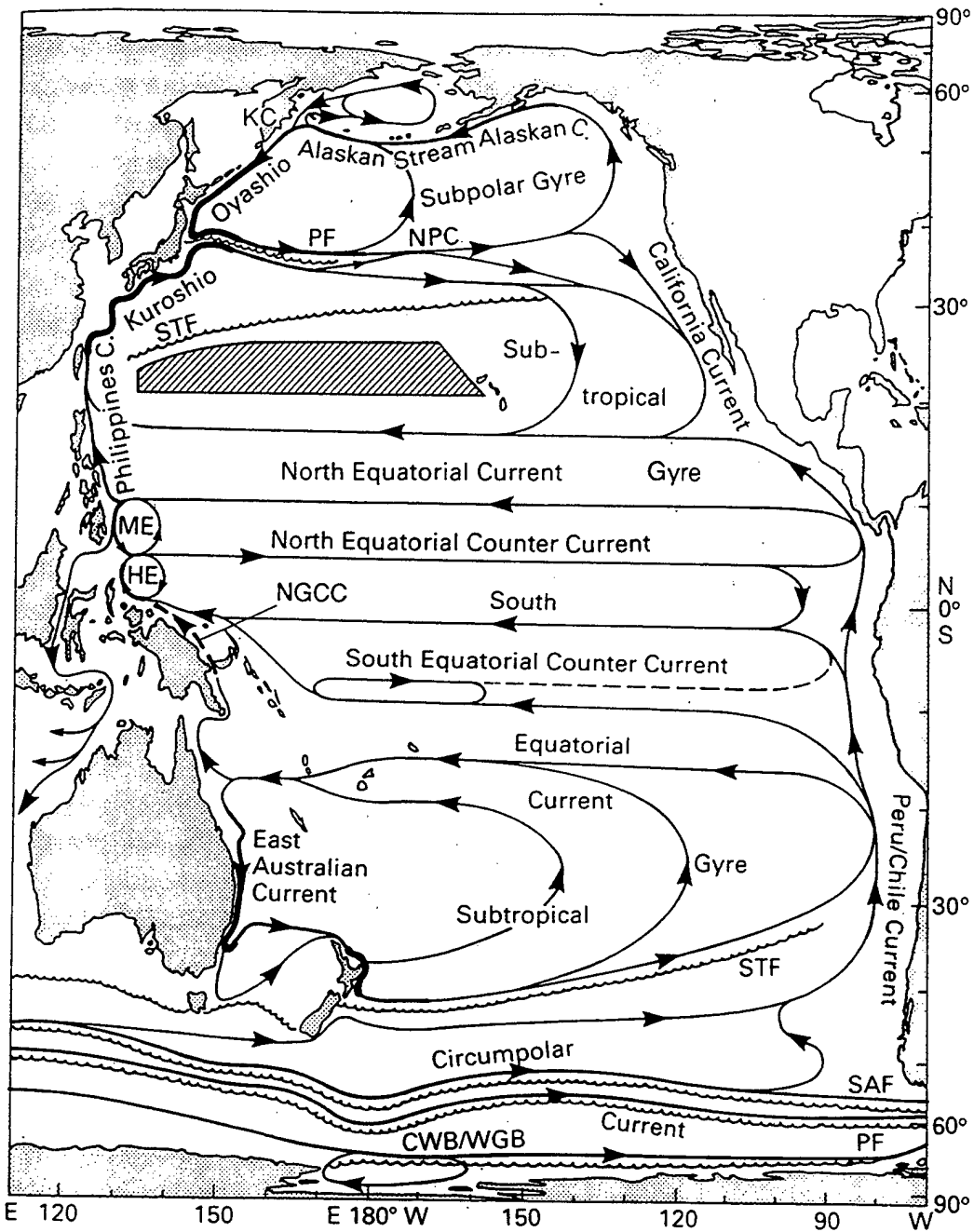


Figure 1. Schematic of the surface currents of the Pacific Ocean. Abbreviations used in the area of study: Mindanao Eddy (ME), Halmahera Eddy (HE), and New Guinea Coastal Current (NGCC). Figure 8.6 from Tomczak and Godfrey (1994).

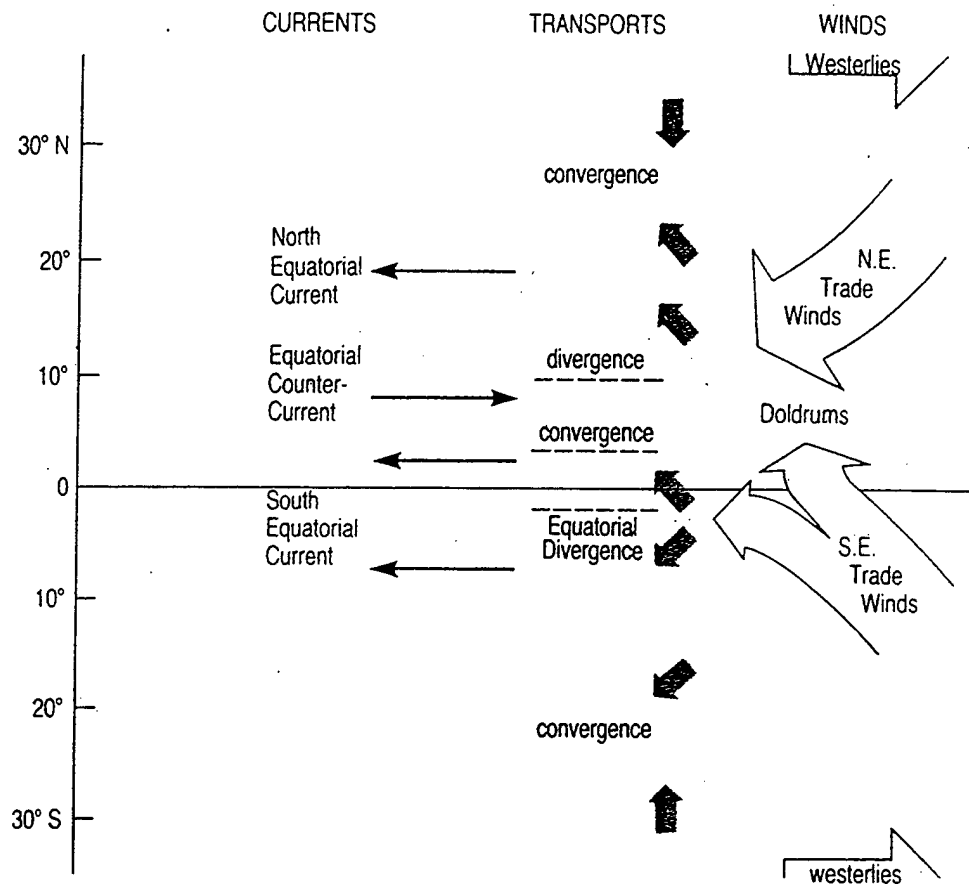


Figure 2. Schematic of the relationships between the wind direction, surface current, and the Ekman transport (total transport in the wind-driven layers, shown by short arrows), in equatorial latitudes. Figure 5.1(a) from *Ocean Circulation*, G. Bearman, ed., 1996.

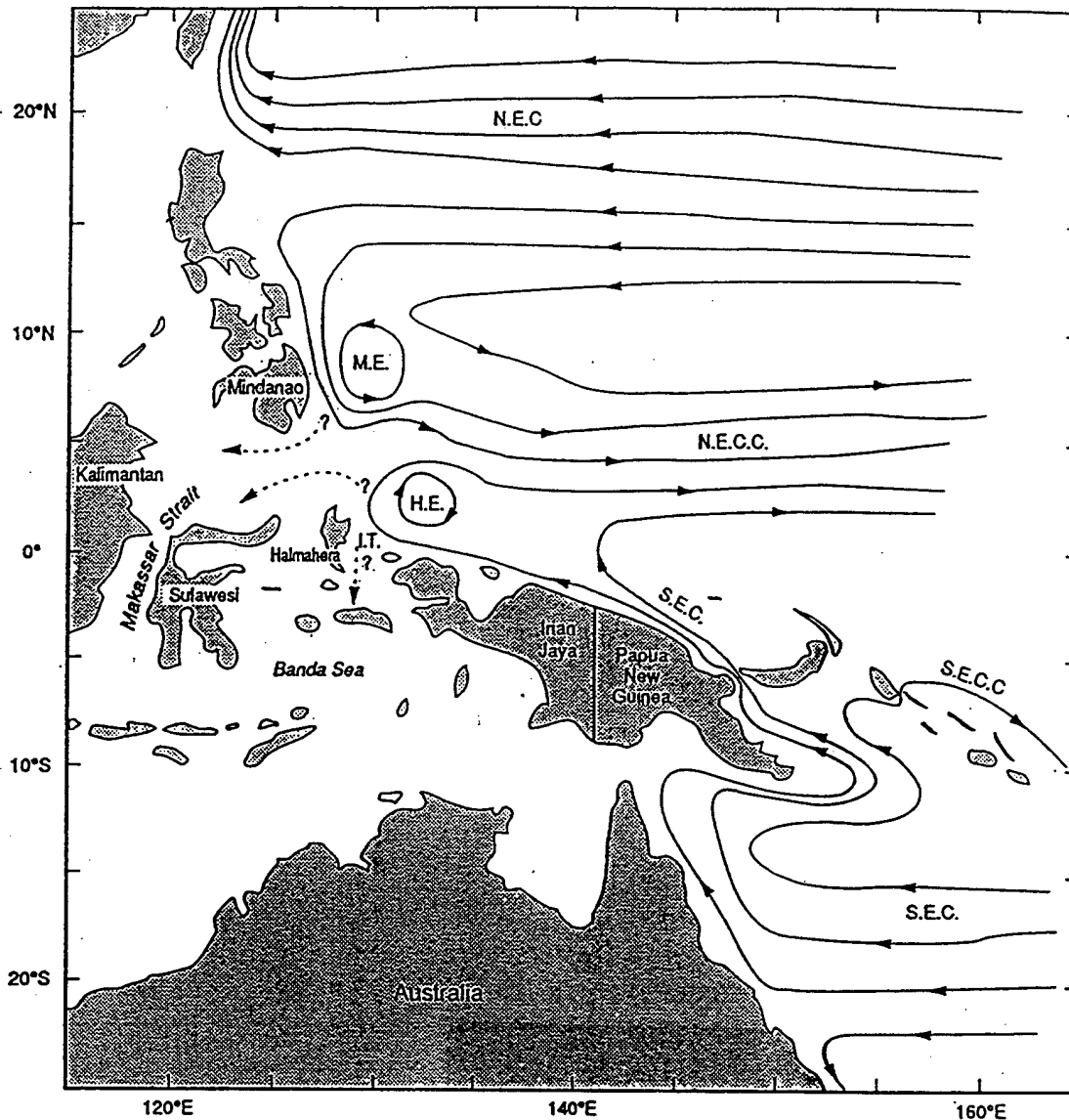


Figure 3. Schematic of the surface currents of the western tropical Pacific. Abbreviations used: North Equatorial Current (NEC), South Equatorial Current (SEC), North Equatorial Countercurrent (NECC), South Equatorial Countercurrent (SECC), Halmahera Eddy (HE), and Mindanao Eddy (ME). Possible sources of the Indonesian Throughflow (IT) are shown as dotted lines. Figure 1 from Godfrey et al. (1993).

### III. MODEL OUTPUT AND DRIFTER DATA SET

#### A. MODEL DESCRIPTION

Model fields are obtained from the LANL  $1/6^\circ$  global POP simulation, an eddy-resolving, z-level primitive equation model with active thermohaline dynamics (Maltrud et al., 1997). Smith et al. (1992) restructured the global,  $1/2^\circ$  Semtner and Chervin (1988) model derived from Bryan's (1969) formulation and versions by Cox (1970, 1984) and Semtner (1974), for a massively parallel Connection Machine 5 at LANL and configured it for a  $1/6^\circ$  grid. Dukowicz and Smith (1994) added an implicit free-surface formulation of the barotropic mode. A full description of the model formulation can be found in Maltrud et al. (1997); here only relevant details will be given.

##### 1. Computational Grid

To better track eddy length scales in this high resolution global simulation, a Mercator grid with 1280 longitudinal and 896 latitudinal points was employed. The longitudinal spacing was  $0.28^\circ$  and the latitudinal spacing equals the longitudinal spacing times the cosine of the latitude, producing a square grid over the global domain between  $77^\circ\text{S}$  to  $77^\circ\text{N}$ . The resolution ranged from about 31 km at the equator to just over 6.5 km at the highest latitudes, which on average, is  $0.17$  or  $1/6^\circ$ . The model has 20 non-

uniformly spaced vertical levels; the uppermost is 25 m deep, increasing to 550 m at the lowest level.

## **2. Initialization and Forcing**

POP was initialized using output interpolated from the end of a 3-year Semtner (1997)  $1/4^\circ$  run (January 1988), which in turn, had been initialized with results from an integration of 35 years from Levitus (1982) at  $1/2^\circ$  and a further 5-year equilibrium run at  $1/4^\circ$ . POP then equilibrated for 5 years at the higher resolution, after which a 9-year run was completed. A density field from the end of this first POP run was used to initialize POP7, the simulation used in this thesis. POP7 was forced with 3-day averaged wind stresses derived from European Center for Medium Range Forecasting (ECMWF) winds from 1985-1994 (1000-mb winds from 1985-1989 and 10-m winds from 1990-1994). Temperature and salinity in the upper level of the model were restored to Levitus (1982) climatology with a restoring timescale of 30 days. Very realistic topography (ETOPO5) was employed. Biharmonic horizontal friction whose coefficients have a latitudinally decreasing form to take advantage of the square Mercator grid, and vertical mixing according to Pacanowski and Philander (1981) were used.

### **3. Output Fields**

Extracted model fields are 3 - day snapshots of zonal velocity ( $u$ ), meridional velocity ( $v$ ), and temperature ( $T$ ), for the period September 1992 to October 1994. High-frequency velocities were available for this period alone; only monthly averages were saved for the rest of the run. Fields were extracted from 112°E to 72°W, 21°S to 21°N, to coincide with the region from which the Pacific Ocean surface drifter measurements were collected. The resultant analysis grid has 655, 152, and 1 cells in longitude, latitude, and depth, respectively. Model output is filtered and binned into 2° latitude x 8° longitude areas for comparison with the drifter data.

### **4. Inertial Oscillations and Aliasing**

Forcing of high-resolution primitive-equation models with realistic, high frequency (period order of days) wind-stress fields produce inertial oscillations. Subsampling model output at intervals of several days leads to aliasing of these inertial currents into lower frequencies that vary with latitude (Jayne and Tokmakian, 1997). Three-day wind-stress averaging and the use of 3-day snapshots both contributed to the aliased signal in the POP output. Replacing the daily winds averaged over three days with daily winds interpolated to every timestep, and using three-daily averages rather than three-daily snapshots increased the

model energy levels (R. Tokmakian, personal communication). Saving values of the prognostic variables at every time step and then averaging every three days avoids aliasing inertial oscillations (Jayne and Tokmakian, 1997). Running another simulation, however, is not realistic, so the application of a 9-day running mean is used to make the output serviceable, removing much of the spurious energy associated with the inertial motions. Figure 4 (R. Tokmakian, personal communication) shows the power spectrum of the  $u$  component of velocity, from the original and averaged runs, sampled at the local minima of the forcing function at  $14.84^{\circ}\text{N}$  and  $14.84^{\circ}\text{S}$ , along  $160^{\circ}\text{W}$ . At these latitudes, the period of the inertial oscillations is aliased to a period longer than the Nyquist frequency of the output data. Most noticeable is the difference in energy between the 3-day snapshot and 3-day average at periods less than 10 days. To remove much of this aliased signal, instantaneous 3-day snapshots were filtered using a 9-day running average. Figure 5 (R. Tokmakian, personal communication) shows the reduction in amplitude of both signals at periods of less than 10 days, with much of the aliased material removed, after application of the 9-day running filter to the 3-day snapshots.

## **5. Previous POP Studies**

Previous relevant investigations and validation studies have shown the robustness of this model version. Fu and Smith

(1996) focus on the comparison of model results with TOPEX, while McClean et al. (1996) compare model results with TOPEX, as well as the Semtner-Chervin  $1/4^\circ$  model. Maltrud et al. (1997) examined mean circulation and variability in the model, with the effects of monthly varying and daily varying winds.

Fu and Smith (1996) studied comparisons of the mean circulation, the mesoscale variability, the amplitude and phase of the annual cycle, as well as intraseasonal and interannual changes, and showed that the simulations and observations agree fairly well over a broad range of spatial and temporal scales. The sea level variance, however, produced by the model is generally less than the model by a factor of 2, primarily in the eddy-rich regions. The authors conclude that even higher resolution is needed to fully resolve the mesoscale eddies.

Maltrud et al. (1997) state that many features of the wind-driven circulation are well simulated by POP and are relatively independent of various surface forcings applied. Surface current patterns from sea surface mean heights, and overall transports from the stream function of volume transport, are very realistic over most of the ocean, with the strongest simulated currents having width scales and core speeds comparable to their real counterparts. The authors cite very good agreement with observations of the Antarctic Circumpolar Current and the Pacific Equatorial Undercurrent,

and the data in the equatorial Pacific regime in general. Z-level models have typically had problems with the equatorial undercurrent due to vertical shear, but a meridional section of the zonal velocity at 150°W (Figure 6), shows the undercurrent and alternating jets decreasing in strength with depth. This good agreement in vertical shear, where previous simulations were problematic, as well as in horizontal circulation, are encouraging features in the model simulation of the equatorial Pacific.

McClellan et al. (1996), in descriptions of the spatial distribution of energy relative to T/P, concentrated upon statistical intercomparisons of mesoscale variability of T/P altimeter data, the 1/4° Semtner-Chervin model, and the 1/6° LANL POP model; independent comparisons were made with drifter data in the tropics. Model results are in rough agreement with the T/P field in terms of spatial variability, with the best agreement in magnitudes in areas of strong currents, such as western boundary currents. Moderate variability is seen several degrees north and south of the equator in the Pacific, attributed to 20- to 30-day instability waves. Between 15°N and 15°S, drifter rms velocity field values are in close agreement with POP values, with drifter values exceeding total model velocities by a factor of 2 in the mid-latitudes.

## **B. DRIFTER DATA SET**

Under the sponsorship of the Tropical Ocean and Global Atmosphere (TOGA) Program of the World Climate Research Program (WCRP), over 1300 satellite-tracked surface drifters were released between January 1979 and May 1994 in the tropical Pacific (20°N to 20°S) to observe surface currents and SST patterns across the entire basin (Niiler et al., 1997). Figure 7 indicates the frequency distribution of the number of five-day drifting buoy velocity observations as a function of year, showing the concentration in the years 1992-1993. Later in this time period, these data include instruments deployed as part of the WOCE Surface Velocity Program. Today the WOCE and TOGA programs and their follow-on programs using similar drifters are referred to as the Global Drifter Program (GDP), managed by NOAA/AOML in Miami.

### **1. Satellite-Tracked Drifter Description**

The GDP drifters were drogued to 15 m depth in order to occupy the middle of the summer mixed layer and to lie below the daily thermocline and associated rotational currents, and were tracked to within a 300 m radius by Service ARGOS. A linear SST sensor accurate to 0.1°C is located on the lower half of the surface float. The drifter is fitted with a submergence sensor which allows the drogue status to be determined (drifter floats rarely submerge without drogues). Drifter technical specifications and manufacturing procedures

are described in Sybrandy and Niiler (1991).

## **2. Temporal and Spatial Extent of the Data**

The drifter data span the 1991-92-93 El Niño and the 1988 La Niña; other variabilities include contributions from seasonal cycles, and eddy and equatorial wave motions of periods longer than 10 days. The data used in this study consists of 5-day-average drifter velocities binned to 2° latitude by 8° degrees longitude.

Concentration of tracks across the tropical Pacific (Figure 8) is more a function of the circulation than location of release. Niiler et al. (1997) note that the measured circulation is the horizontal circulation of a three-dimensional flow, where the meridional and vertical velocity components play as significant a role as the mean zonal flows. Drifters deployed near the Equator generally moved to higher latitudes in response to mean Ekman divergences, which are not present in dynamic topography. Data density was not spatially uniform, as the drifters spent about twice as much time in convergent regions, such as the southern margin of the NECC, than at the Equator.

## **3. Sources of Error**

Error sources in constructing current fields from drifter data are from ARGOS position errors, the fidelity with which the buoys measure water movement (McNally, 1981),

and the variability inherent in mesoscale perturbations (Hansen and Paul, 1984; Poulain and Niiler, 1989). Niiler et al. (1995) established the drifter slip for tropical, GDP-style drifters, to be within 1 cm/sec in winds of 10 m/sec; drifter data used here have not been corrected for wind induced slip because the mean wind speeds in the tropical Pacific are less than 10 m/sec (Niiler et al., 1997). Service ARGOS has consistently provided excellent positioning, though expensive, with uncertainty of less than 500 m (Poulain and Niiler (1989); this data set has an estimated accuracy of 300 m (Niiler et al. 1997). The greater uncertainty associated with these data is that drifters do not provide a random sampling of currents since drifter deployment is not random in space or time, and the mean current near the equatorial divergence creates data sparse regions (Niiler et al., 1997; Poulain 1993; Reverdin et al., 1994). This data error is not estimated here, but we investigate this issue by comparing different sets of model-derived trajectories where we can control the initial distribution.

Since water parcels in a non-diffusive medium move on  $\sigma_t$  surfaces and surface drifters on isobaric surfaces, trajectories of buoyant floats are not strictly Lagrangian (Fieux et al., 1994; Freeland et al., 1975; Poulain and Niiler, 1989). Diffusivity effects can induce uncertainty, particularly in drifter deployments of long duration.

Uncertainties also occur in interpretation of mean flow information from ensemble averaged float velocities. Time-averaged flow over large areas is equal to the instantaneous average over many widely dispersed floats, if the turbulence is homogeneous and stationary. But if the eddy intensity varies in space, the center of mass of the float cluster will ascend the energy gradient to yield an inaccurate measure of mean flow (Freeland et al., 1975). This leads to apparent mean velocities if data concentration is not uniform and has been termed array bias (Davis et al., 1996).

#### **4. Relevant Drifter Studies**

The use of surface floats for measuring current systems has become increasingly common as an effective method to measure surface circulation, as a complement to other observations, and as a method to refine numerical models with direct observations. A selection of drifter studies relevant to the area of study, model output domain, analysis methods, and dynamics involved is outlined here.

Investigations into Pacific surface flow using Lagrangian surface floats include Hansen and Paul (1984), with estimates of equatorial divergence in the eastern tropical Pacific from drifter-derived measurements of surface currents, and McNally (1981) in the northeastern Pacific. McNally et al. (1983) used the trajectories of 16 satellite-tracked drifting buoys and derived velocities to construct a

Lagrangian perspective of the near-surface circulation of the North Pacific subtropical gyre. Paduan and Niiler (1993), using Lagrangian surface drifters, report on the general nature of the large spatial scale and seasonal timescale currents and temperatures obtained from the drifters, and calculate the large-scale spatial convergence of heat in the northeast Pacific Ocean. Poulain (1993) presents estimates of horizontal divergence and vertical velocity in the equatorial Pacific, and Poulain and Niiler (1989) describe the statistical analysis of drifter motion in the eastern Pacific. Ralph and Niiler (1995) discuss preliminary results of the wind-driven currents deduced from Pacific drifter data sets, including the data set used here. Reverdin et al. (1985), Niiler et al. (1989), and Richardson (1983) use drifters to describe mesoscale eddies. Niiler et al. (1997) describe the data set used in this study.

Hansen and Paul (1984) used data from 20 satellite-tracked drifting buoys deployed in the eastern equatorial Pacific in a study of the nature, effects, and energetics of currents associated with cusp-shaped long waves. They found that long waves are associated with a vigorous pattern of mesoscale eddies lying between the equator and 7°N, between 110°W and 105°W.

Poulain (1993) presents estimates of horizontal divergence and vertical velocity in the equatorial Pacific calculated from 12 years of surface drifter trajectories.

Mean divergence estimates are predominantly meridional and are similar to values from previous studies. Seasonal variability of equatorial divergence and upwelling are substantial and in phase with local wind forcing.

Poulain and Niiler (1989) present a description of the surface circulation off the Southern California and Baja coasts, based upon statistical kinematic analysis of the trajectories of satellite tracked drifters. Lagrangian and Eulerian statistics of the variations about a mean southward drift are computed, with drifter velocities averaged in 200 km by 200 km spatial bins. Absolute and relative particle dispersion was investigated using single and two-particle Lagrangian statistics.

A preliminary report by Ralph and Niiler (1995) presents findings of wind-driven currents described from this set of satellite-tracked drifters in the tropical Pacific. Wind-driven currents were inferred by subtracting the geostrophic component from the observed total current; the residual or Ekman currents can be used to test models of vertical mixing and heat flux. Five-day segments of drifter velocity measurements were binned into 1 latitude degree x 5 longitude degree boxes and averaged within each box. The drifter data were used to assess the validity of the Ekman and Pollard models by comparing the magnitudes of the observed and the predicted velocities.

Reverdin et al. (1994) use buoy drifts and current meter

records to present a statistical analysis of the seasonal variability of the equatorial Pacific Ocean at 15 meters. The objective of the analysis is to reduce the sampling noise by having a large data set, with the question of whether all drifters are comparable and whether the differences with the true currents can be corrected. The seasonal cycle is compared to ship-drift data, confirming that the analysis captured the seasonal cycle in the currents, and that the data is a faithful description of the mean tropical Pacific surface currents. The seasonal cycle is analyzed between 20°N and 20°S on a 1° latitude by 5° longitude grid, which captures a large zonal seasonal variability of the currents within 15 degrees of the equator.

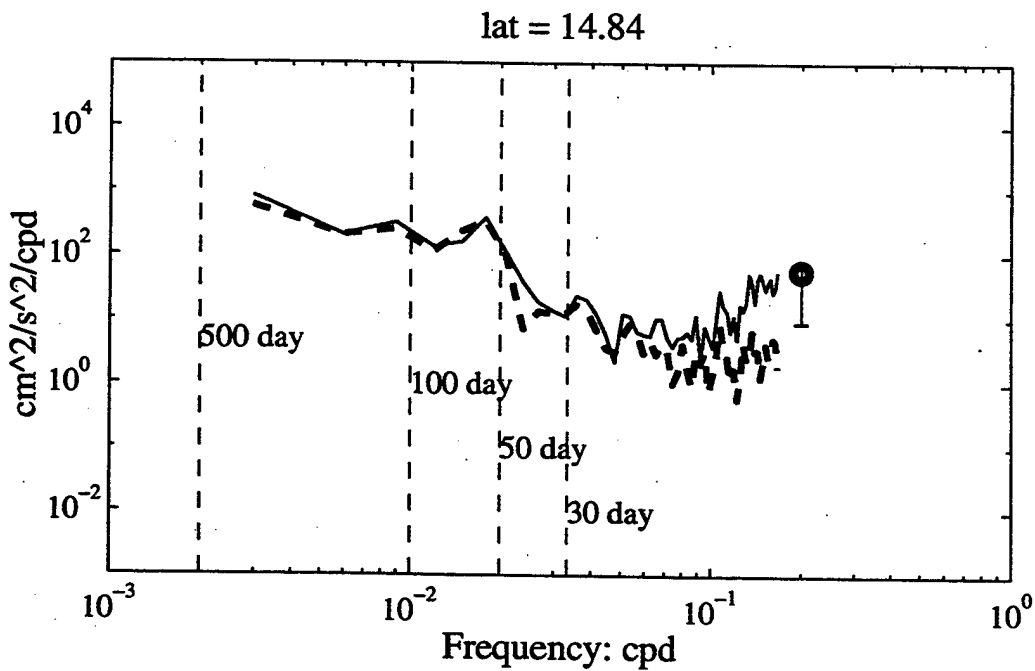
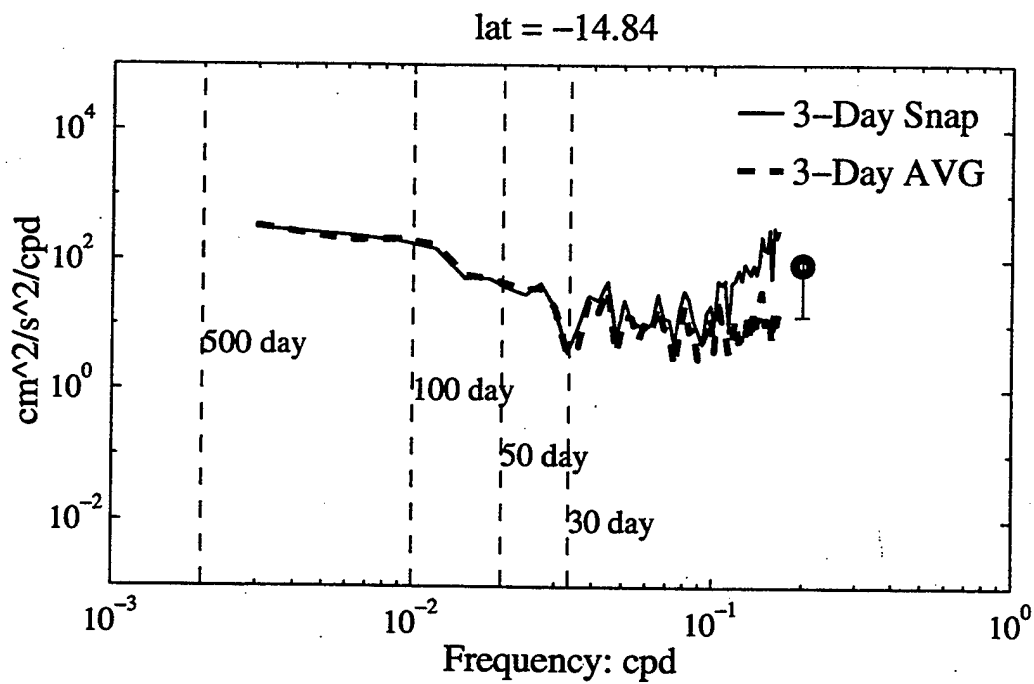


Figure 4. Power spectra (cpd) of the  $u$  velocity component at  $14.84^\circ\text{N}$  and  $14.84^\circ\text{S}$ , along  $160^\circ\text{W}$  in the tropical Pacific, before application of the 9-day running filter. (R. Tokmakian, personal communication)

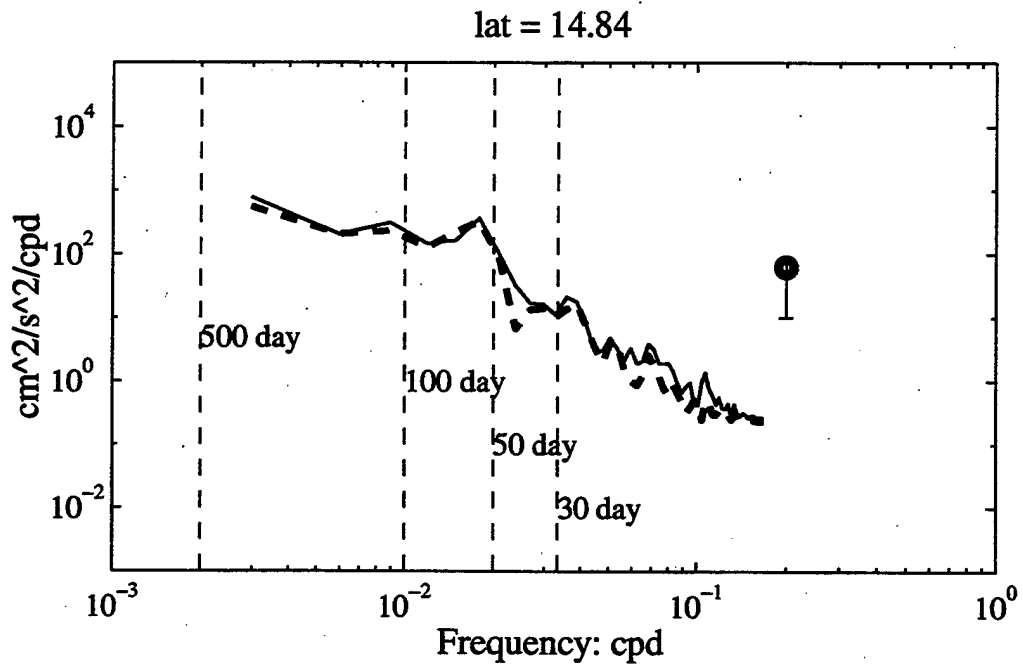
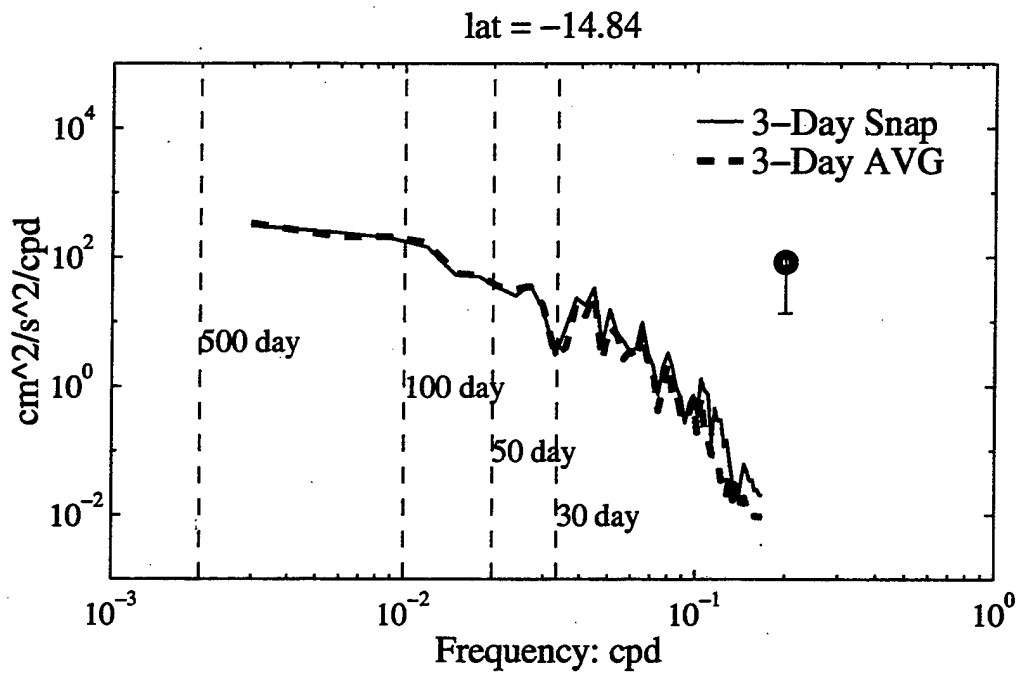


Figure 5. Power spectra (cpd) of the  $u$  velocity component at  $14.84^\circ\text{N}$  and  $14.84^\circ\text{S}$ , along  $160^\circ\text{W}$  in the tropical Pacific, after application of the 9-day running filter. (R. Tokmakian, personal communication)

## Zonal Velocity at 150W, Run 11

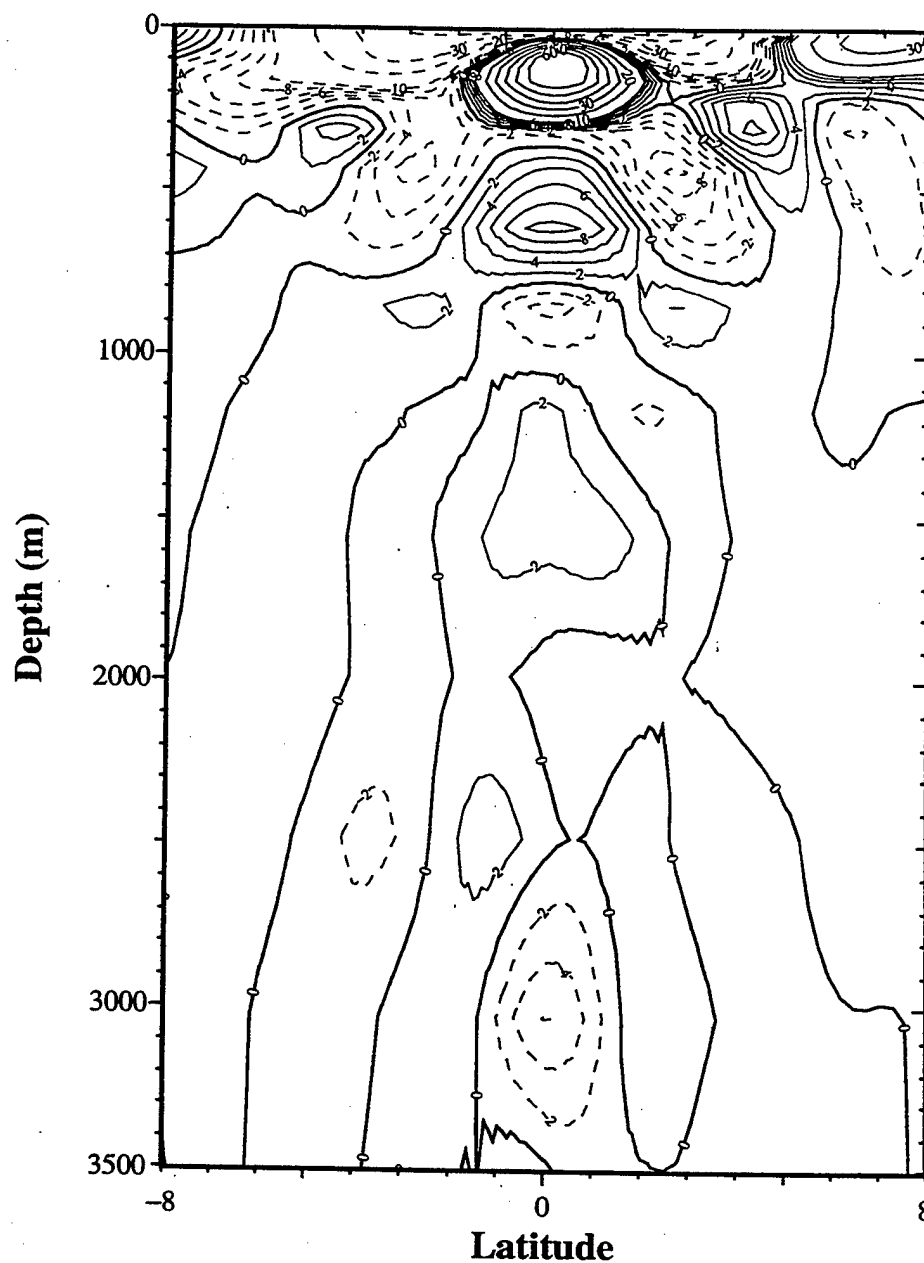


Figure 6. Cross-section of the zonal velocity at 150°W from POP11. The contour interval is 2 cm sec<sup>-1</sup> for  $u$  less than or equal to 10 cm sec<sup>-1</sup>, and 10 cm sec<sup>-1</sup> for  $u$  greater than 10 cm sec<sup>-1</sup>. Dashed contours denote westward flow. Figure 10 from Maltrud et al., 1997.

# PACIFIC OCEAN DATA through 31 May, 1996

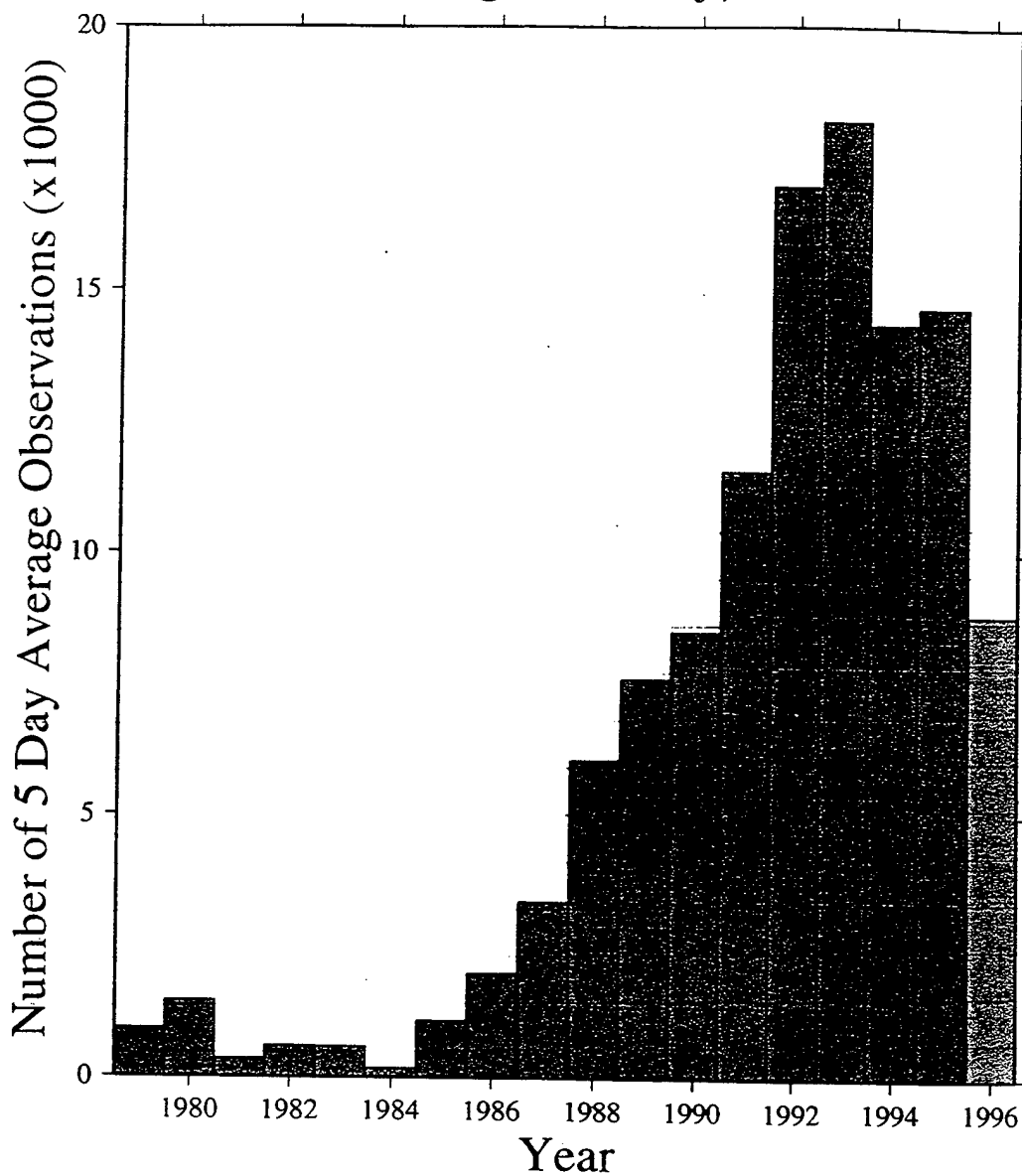


Figure 7. Frequency distribution of the number of five-day drifting buoy velocity observations as a function of year. (P. Niiler, personal communication).

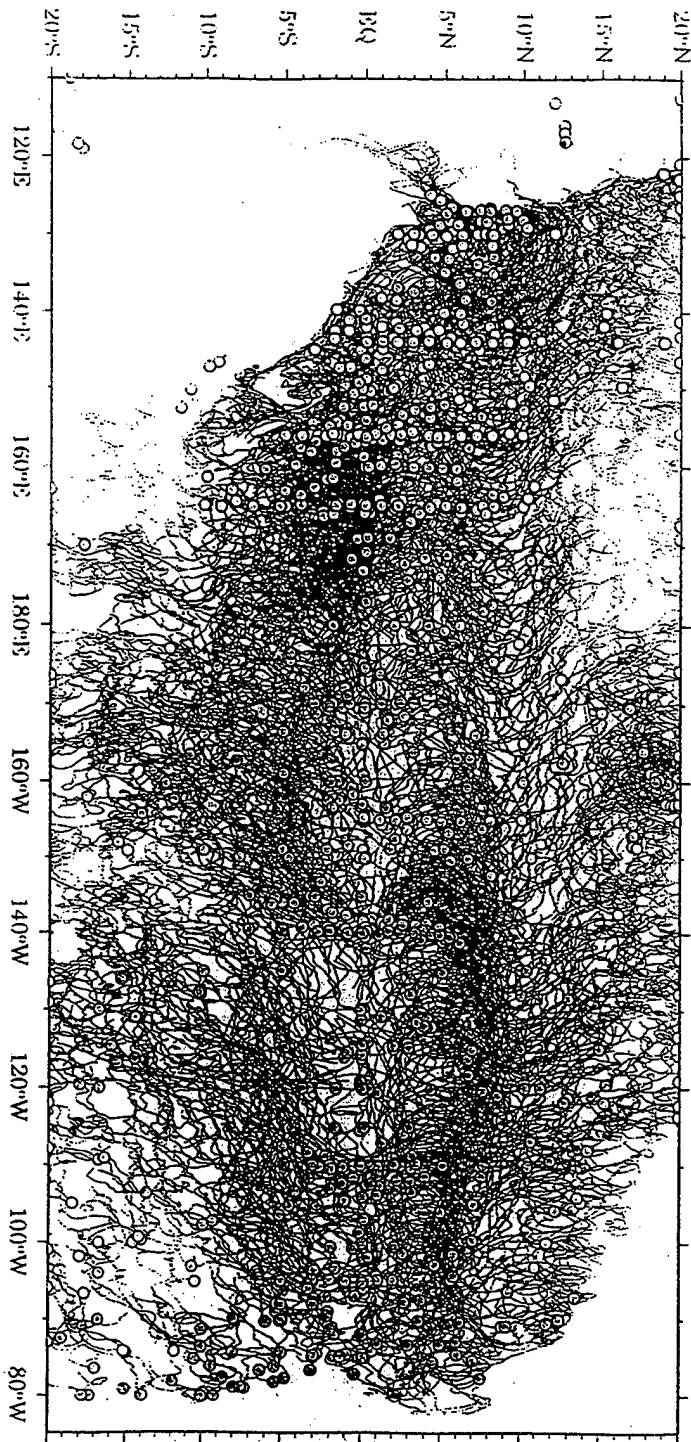


Figure 8. Tracks of drogued drifters released in the tropical Pacific from January 1, 1988 to December 31, 1994. From Niiler et al. (1997).

## IV. EULERIAN RESULTS

### A. MEAN FIELDS

#### 1. Mean Zonal Velocity

The mean zonal velocity ( $\text{cm s}^{-1}$ ) model and drifter fields (Figure 9) reveal the conspicuous surface circulation systems of the tropical Pacific, showing the low-latitude limbs of the recirculating subtropical gyres. Both data and output show the westward directed North Equatorial Current (NEC), between  $20^{\circ}\text{N}$  and  $8^{\circ}\text{N}$ , the South Equatorial Current (SEC), between  $3^{\circ}\text{N}$  and  $10^{\circ}\text{S}$ , and between them, the eastward flowing North Equatorial Countercurrent (NECC).

A weak eastward equatorial flow with values of  $10 \text{ cm s}^{-1}$ , west of the International Dateline and centered along the equator, is also common to both fields. Other similarities include a SEC maximum at  $2^{\circ}\text{N}$ ,  $125^{\circ}\text{W}$  of about  $50 \text{ cm s}^{-1}$ ; NEC current values ranging from about  $-20 \text{ cm s}^{-1}$  at approximately  $12^{\circ}\text{N}$  and  $140^{\circ}\text{E}$ , to  $-10 \text{ cm s}^{-1}$  in the eastern Pacific; and NECC maxima in excess of  $30 \text{ cm s}^{-1}$  in the western basin ( $5^{\circ}\text{N}$ ,  $130^{\circ}\text{E}$ ), and in the eastern basin ( $5^{\circ}\text{N}$ ,  $100^{\circ}\text{W}$ ), with consistent values of at least  $10 \text{ cm s}^{-1}$  across the basin.

In addressing features expected from historical observations, Lukas (1987) also reports a SEC maximum of 50

cm s<sup>-1</sup> at 2°N, and a minimum on the equator, along meridional transects at 158°W, 153°W, and 150°W. Drifter data would indicate a weak eastward flow along the equator at 135°W, previously observed by Hansen and Paul (1984) in investigations between 8°N and 8°S, 105°W to 110°W, and cited as imposing a jetlike structure in the westward flowing SEC. No indication of this weak eastward flow is indicated in the model field. As mentioned previously, the eastward flow in the western equatorial Pacific is indicative of westerly wind bursts.

The most notable difference in the model field is the elongation of the SECC to the eastern basin, from 150°E to 110°W. The latitudinal extent of the NEC in the model is slightly greater than that of the drifter data, extending from 5°N to slightly above 10°N, while the drifter data extends from 5°N to just below 10°N. (Reverdin et al., 1994).

This discrepancy between model and drifter results may be due to the representation of the winds forcing the model in the tropical South Pacific; if there is a paucity of wind observations in this area, it is likely that the forcing could be somewhat erroneous.

## **2. Mean Meridional Velocity**

The most significant feature of both mean meridional velocity fields (cm s<sup>-1</sup>) is the cross-equatorial symmetry of

generally northward flow north of the equator and southward flow south of the equator (Figure 10). Maximum northward and southward flow for the drifter field is at approximately  $110^{\circ}\text{W}$ , at  $8 \text{ cm s}^{-1}$  north of the equator and  $-10 \text{ cm s}^{-1}$  south of the equator. Model field maxima are displaced west to about  $140^{\circ}\text{W}$ , which may again be due to inadequacies in the wind forcing.

Similar observations from drifter data were made by Luther and Johnson (1990), and Hansen and Paul (1984); both studies report that, with the exception of brief crossings in conjunction with eddies, drifters avoided crossing the equator. Hansen and Paul (1984) infer from the divergence of the meridional flow with the equator that the dominant process is Ekman transport, divergent at the equator and driven by the southeast trade winds. The feature at  $5^{\circ}\text{N}$ ,  $124^{\circ}\text{E}$  (positive / negative reversal) in both model output and drifter data indicate a standing Rossby wave, where the mean flow has arrested the westward propagating Rossby wave and rendered it stationary (Lukas, 1987; Philander, 1990; Pedlosky, 1996). In a study of the meridional structure of near-equatorial currents, Poulain (1993) concluded that the zonally averaged divergence is concentrated in a narrow 20-km band centered on the equator, and that mean divergence estimates are predominantly meridional.

Significant differences exist in magnitudes, with the model output showing ranges in the central basin in excess of

18 cm s<sup>-1</sup> at 4°N 140°W and -16 cm s<sup>-1</sup> at 3°S 130°W, while the drifter data values are displaced to the east, with values in excess of 8 cm s<sup>-1</sup> at 3°N 115°W and -10 cm s<sup>-1</sup> at 3°S 115°W.

These differences in magnitudes may be due to a lack of a model mixed layer. Since the model is solely dependent on the Richardson-number formulation of Pacanowski and Philander (1981) for the vertical redistribution of properties, the Ekman drift is largely trapped in the upper layer, producing artificially strong flow.

### **3. Mean Velocity Vectors**

The velocity vector fields (cm s<sup>-1</sup>) again show the alternating eastward and westward zonal flows of the tropical Pacific (Figure 11), with the latitudinal shear between oppositely directed currents. The southern branch of the SEC (centered at about 5°S) extends across the basin to New Guinea while the southern branch ends near the IDL. The East Australia Current is seen south of 15°S, along the 155°E meridian.

In plots of surface current vectors of the tropical Pacific Philander et al. (1986) and Reverdin et al. (1994) also show the latitudinal shear north of the equator and strong westerly flow in the eastern Pacific. Reverdin et al. (1994) also show the bifurcation of the SEC in the western Pacific.

The most obvious difference between output and data occurred in the vicinity of the Indonesian Throughflow (ITF), with the highest drifter values indicating a strong cyclonic circulation in the Banda Sea that was not indicated in the model output; however, with the large grid size and few drifters in this region, no definite conclusions can be drawn.

#### **4. Mean SST**

Mean temperature fields ( $^{\circ}\text{C}$ ) from model and drifter data exhibit the characteristic warm pool (designated by the  $29^{\circ}\text{C}$  isotherm in the drifter data) extending from the western equatorial Pacific southeast to about  $160^{\circ}\text{W}$ ,  $10^{\circ}\text{S}$ , and the cold tongue extending along the equator from the South American coast to the mid-basin (Figure 12). Except for a band of warm surface water that extends across the ocean basin just north of the equator, SST from both fields are much lower in the eastern than the western tropical Pacific. Hansen and Paul (1984) report similar SST patterns in the eastern equatorial Pacific and find evidence of cold intrusions that associate this cold tongue with equatorial divergence of Ekman transport and/or advection from the Peruvian coastal upwelling region to as far as  $160^{\circ}\text{W}$ .

The drifter temperature field shows the western warm pool as larger and extending farther west than depicted by Levitus (1982). Since the model is restored to Levitus,

conversely the western warm pool is not as extensive in the model output as it is in the drifter data.

## **B. VARIABILITY**

The variability of the velocity components and temperature were calculated from the deviations of the bin-averaged ensemble means discussed in the previous section.

### **1. Variability of Zonal Velocity**

Both fields show coherent patterns across the Pacific interior, with weaker variability poleward of  $10^{\circ}\text{N}$  and  $10^{\circ}\text{S}$  than in the equatorial region (Figure 13). Drifter and model both show two general regions of relative maxima along the equator and at  $7^{\circ}\text{N}$ , and two general regions of relative minima, at  $14^{\circ}\text{N}$  and south of  $10^{\circ}\text{S}$ , east of  $140^{\circ}\text{W}$ . Model maxima are about  $15\text{ cm s}^{-1}$  at  $7^{\circ}\text{N}$  and  $25\text{ cm s}^{-1}$  at the equator, while drifter maxima for these regions are 25 and  $50\text{ cm s}^{-1}$ , respectively. Both fields have similar locations of maxima in the the western Pacific, at about  $130^{\circ}\text{E}$  and  $4^{\circ}\text{N}$ , with values of about  $40\text{ cm s}^{-1}$  for drifter data and  $30\text{ cm s}^{-1}$  for the model values.

Niiler et al. (1997) state that the maximum in the eastern basin on the equator, between  $100^{\circ}\text{W}$  and  $140^{\circ}\text{W}$ , results from variations produced by equatorial wave propagation from the west, and from the local generation of

instability waves in the east. A second relative maximum is at about 7°N in the eastern basin, where organized wave/eddy motions have been reported in Geosat sea surface height data (Perigaud, 1990), or possibly due to seasonal variability of the NEC. Poulain (1993) also mentions that the variability not associated with the wind could be induced by inertia-gravity waves excited by shear instability of the zonal currents. Reverdin et al. (1994) report high frequency (20 to 30 days) values on the equator ranging from 14 cm s<sup>-1</sup> at 170°W to 26 cm s<sup>-1</sup> at 110°W.

Model values are less than drifter data in all regions; along the equator the model western basin maximum displays about 80% of the drifter variability and is displaced to the west (possibly as a result of the wind forcing). The magnitude of the eastern basin model maximum is about 55% of the observed value, while the model maximum at 7°N is about 60% of the corresponding observed value. Away from these maxima, the model values are roughly half the drifter values.

## **2. Variability of Meridional Velocity**

Variability in  $v$  (cm s<sup>-1</sup>) for both fields is largest just north of the equator in the western and east-central Pacific, and north of the equator in the eastern Pacific (Figure 14). In the western Pacific, drifter and model maxima are centered 3°N, 130°E, with drifter values of >35 cm s<sup>-1</sup>, and model

values of  $>14 \text{ cm s}^{-1}$ . Maxima exist in both fields on the equator near  $4^{\circ}\text{N}$ ,  $128^{\circ}\text{W}$ , with drifter values of  $>30 \text{ cm s}^{-1}$ , and model values of  $>10 \text{ cm s}^{-1}$ .

Reverdin et al. (1994), in using data from five current meter moorings from 1987 - 1992, report high frequency (20 to 30 days) meridional variance values along the equator ranging between  $15 \text{ cm s}^{-1}$  at  $170^{\circ}\text{W}$  to  $28 \text{ cm s}^{-1}$  at  $110^{\circ}\text{W}$ . These values in the eastern Pacific are again caused by instability waves (Hansen and Paul, 1984; Reverdin et al., 1994). Poulain (1993) associates the maxima in the eastern Pacific with semiannual fluctuations of the equatorial divergence.

The most significant difference exists in the magnitudes, with model output less than drifter values. This may be due to inadequate representation of wind forcing in the model, lack of a mixed layer, and possibly still too coarse resolution.

### **3. Variability of Total (u and v) Velocity**

Both model- and drifter-based representations of eddy kinetic energy show good agreement (Figure 15) in the central basin straddling the equator, away from land, with drifter values ( $\text{cm s}^{-1}$ ) slightly higher than model output; output and data do not agree as well at higher latitudes. Drifter data show greater variability in the vicinity of the HE and ME, in the south Pacific, east of Australia, and in the WBC region

north of New Guinea. Drifter variability is also greater in the region between 10°S and 20°S.

#### **4. Variability of SST**

Drifter data (Figure 16) show a temperature variance maxima (°C) along the equator, in the eastern Pacific extending from the South American coast to about 130°W, approximately at the IDL; a weaker maxima is seen in the model. Hansen and Paul (1984) also refer to a region of larger variance at 2°S, not indicated in the drifter or model data set, and attribute it to the passage of a cold pool, perhaps due to upwelling. Drifter variability is greater than model output due to model restoration to Levitus climatology, on a 30-day time scale. Also, applying a 9-day running mean to temperature, for consistency with the velocity data, further reduced the temperature variability.

### **C. DIVERGENCE AND RELATIVE VORTICITY**

#### **1. Divergence**

Divergence ( $10^{-7} \text{ s}^{-1}$ ) was calculated using

$$\nabla \cdot \mathbf{V}_H = (\partial \langle u \rangle / \partial x + \partial \langle v \rangle / \partial y)$$

in a centered-difference scheme applied to the 2° x 8° Eulerian means discussed above.

Divergence in the drifter and model (Figure 17) was well

defined and due mainly to  $\partial\langle v \rangle / \partial y$ . Both fields are similar in outline, with strongly divergent circulation along the equator east of the IDL and weakly divergent flow in the western basin. Both representations show equatorial divergence at all meridians, except at about 120°E. The highest value for the model output is  $7 \times 10^{-7} \text{ s}^{-1}$ , centered at about 140°W, while the drifter data has two regions of maxima,  $4 \times 10^{-7} \text{ s}^{-1}$ , centered at about 145°W, and  $3 \times 10^{-7} \text{ s}^{-1}$  centered at about 110°W. Both data and output indicate the southern limb of the convergent north Pacific subtropical gyre north of 12°N. The convergence, poleward of 3°N and 3°S in both model output and drifter data, was more broad scale than the divergent fields. The divergence is due principally to the surface poleward Ekman flow on each side of the equator, driven by the prevailing westward trade winds.

The most significant discrepancy is slightly higher model magnitudes, due to use of mean velocity values in the divergence calculation. The divergence calculation depends mainly on  $\partial\langle v \rangle / \partial y$ , which reflects the mean meridional velocity  $\langle v \rangle$ . Thus, the generally higher mean velocity values from the model output, compared to drifter data, also translates to higher divergence values.

## 2. Relative Vorticity

Relative vorticity ( $10^{-7} \text{ s}^{-1}$ ) was also calculated from the  $2^\circ \times 8^\circ$  Eulerian averages using

$$\zeta = (\partial \langle v \rangle / \partial x - \partial \langle u \rangle / \partial y),$$

and is due principally to  $\partial \langle u \rangle / \partial y$ , reflecting variations of the zonal currents. The relative vorticity of both model- and drifter-based fields (Figure 18) is similarly defined in spatial extent, with a narrow band of positive vorticity along the equator with negative vorticity north and south, alternating approximately every five degrees. Relative vorticity values are similar along the equator, with the model about 30% higher than observed data in the regions of  $10^\circ\text{S}$  and  $10^\circ\text{N}$ .

## D. COVARIANCE FIELDS

### 1. Covariance of u and v: $\langle u'v' \rangle$

Given N pairs of observations the covariance between two variables is calculated from (Chatfield, 1996):

$$s_{xy} = \sum_{i=1}^N (x_i - \bar{x})(y_i - \bar{y}) / (N - 1).$$

Both drifter data and model output (Figure 19) show consistent negative values north of the equator. The drifter data show maxima along the equator, between the dateline and

100°W, associated with the velocity variance peaks. The high negative values in the western tropical Pacific of the drifter data occur farther to the west and north of the equator in the model; however, the drifter data is noisy. The covariance maximum along the equator in the drifter data, between the IDL and 100°W, is not indicated in the model output.

Hansen and Paul (1984) indicate that the negative covariance north of the equator supports the hypothesis that waves derive energy from the barotropic instability of the meridional shear of the zonal mean flow. Luther and Johnson (1990) attribute the broad maximum along the equator to a momentum flux that is down gradient of the mean zonal velocity, with magnitudes comparable to a WBC.

## **2. Covariance of Velocity and SST**

The covariance of zonal velocity and SST ( $\text{cm s}^{-1} \text{ } ^\circ\text{C}$ ) in drifter and model (Figure 20) vector plots both show a tendency of the covariance vectors to tilt towards the equator, implying a net eddy heat convergence in the equatorial band. Both exhibit rough similarity in the general distribution of the positive covariance along the equator, indicating eastward heat flux, with the model output amplitudes less than the drifter data. Both fields indicate convergence (downwelling) in cooler regions (along 5°N and

5°S), where poleward flow predominates, and divergence (upwelling) in warmer regions (along the equator) where poleward flow is weaker. The greatest variance in both fields is shown in the cold tongue along the east basin, extending westward into the high gradient region of the tongue. The prevalence of equatorial upwelling is shown as this narrow tongue of relatively cooler SST extending from the coast of South America to the IDL. The drifter data values are highest in the east, at approximately 100°W, whereas the model output is greatest at the IDL with smaller but consistent values to the east.

Hansen and Paul (1984) report a slight negative covariance in the southern hemisphere (as indicated in the drifter data, but not apparent in the model output), and more definite negative values north of the equator (indicated in the model but less apparent in the drifter data).

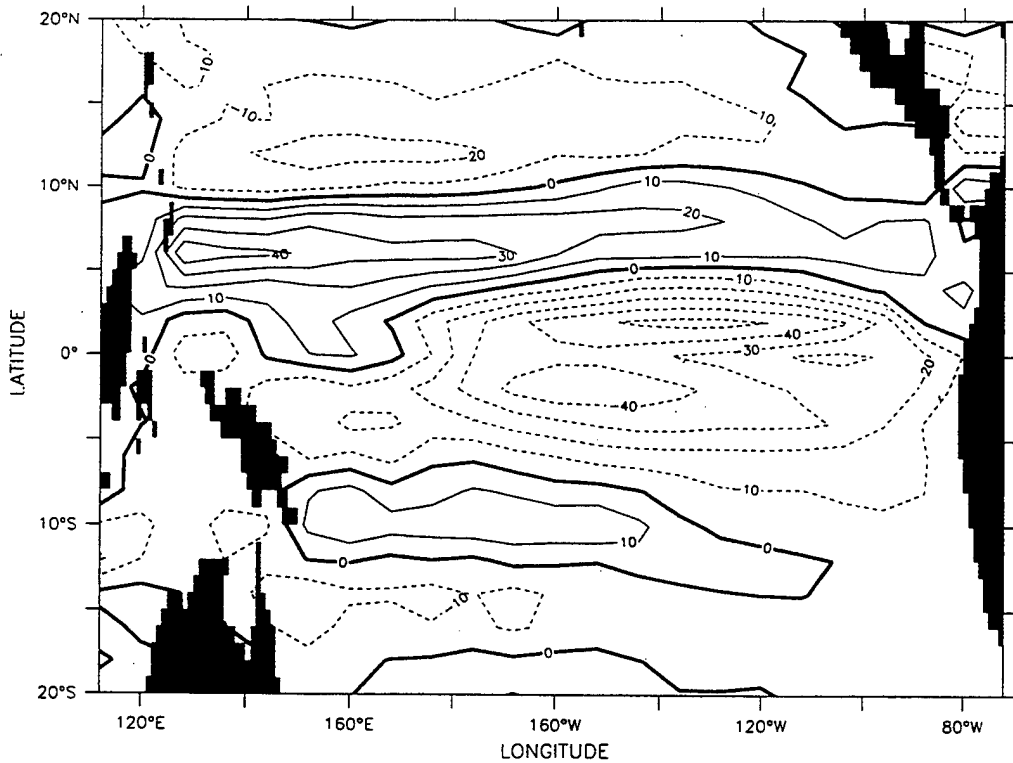
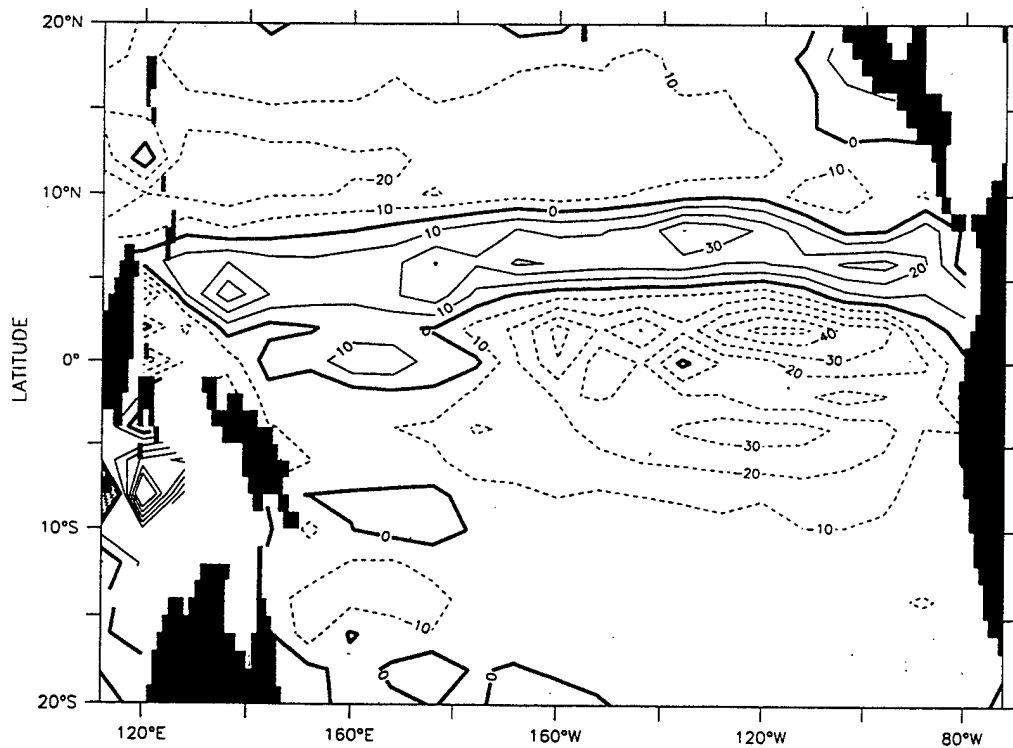


Figure 9. Mean Zonal Velocity ( $\text{cm s}^{-1}$ ): Drifter Data (top) and Model Output (bottom).

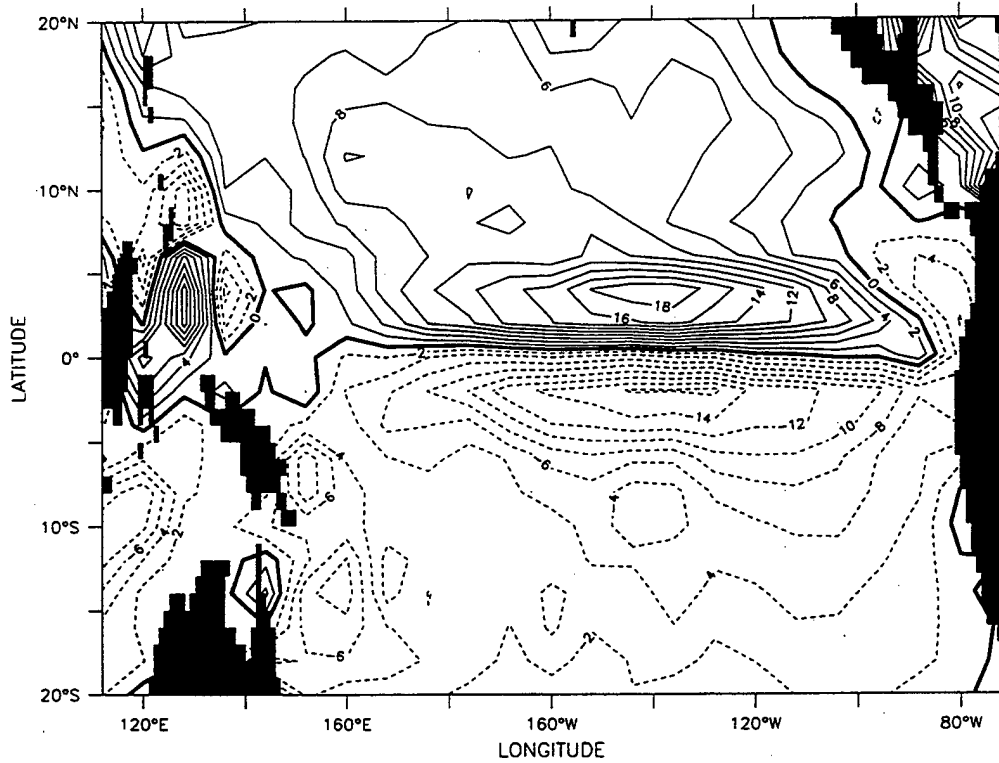
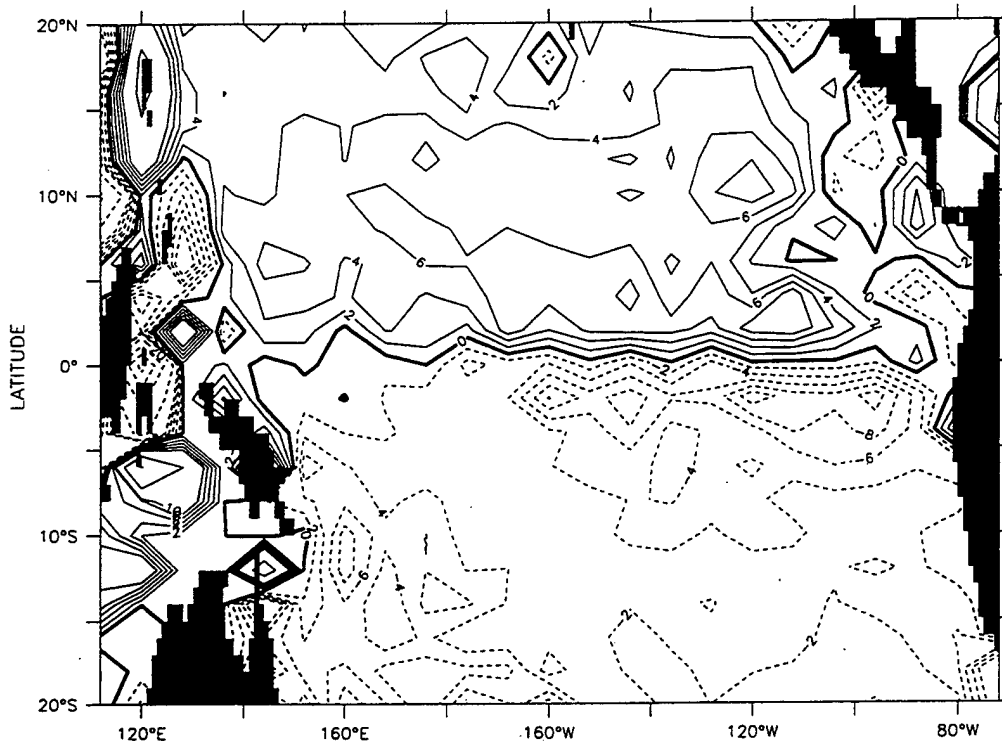
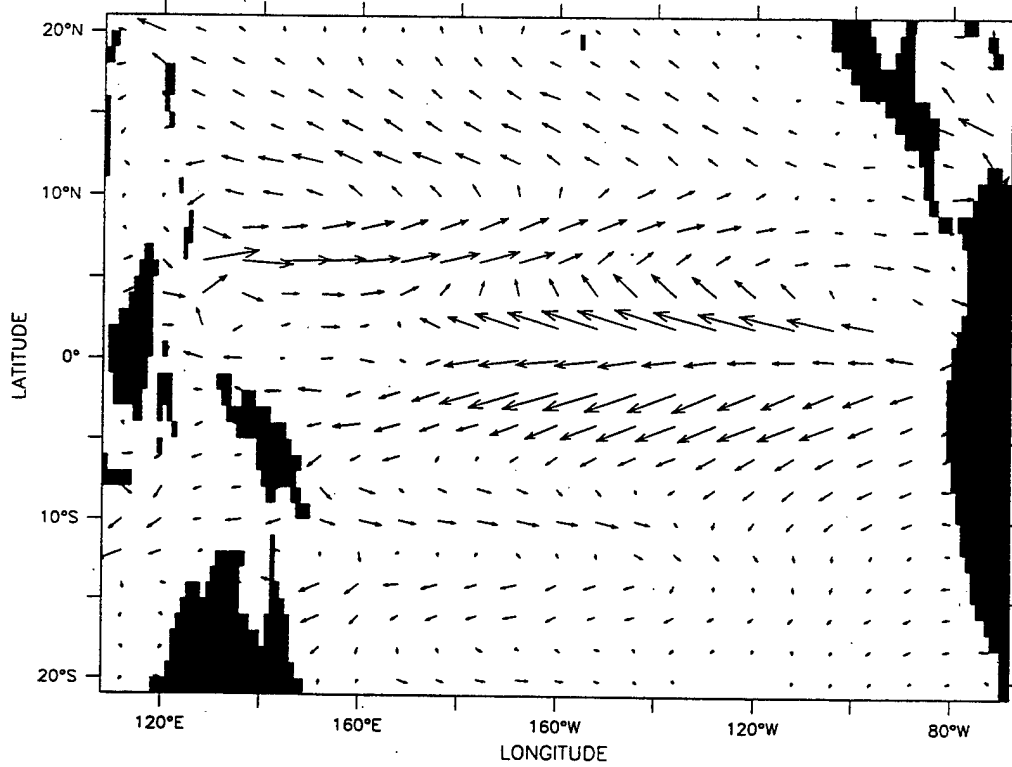
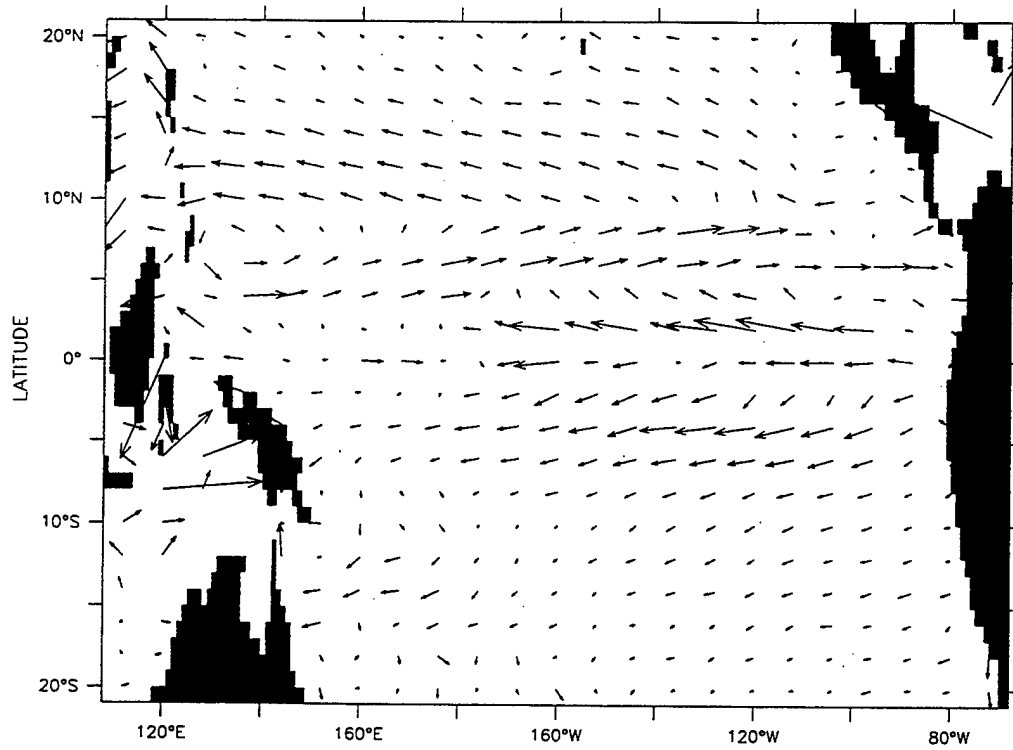


Figure 10. Mean Meridional Velocity ( $\text{cm s}^{-1}$ ): Drifter Data (top) and Model Output (bottom).



$\longrightarrow$  50.0  
 Figure 11. Mean ( $u$  and  $v$ ) Velocity Vectors ( $\text{cm s}^{-1}$ ): Drifter Data (top) and Model Output (bottom).

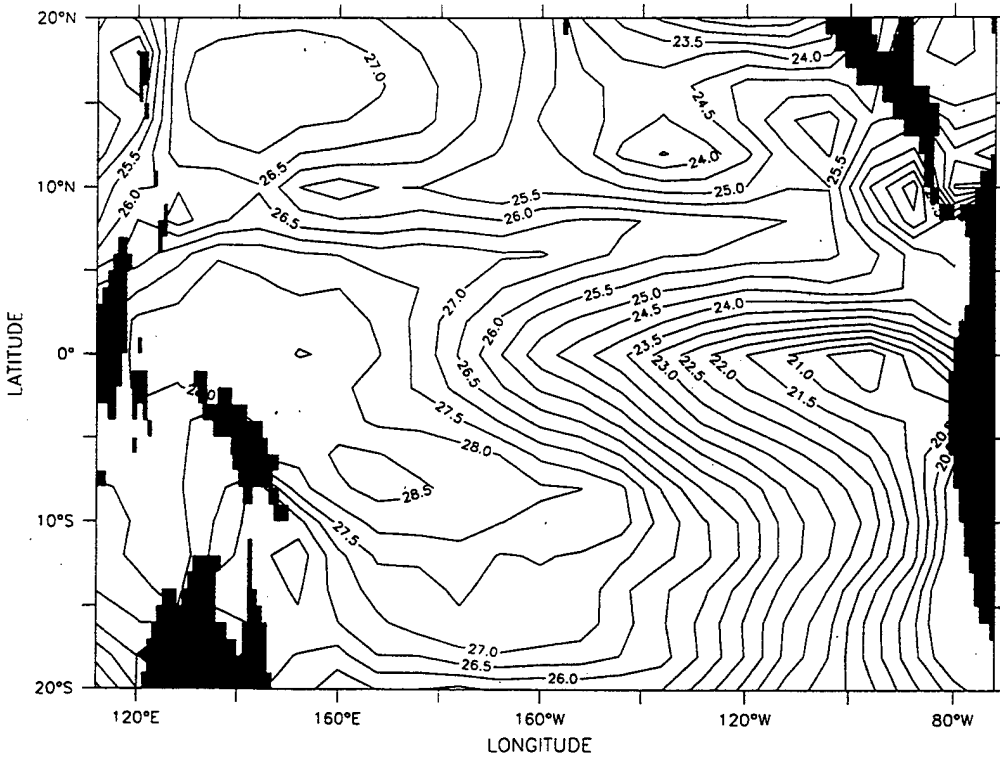
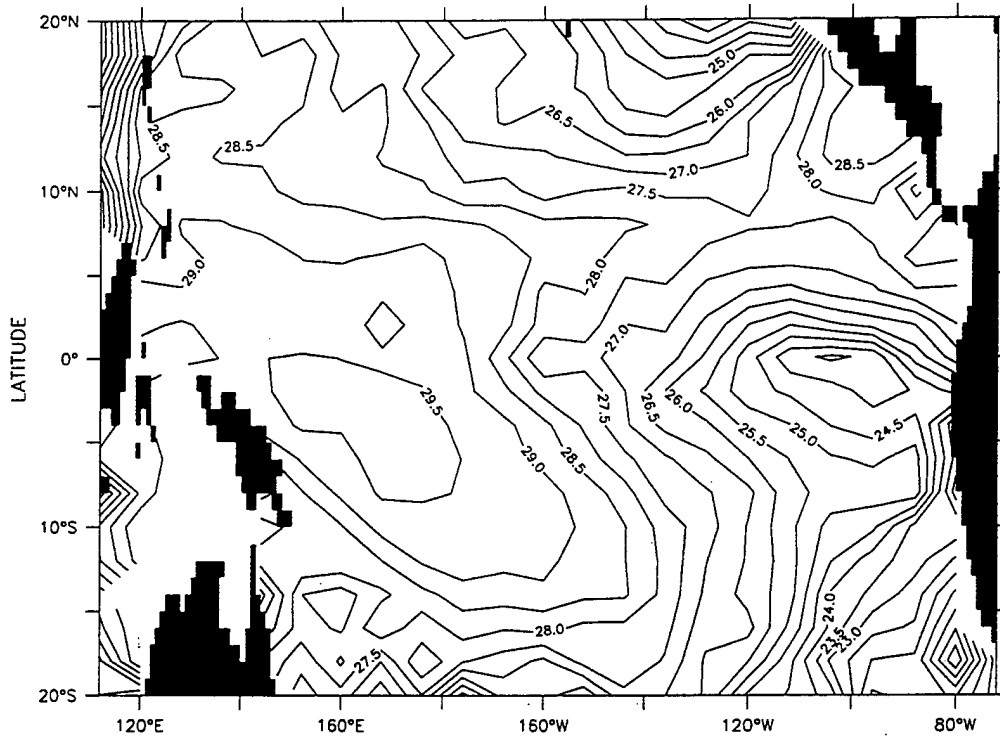


Figure 12. Mean Temperature ( $^{\circ}\text{C}$ ): Drifter Data (top) and Model Output (bottom).

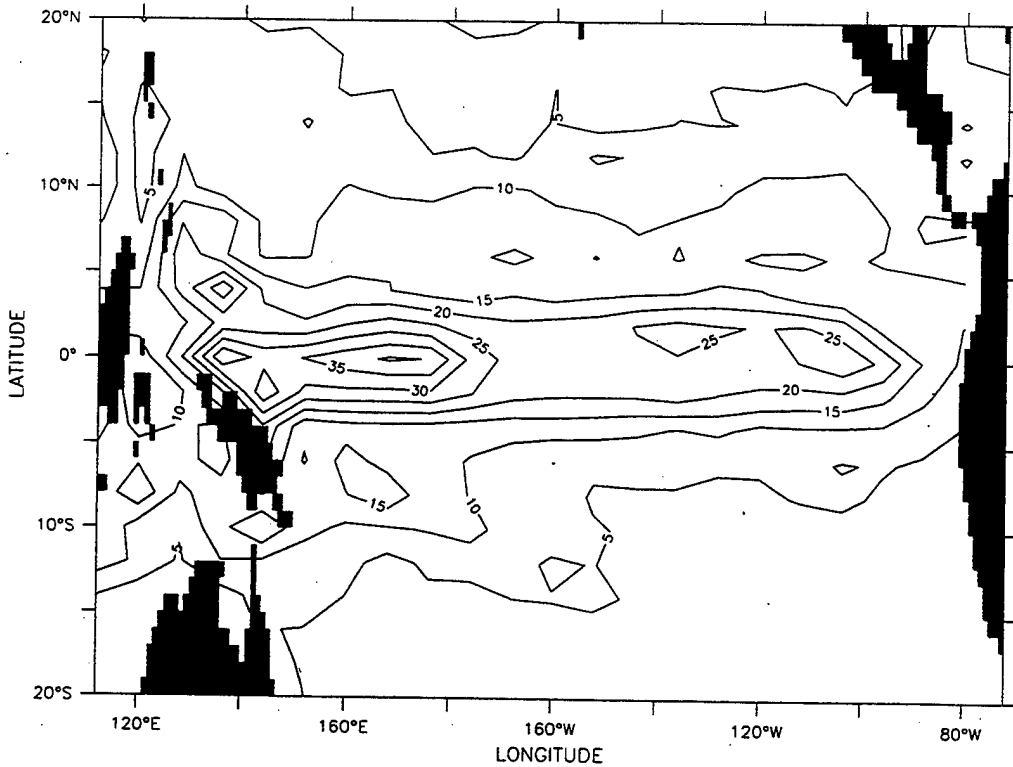
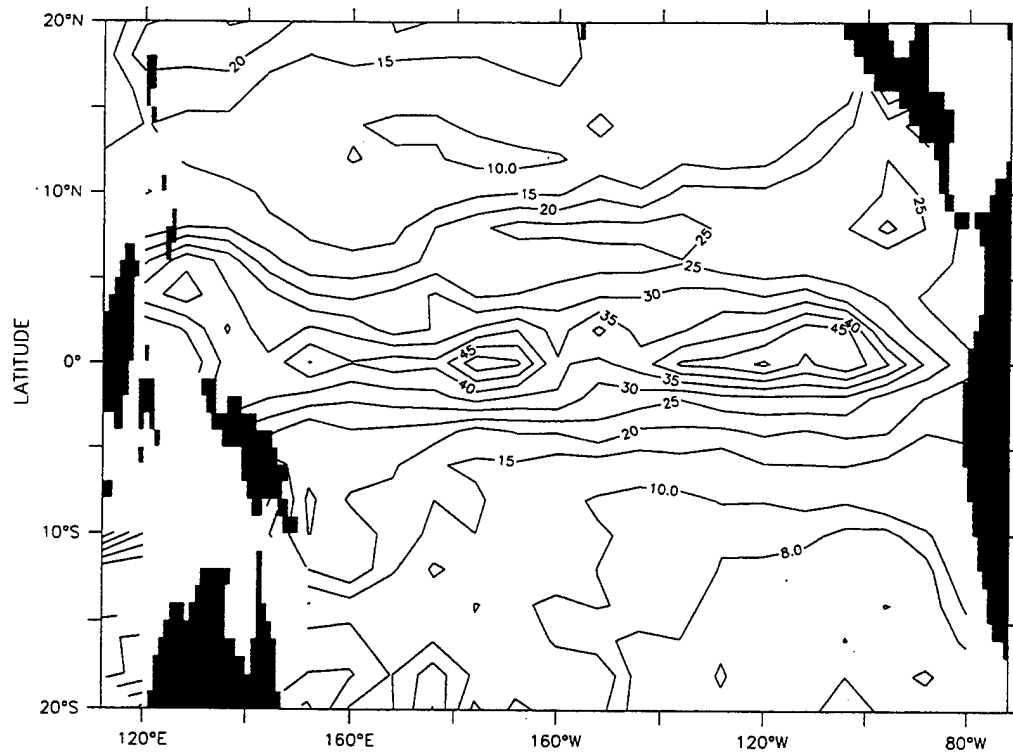


Figure 13. Variability (standard deviation) of Zonal Velocity (cm s<sup>-1</sup>): Drifter Data (top) and Model Output (bottom).

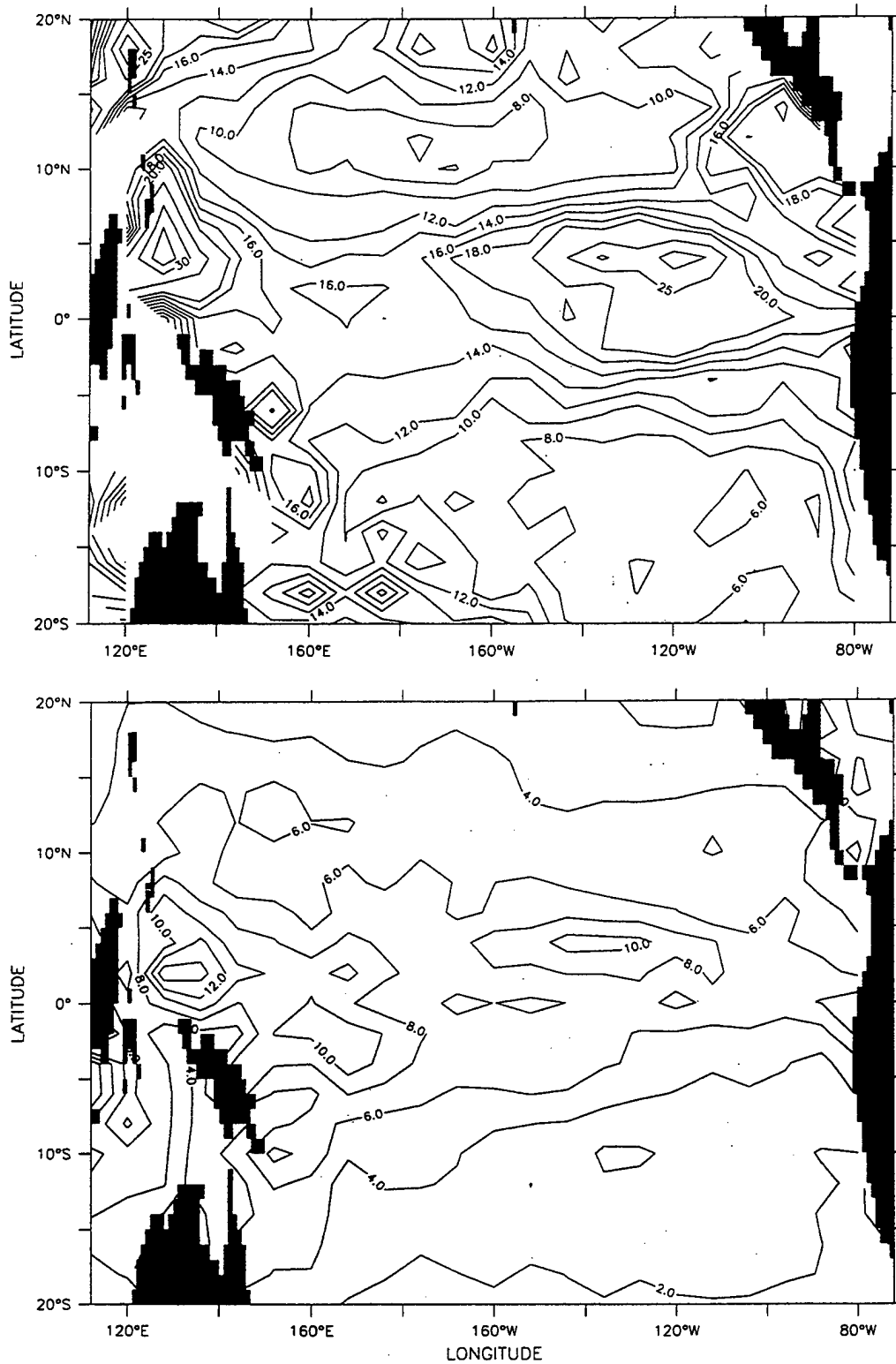


Figure 14. Variability (standard deviation) of Meridional Velocity ( $\text{cm s}^{-1}$ ): Drifter Data (top) and Model Output (bottom).

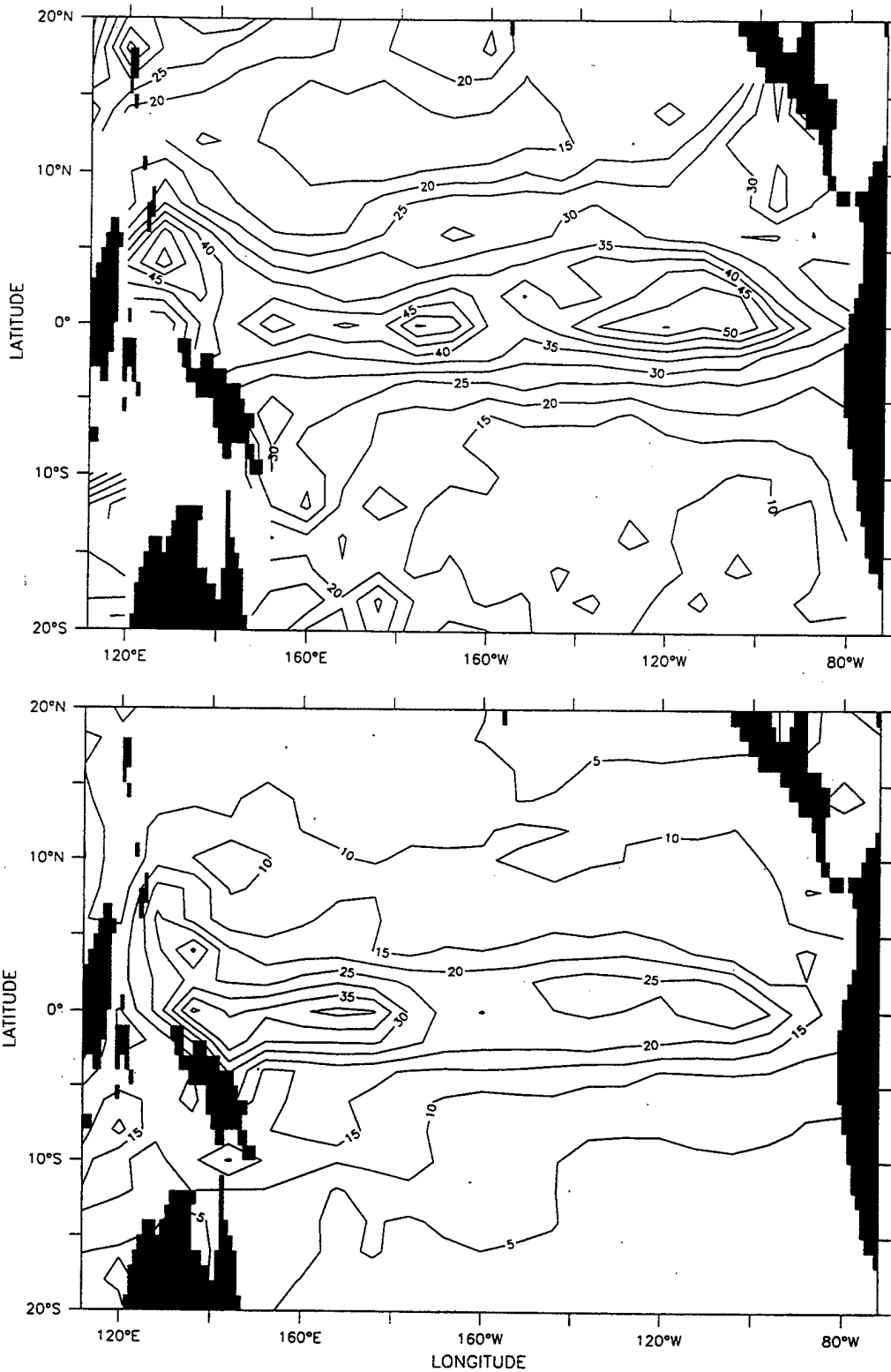


Figure 15. Variability (square root of eddy kinetic energy) of  $u$  and  $v$  Velocity ( $\text{cm s}^{-1}$ ): Drifter Data (top) and Model Output (bottom).

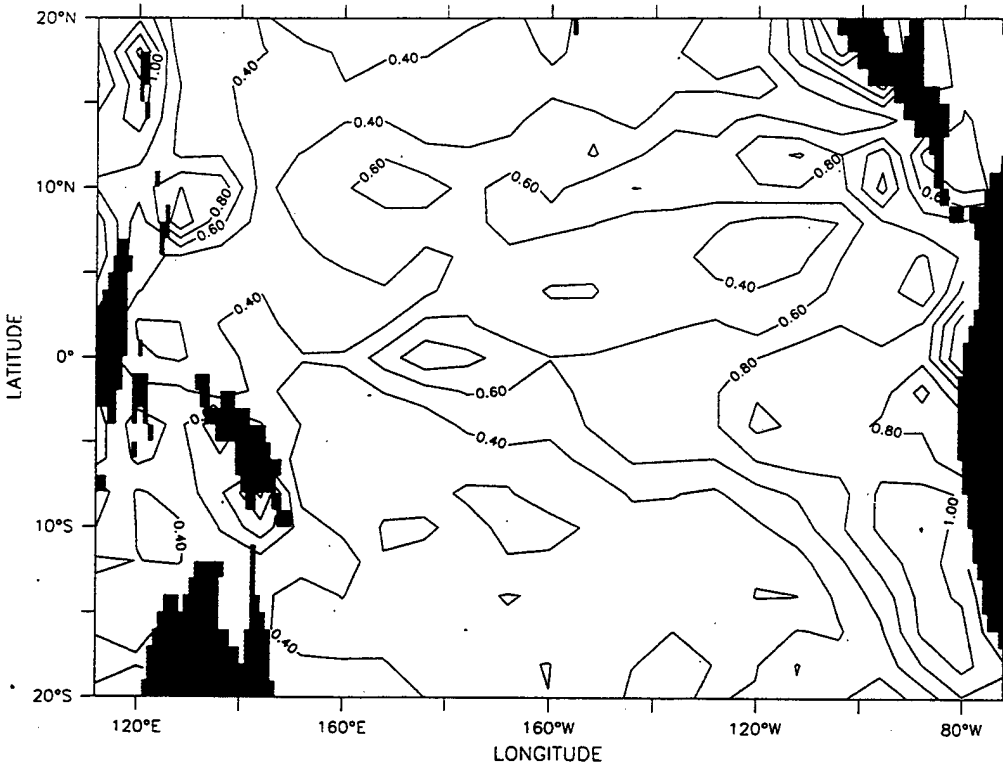
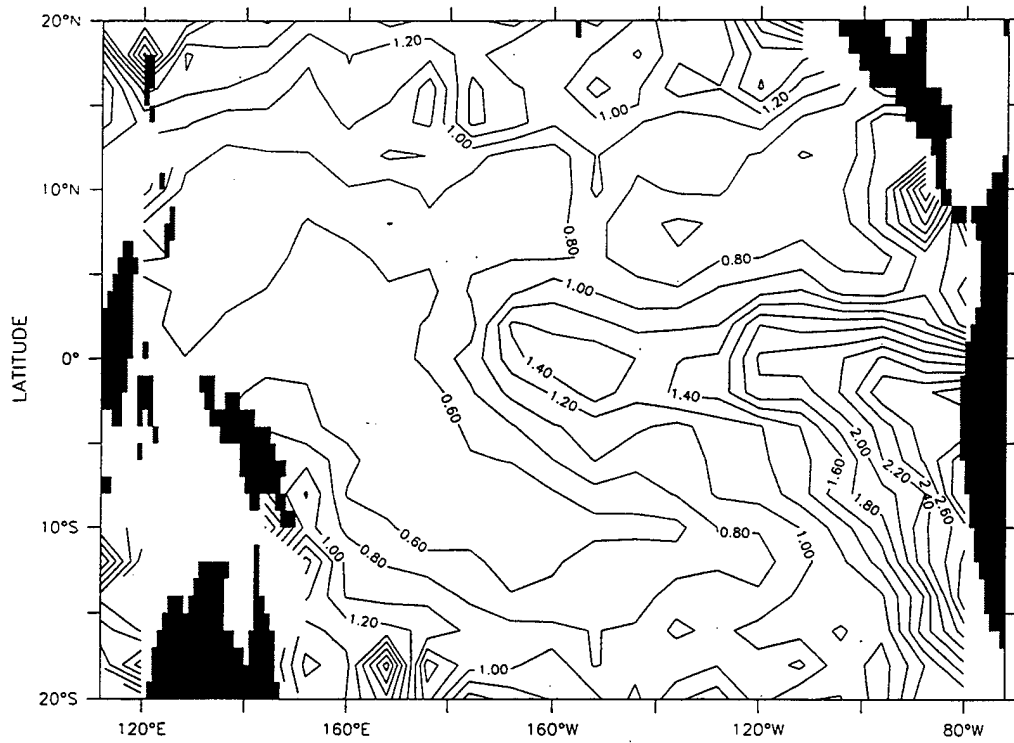


Figure 16. Variability of SST ( $^{\circ}\text{C}$ ): Drifter Data (top) and Model Output (bottom).

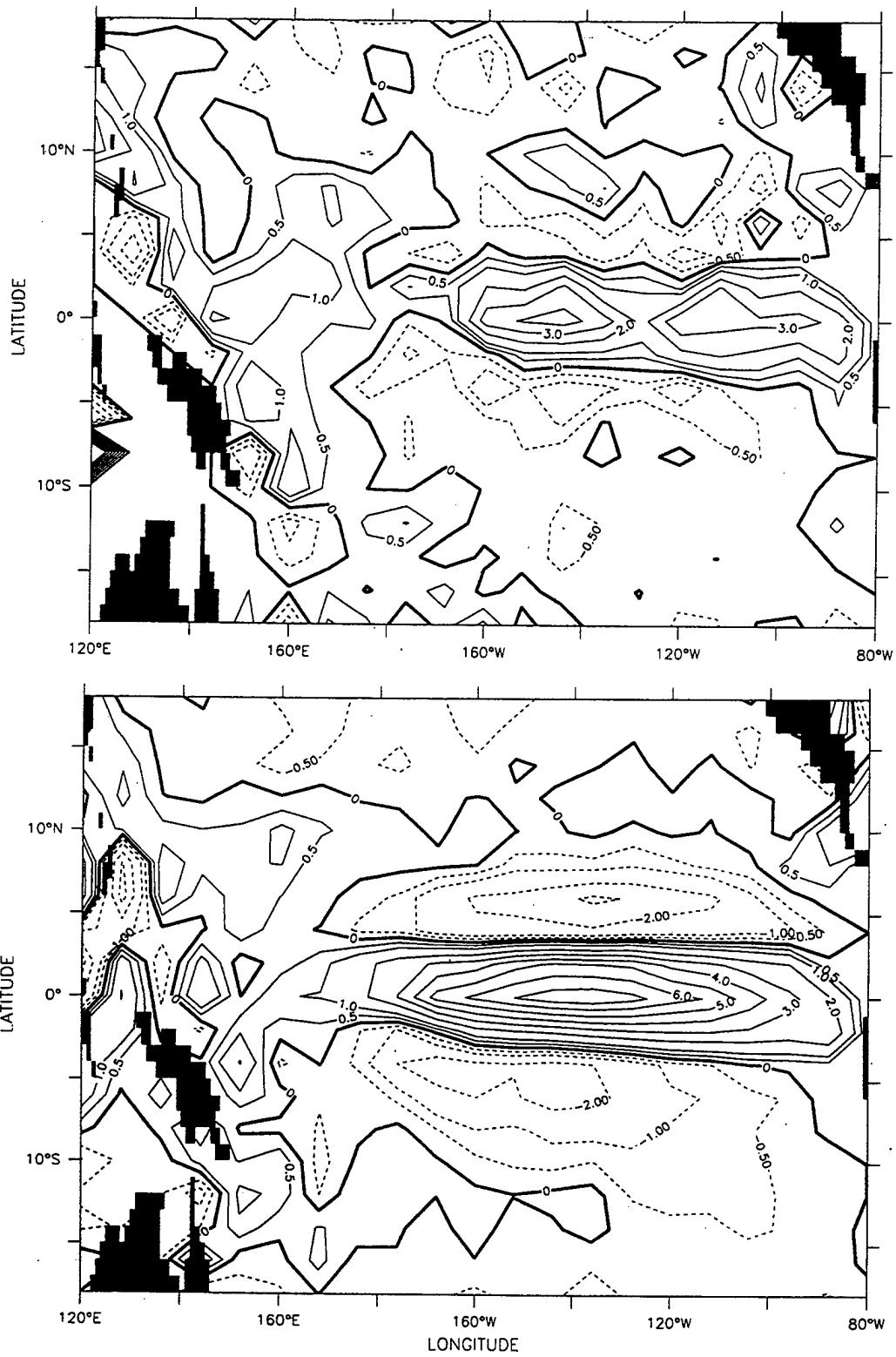


Figure 17. Divergence ( $10^{-7} \text{ s}^{-1}$ ): Drifter Data (top) and Model Output (bottom).

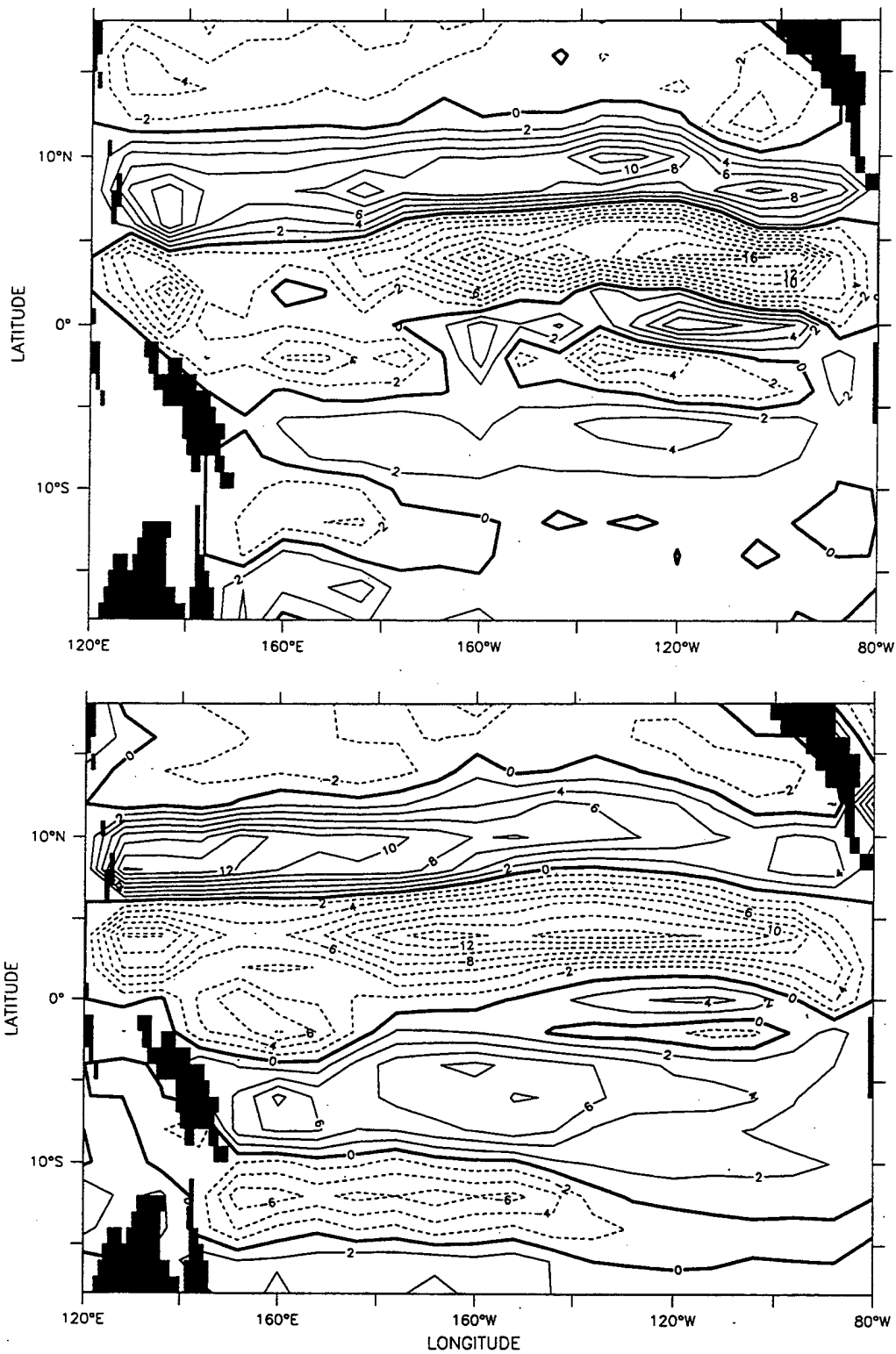


Figure 18. Relative Vorticity ( $10^{-7} \text{ s}^{-1}$ ): Drifter Data (top) and Model Output (bottom).

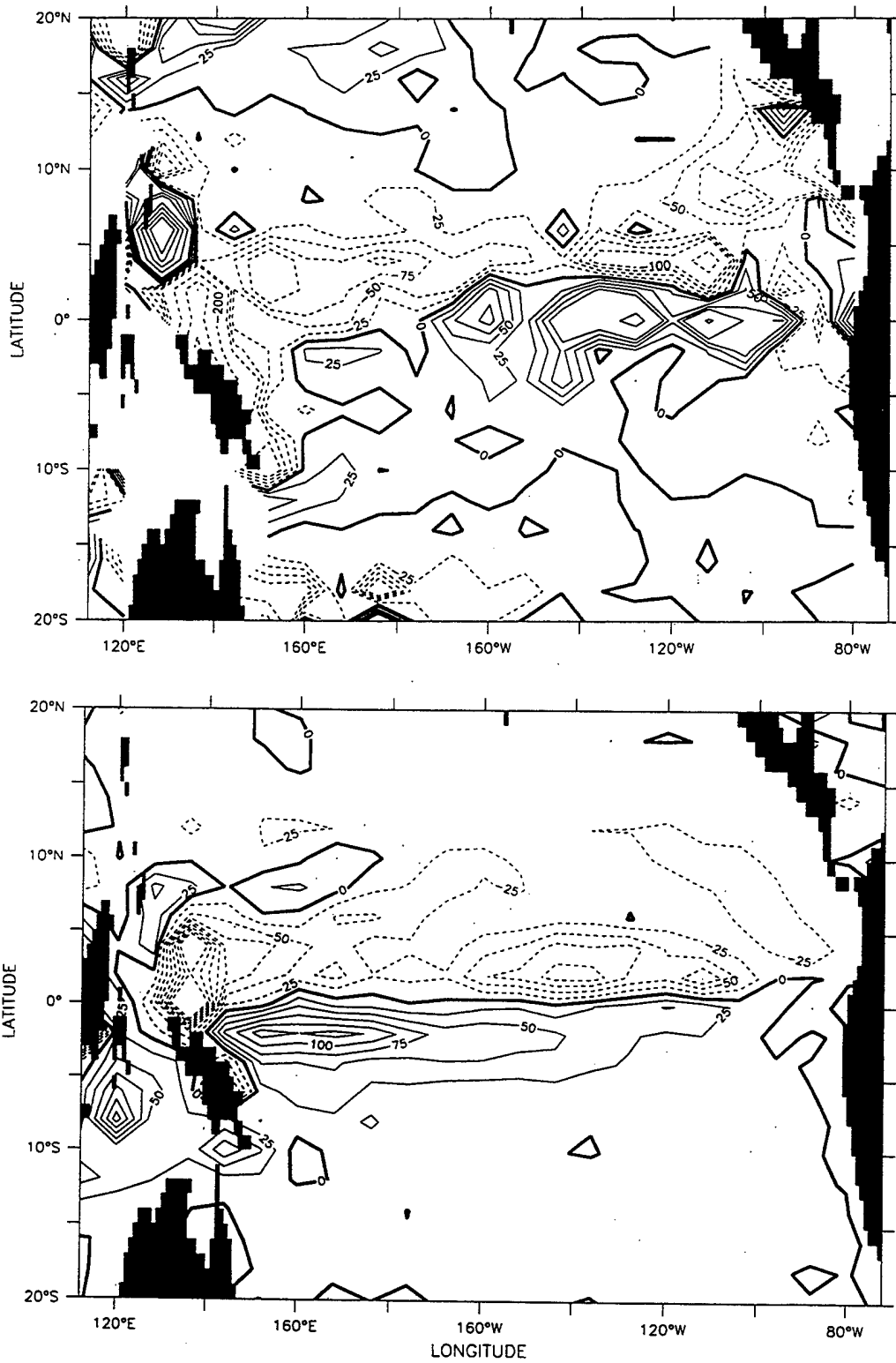
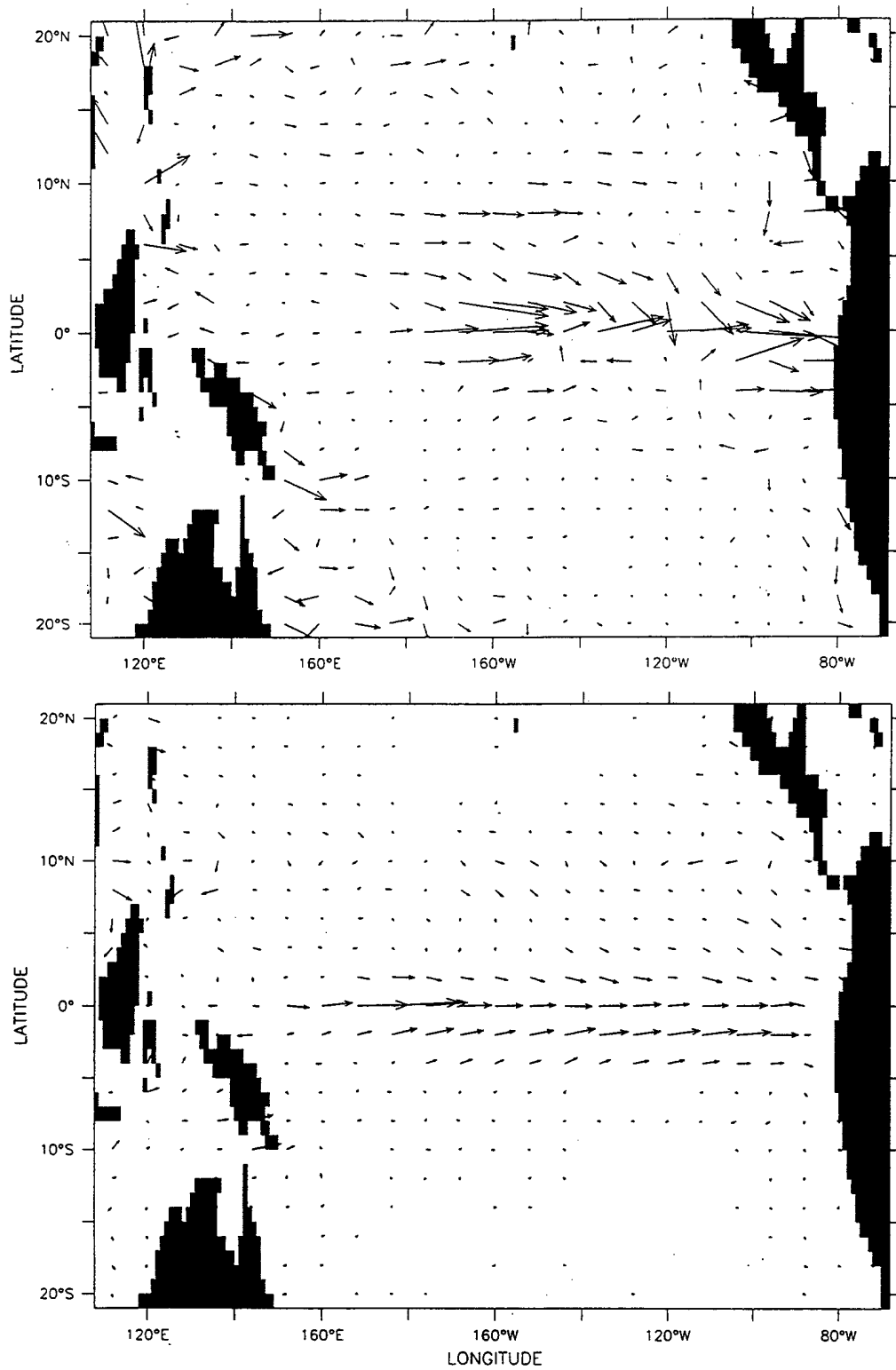


Figure 19. Covariance of Total ( $u$  and  $v$ ) Velocity ( $\text{cm}^2 \text{s}^{-2}$ ): Drifter Data (top) and Model Output (bottom).



→ 21.0  
 Figure 20. Covariance of Velocity and SST ( $\text{cm s}^{-1} \text{ } ^\circ\text{C}$ ): Drifter Data (top) and Model Output (bottom).



## V. LAGRANGIAN STATISTICS

The Eulerian statistics presented previously do not take full advantage of the particle-path (trajectory) nature of the drifter data. Indeed, Lagrangian statistics that describe the decorrelation time and length scales, along with the strength of the turbulent dispersion (i.e., the diffusivity), by following the horizontal particle paths has been a primary focus of open-ocean drifter experiments (Poulain and Niiler, 1989; Paduan and Niiler, 1993).

The large spatial and temporal extent of the drifter data set makes it possible to examine Lagrangian statistics of the tropical Pacific surface circulation. Poulain (personal communication, 1997) has made preliminary calculations of these quantities for the drifter data. This section presents the Lagrangian autocorrelation, time and length scales, and diffusivity based on particle paths created from the model velocity fields, for comparison with the drifter-based results. Statistical methods used here have been presented by Davis et al. (1996), Poulain and Niiler (1989), and Paduan and Niiler (1993), among others.

Model velocity fields were used to produce simulated Lagrangian trajectories for comparison with actual drifter trajectories. An advantage of model-based trajectories is the ability to initialize the trajectories at any time/space point. In this study, two sample initialization grids were

chosen. One released particles at 460 uniformly spaced locations in the model grid using the 2° by 8° spacing of the Eulerian comparisons described earlier. The second data set consisted of 280 trajectories initiated at the actual deployment locations of the WOCE/TOGA drifters during the period September 1992 to October 1994. In this non-uniform case, all trajectories were initialized at the start of the model period, as was also the case for the uniform grid. Trajectories themselves (Figure 21) were obtained by using a fourth-order Runge-Kutta method (Appendix) as used by Hofmann et al. (1991). Lagrangian autocovariance and diffusivity functions from individual trajectories were ensemble-averaged according to mean positions (Figure 22) in latitude bands of 22.5°N to 22.5°S, in 5° bands. The resulting Lagrangian statistics are described below and are listed in Table I and Table II.

In a comparison of trajectories of the Pan-Pacific Surface Current Study (PPCS; Figure 8) and the uniform and non-uniform data (Figure 21), the most significant features in common are the concentration of tracks in the western Pacific, at around 140°E, between the equator and 5°N in the uniform and non-uniform fields, and between the equator and 5°S in the PPCS. Also, both model- and drifter-derived trajectories exhibit a paucity of tracks in the central basin along the equator. Track density is a function of deployment strategy and mean circulation patterns, primarily equatorial

divergence. This is made clear by the comparison of the uniform and non-uniform data sets in Figure 21. Although the very high concentration of trajectories in the western Pacific is largely the result of large numbers of deployments in that region, the uniformly deployed data set shows there to be convergence in the model velocities in that region. Similarly, the additional equatorial deployments in the non-uniform data set are not enough to overcome the strong divergence in that region.

#### A. LAGRANGIAN AUTOCOVARANCE

The Lagrangian autocovariance is defined as the average time-lagged covariance of velocity along a trajectory (Davis, 1993):

$$R_{ij}(\tau, T, x_0, t_0) \equiv \frac{1}{T} \int_{t_0}^{t_0+T} u'_i(t, x_0, t_0) u'_j(t+\tau, x_0, t_0) dt \quad i = u, v; j = u, v$$

where  $u'$  is the perturbation velocity and  $T$  is the length of the time series. The velocity components  $u$  and  $v$  refer to the velocity at time  $t$  of the drifter passing through  $x_0$  at the initial time  $t_0$ . If the velocity field is assumed to be stationary and homogeneous, as was done in this study, then dependence upon the initial point  $x_0$  vanishes and the equation

simplifies to:

$$R_{ij}(\tau, T) = \frac{1}{T} \int_0^T u_i'(t) u_j'(t+\tau) dt \quad i = u, v; j = u, v.$$

The zero-lag autocovariances  $R_{uu}(0, T)$  and  $R_{vv}(0, T)$  are the velocity variances in the east-west and north-south directions, respectively, for the time series of length  $T$ .

Lagged autocovariance functions were computed for each trajectory and regional (zonal) statistics were estimated by ensemble averaging all functions whose mean position fell within  $5^\circ$  latitude bands. For ensemble averages, the individual autocorrelation functions were calculated by normalizing the autocovariance by the variance before ensemble averaging.

Ensemble averages, by latitude band, of the autocorrelation functions are shown in the center panel of Figures 22 - 30 for the uniform distribution and Figures 31 - 39 for the non-uniform distribution. The standard deviation of the mean autocorrelation function is shown for each time lag. For both the uniform and non-uniform ensemble-averaged time-lagged autocorrelation functions,  $v$  decays faster in all cases, but error bars indicate that the averages are not well defined.  $R$  should smoothly asymptote to zero in the presence of stationary, homogeneous turbulence; the degree to which the functions fail to asymptotically approach zero provides a

measure of the non-homogeneity of the field. Most likely, deviations from the expected functional forms reflects inadequate description of the mean currents and their horizontal shear (Bauer et al., 1997) so that a single turbulent (mesoscale) time scale is not appropriate.

The ensemble-averaged time-lagged autocorrelation functions based on the uniform trajectories are well-behaved, with some indications of multiple time scales in the  $v$  component of 7.5°S to 2.5°S and the 2.5°N to 7.5°N bins. The bin spanning the equator, from 2.5°S to 2.5°N, shows a more rapid decay of the  $v$  component than other bins. The ensemble-averaged time-lagged autocorrelation functions based on the non-uniform trajectories show similar behavior in similar bins.

## B. INTEGRAL TIME AND LENGTH SCALES

The Lagrangian integral time and space scales are the time and distance over which a drifter remembers its path, and are defined by (Poullain and Niiler, 1989):

$$T_i^L \equiv \frac{1}{\langle u_i'^2 \rangle} \int_0^t R_{ij}(\tau) d\tau$$

$$L_i^L \equiv \frac{1}{[\langle u_i'^2 \rangle]^{1/2}} \int_0^t R_{ij}(\tau) d\tau = [\langle u_i'^2 \rangle]^{1/2} T_i^L$$

The zonal and meridional autocorrelation functions computed here asymptotically approach zero, but in some cases do not cross zero. Therefore, the choice of e-folding scale rather than zero crossings was made to provide consistent estimates of time and length scales. Furthermore, the method used to determine the time scale selected the closest lag to the integral e-folding time resulting in a discretization of the estimates into the 3-day time steps of the trajectory data.

The ensemble-averaged time and length scales for each latitude band, by uniform and non-uniform deployment, are shown in Figures 41 and 42, respectively, and listed in Table I and Table II. In the tables, the range estimates derive from the e-folding times of the ensemble averaged functions plus and minus one standard deviation.

Zonal integral time scales for the uniform field vary between 18 days, for the southernmost and northernmost bands, and 51 days for the 12.5°N to 7.5°N band. Meridional time scales, conversely, vary between 6 or 9 days in the seven innermost bands, to 12 days at the northern- and southernmost bands. Poulain (personal communication, 1997), reports a zonal integral time scale (Figure 43) of about 10 days, and a meridional time scale (Figure 44) of about 5 days, throughout four seasonal ensembles. Zonal and meridional integral time scales for the non-uniform fields reflect the same distribution as the uniform field, despite the large

differences in trajectories per band for several latitude bands.

Average length scales of the uniform field for east-west and north-south drifter motions are 130 km and 29 km, respectively, and are consistently larger in the east-west than in the north-south direction. Length scales seem more sensitive to drifter concentration than time scales. Zonal length scales for the uniform field vary between 24 km in the southernmost band, consistently increasing to the north, to a high of 283 km in the 12.5°N to 7.5°N band. Meridional length scales vary between 14 to 20 km in the four southernmost bands, then between 28 and 35 km in the next four bands to the north, and reaches a maximum of 67 km at the northernmost band.

### C. DIFFUSIVITY

The diffusivity  $K$ , which is defined as the time rate of change of the displacement covariance, is related to the integral of the Lagrangian autocovariance, in the stationary, homogeneous regime by (Poulain and Niiler, 1989):

$$K_{ii}(t) = \frac{1}{2} \int_0^t R_{ii}(\tau) d\tau.$$

The diffusivities  $K_{uu}$  and  $K_{vv}$  are computed from the individual

autocovariance functions without normalization, and then ensemble-averaged by latitude bands for each lag as for  $R$  (bottom panel, Figures 23 - 40; note that large variations in  $K$  necessitate different ordinate scales for some figures).

To represent the theoretical asymptotic values for  $K_{uu}$  and  $K_{vv}$ , values were selected at the integral times computed from the normalized  $R_{uu}$  and  $R_{vv}$  above. These diffusivity values are an approximation to the asymptotic solution at the time lag corresponding to the integral time scale. These are plotted versus latitude in Figure 45 and listed in Table I and II. Range values derive from the diffusivities plus or minus one standard deviation for the time lags corresponding to the integral time scales.

In the uniform data the zonal component of diffusivity  $K_{uu}$  dominates the results with maximum values ranging from  $0.2 \times 10^3 \text{ m}^2\text{s}^{-1}$  at high latitudes to  $12 \times 10^3 \text{ m}^2\text{s}^{-1}$  near the equator. Typical magnitude of the meridional diffusivity  $K_{vv}$  ranges from about  $0.1 \times 10^3 \text{ m}^2\text{s}^{-1}$  at  $20^\circ\text{S}$  to  $2.2 \times 10^3 \text{ m}^2\text{s}^{-1}$  at  $20^\circ\text{N}$ . Poulain (personal communication, 1997) report maximum values of the zonal component of diffusivity (Figure 46) of  $50 \times 10^3 \text{ m}^2\text{s}^{-1}$  at high latitudes to  $150\text{-}200 \times 10^3 \text{ m}^2\text{s}^{-1}$  near the equator, and a typical magnitude of meridional diffusivity (Figure 47) of  $10\text{-}20 \times 10^3 \text{ m}^2\text{s}^{-1}$ . Bauer et al. (1997) report

$K_{uu}$  and  $K_{vv}$  values in the SEC of  $7 \times 10^3 \text{ m}^2\text{s}^{-1}$  and  $3 \times 10^3 \text{ m}^2\text{s}^{-1}$ , respectively; they report  $K_{uu}$  and  $K_{vv}$  values in the NECC of  $15 \times 10^3 \text{ m}^2\text{s}^{-1}$  and of  $4 \times 10^3 \text{ m}^2\text{s}^{-1}$ , respectively.

#### D. POLARIZATION

A Lagrangian measure of the polarization or mean angular momentum  $J$  is given by the integral of the covariance functions (Poulain and Niiler, 1989):

$$J(t) = \int_0^t R_{uv}(\tau) - R_{vu}(\tau) d\tau$$

The direction of rotation of the trajectories can be determined from combinations of the covariance functions between zonal and meridional currents, which provides a characterization of the eddy field. Positive  $J$  indicates cyclonic (counterclockwise) rotation, while negative  $J$  indicates anticyclonic rotation. Values of  $J$  are shown in the top panel of the uniform (Figures 23 - 31) and non-uniform (Figures 32 - 40) averaged ensembles. Because these functions depend on the Lagrangian autocovariance functions and the assumptions of homogeneity and stationarity, values for times greater than the integral time scales should be ignored. For the long model trajectories used here and the

rather large areas that these statistics represent, there is no evidence for significant bias toward clockwise or counterclockwise rotations in the trajectories.

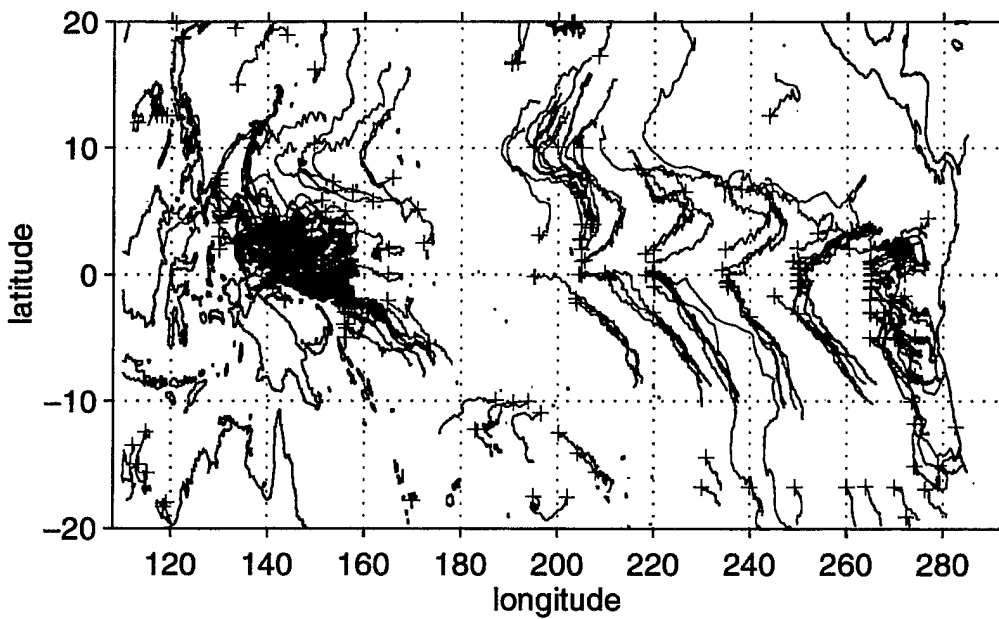
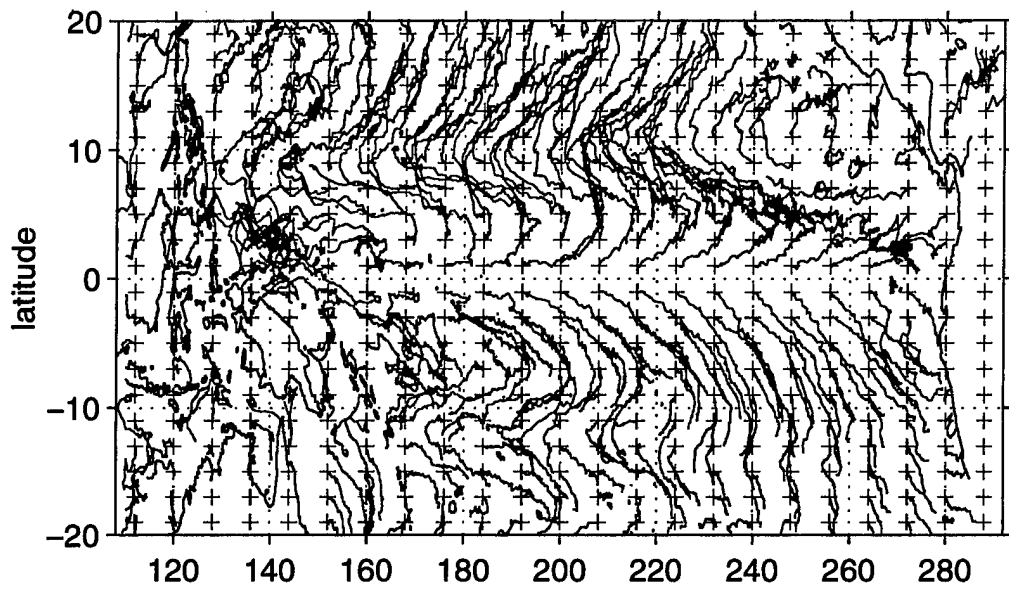


Figure 21. Resultant trajectories induced by POP model velocity fields from 460 uniformly spaced initial positions (top) and 280 non-uniformly spaced initial positions (bottom). Crosses are initial positions.

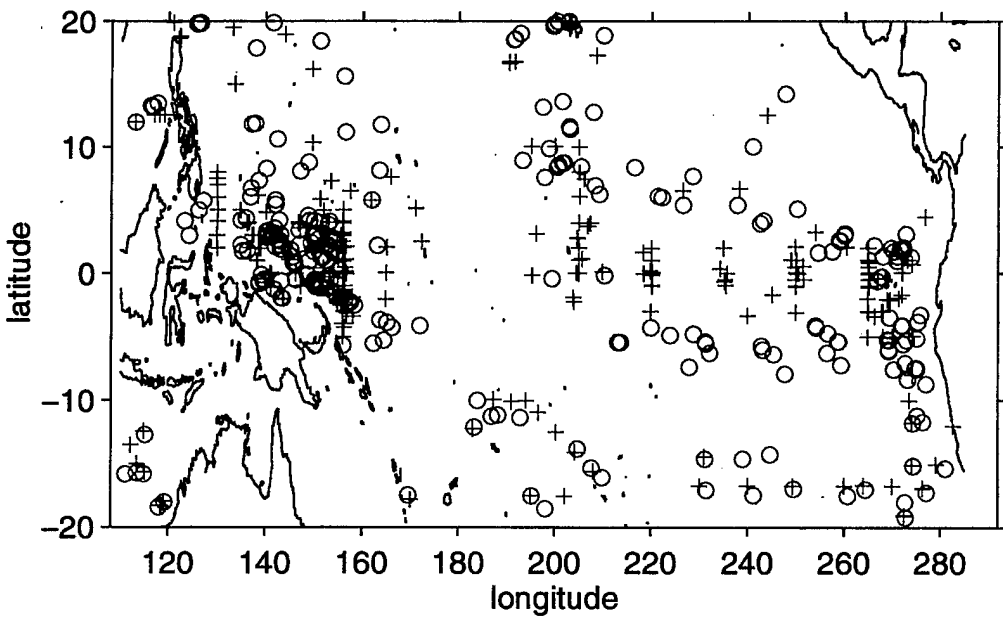
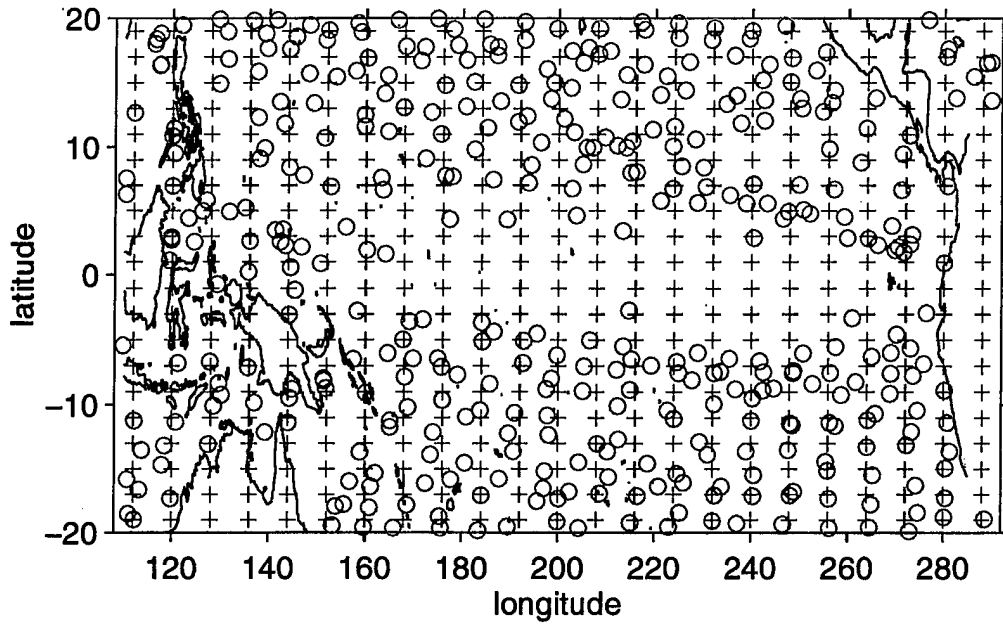


Figure 22. Mean and initial positions for 460 uniformly spaced initial positions (top) and 280 non-uniformly spaced initial positions (bottom). Crosses are initial positions, circles are mean positions.

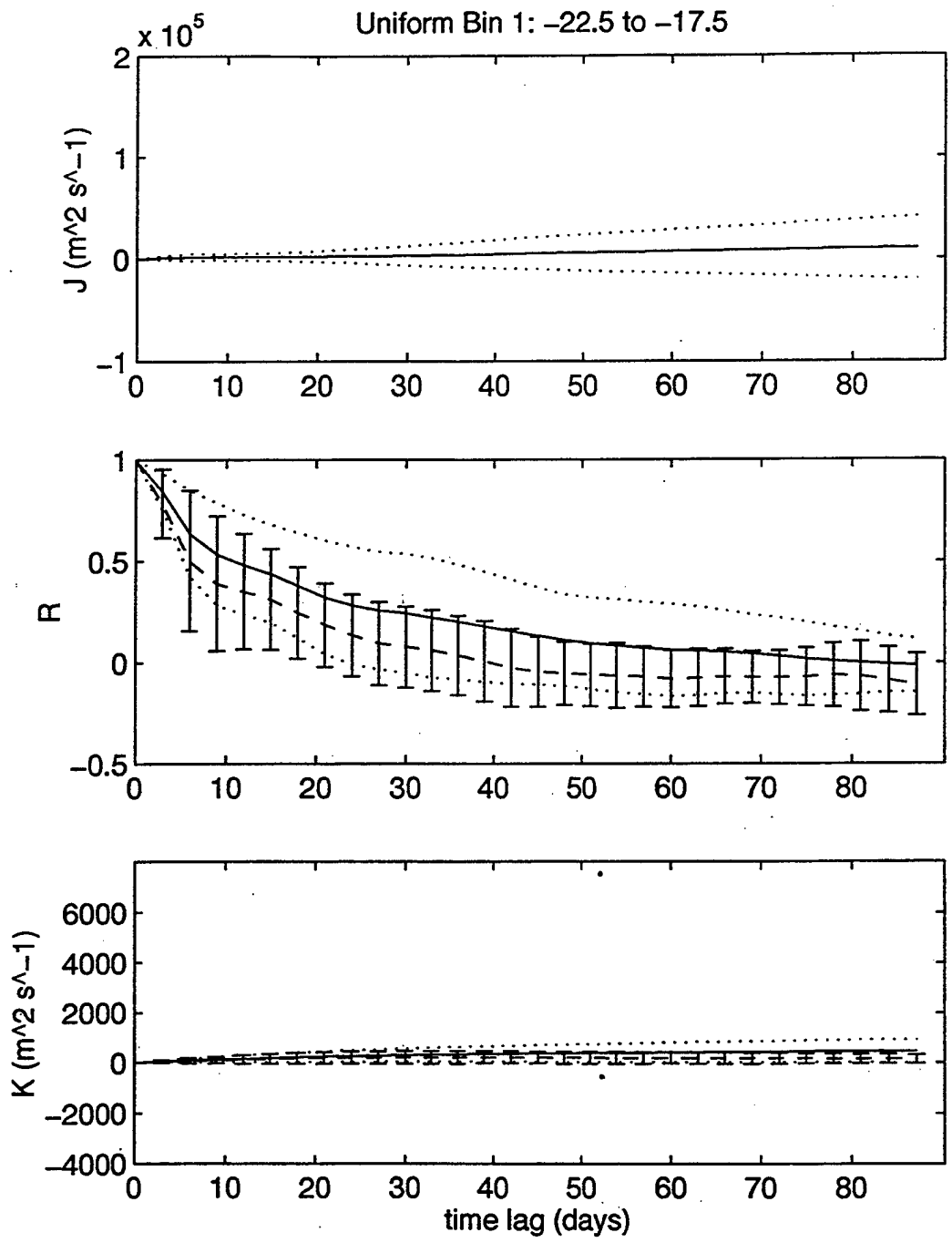


Figure 23. Ensemble Averaged Uniform Deployments. Latitude Band 22.5°S - 17.5°S. Polarization ( $10^7 \text{ m}^2 \text{ s}^{-1}$ ) or measure of angular momentum  $J$  (top); autocovariance  $R_{uu}$  (solid line, error envelopes) and  $R_{vv}$  (dashed line, error bars) (center); diffusivity  $K_{uu}$  ( $\text{m}^2 \text{ s}^{-1}$ ) (solid line, error envelopes) and  $K_{vv}$  (dashed line, error bars) (bottom).

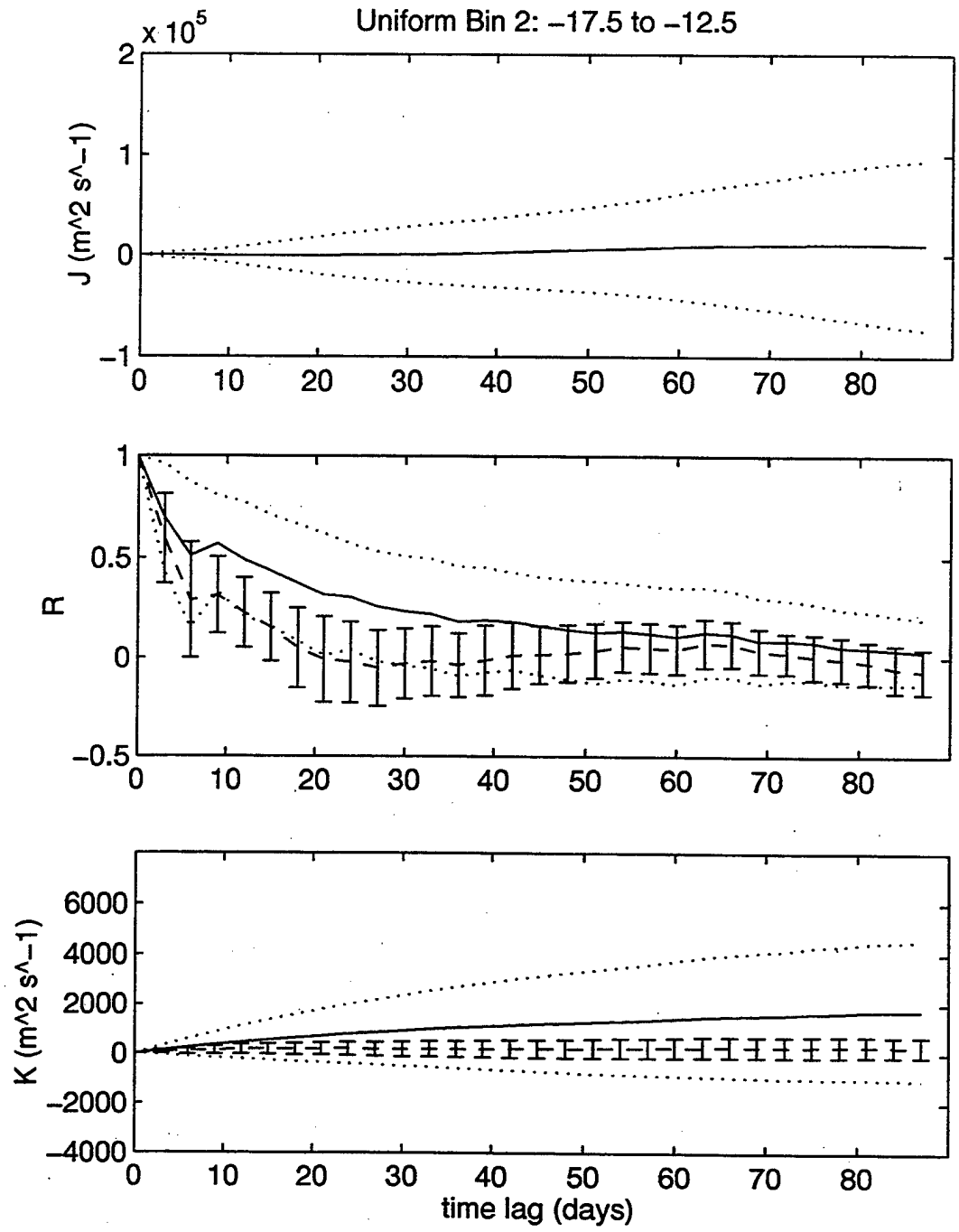


Figure 24. Uniform Deployments. Latitude Band 17.5°S - 12.5°S.

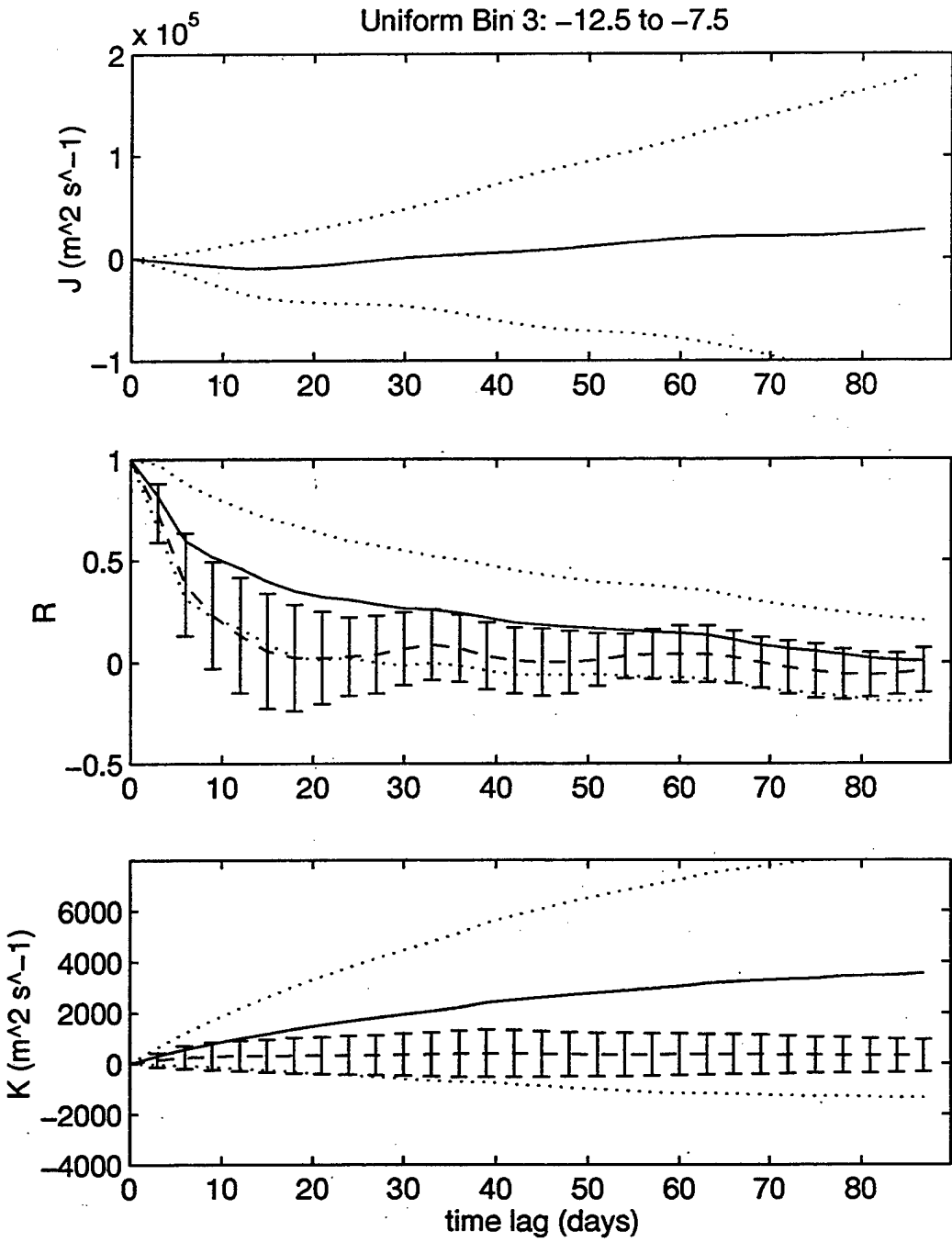


Figure 25. Uniform Deployments. Latitude Band 12.5°S - 7.5°S.

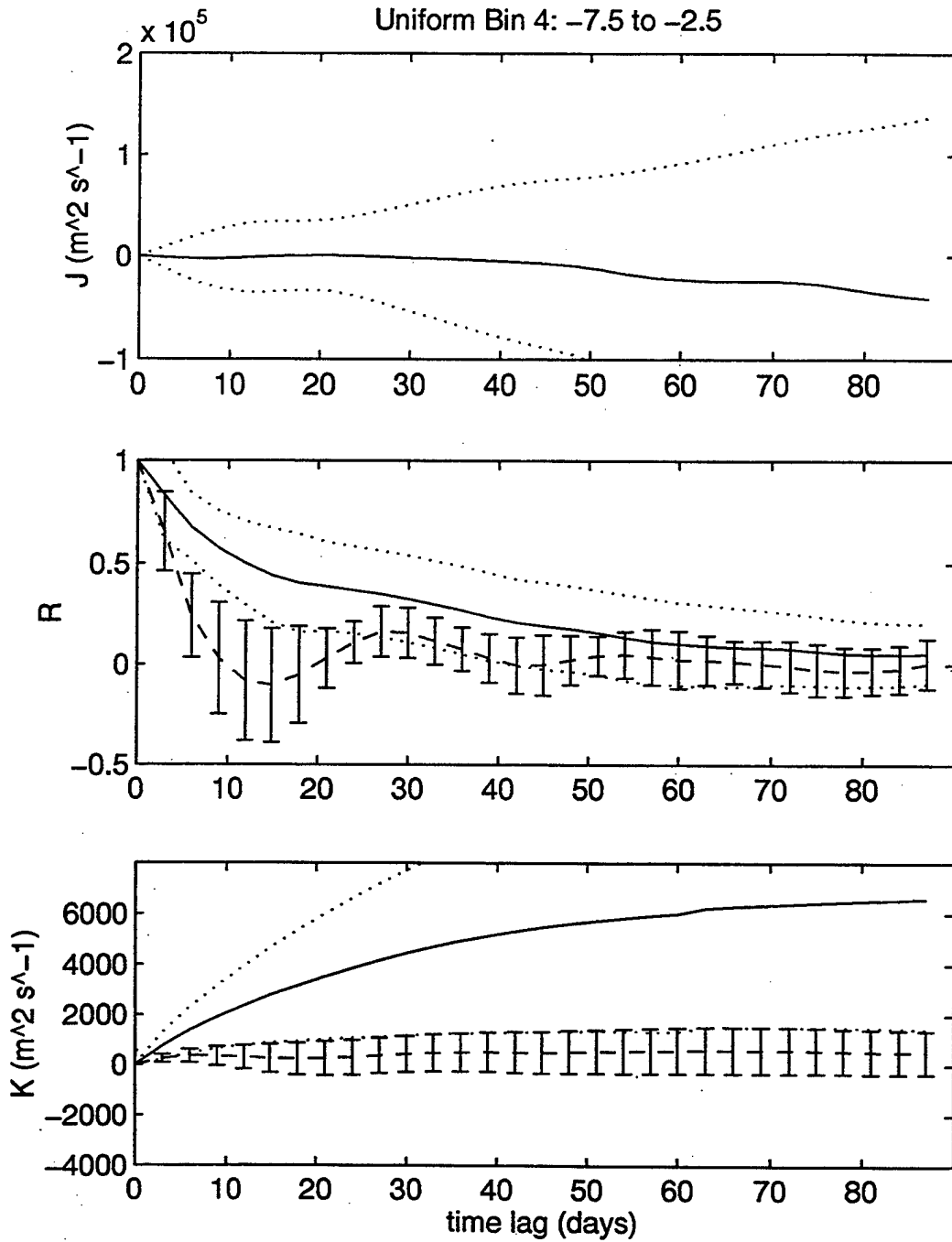


Figure 26. Uniform Deployments. Latitude Band 7.5°S - 2.5°S.

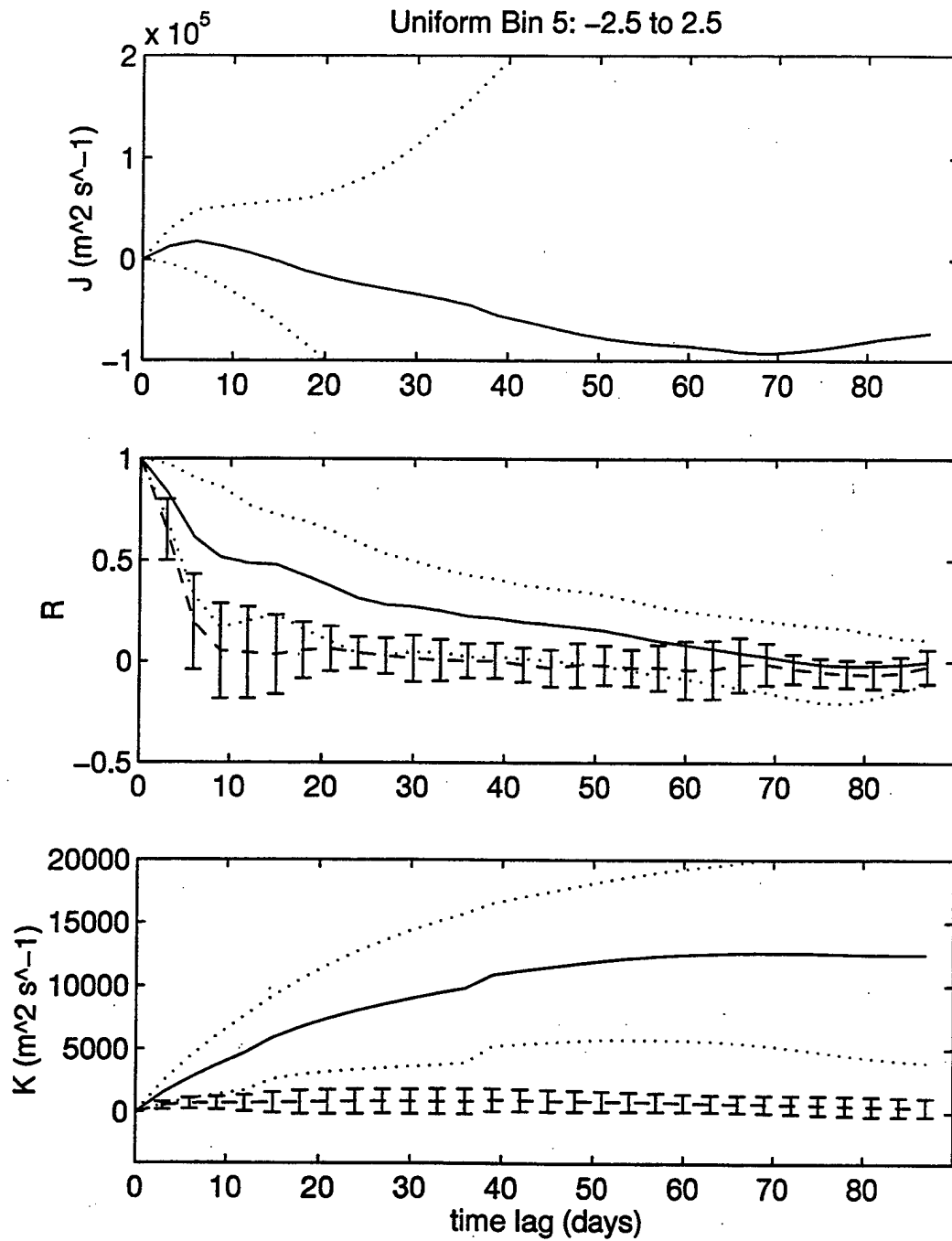


Figure 27. Uniform Deployments. Latitude Band 2.5°S - 2.5°N.

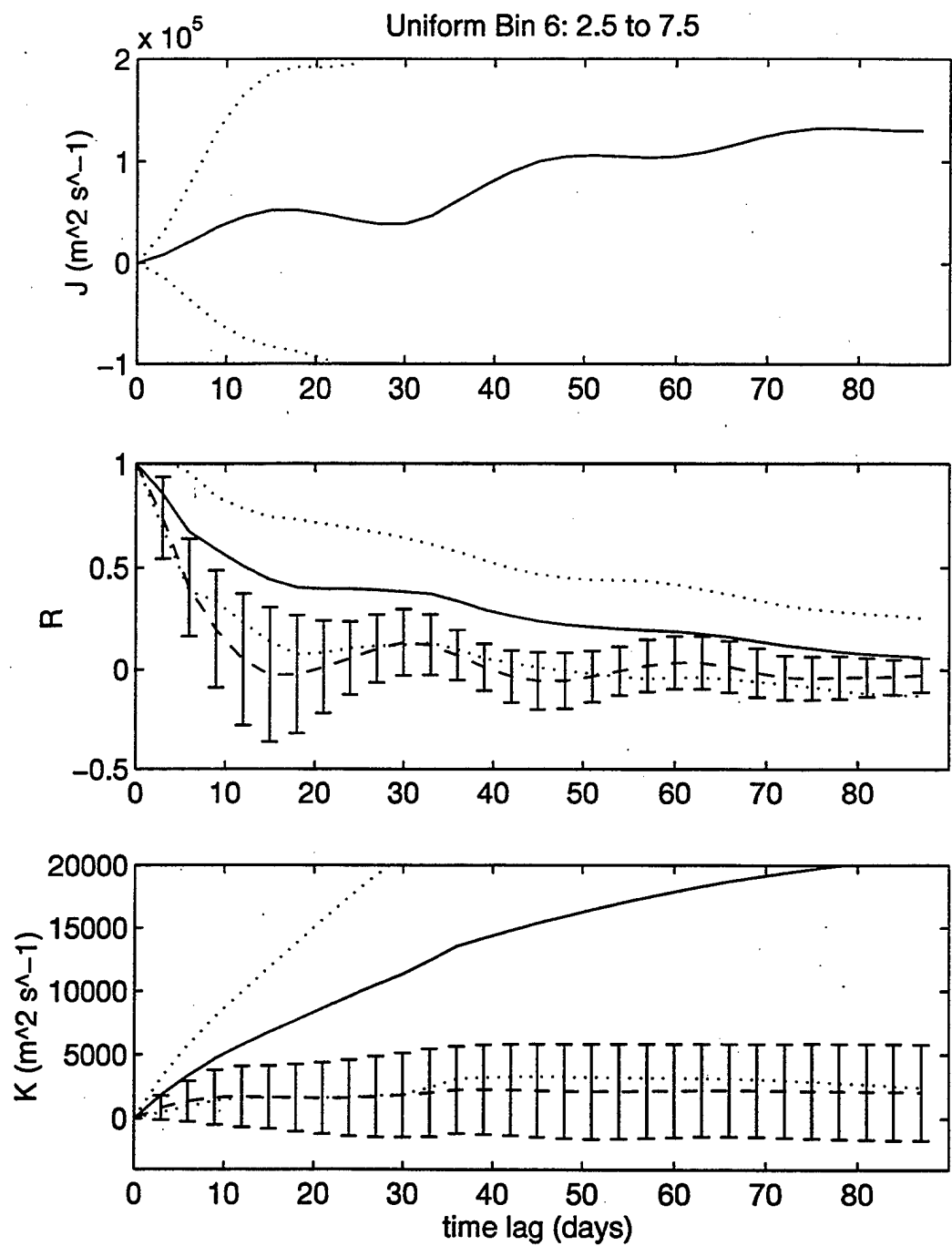


Figure 28. Uniform Deployments. Latitude Band 2.5°N - 7.5°N.

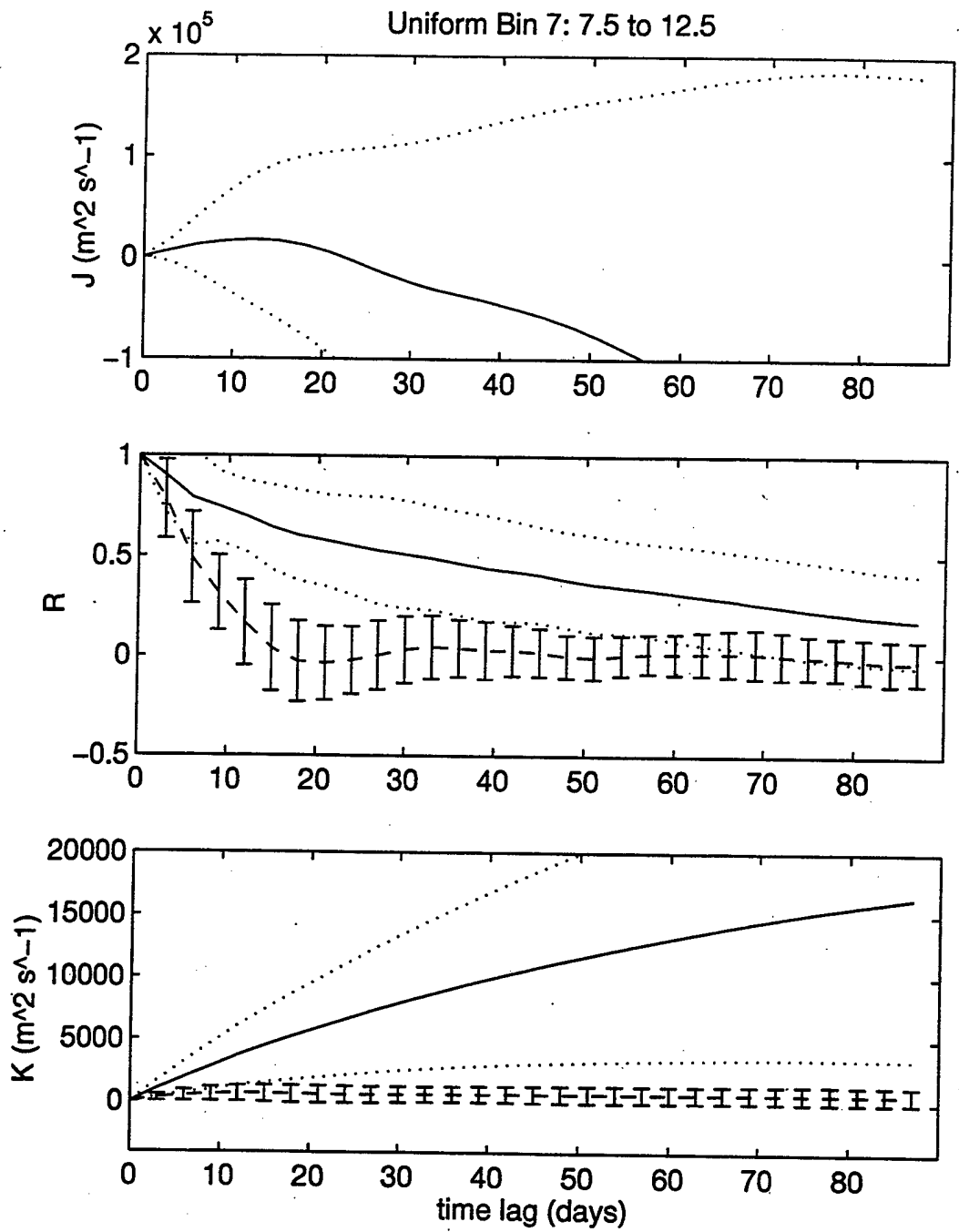


Figure 29. Uniform Deployments. Latitude Band 7.5°N - 12.5°N.

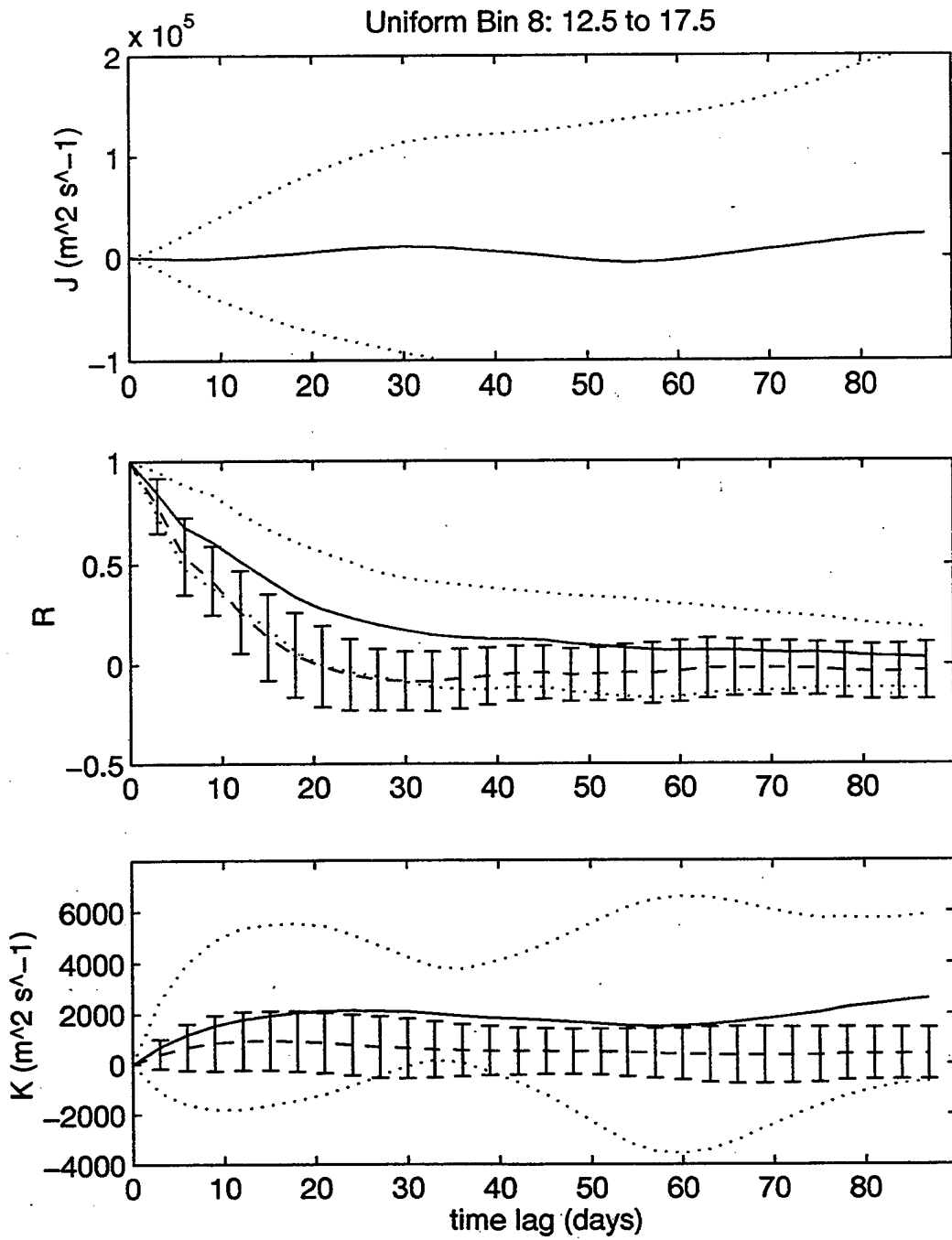


Figure 30. Uniform Deployments. Latitude Band 12.5°N - 17.5°N.

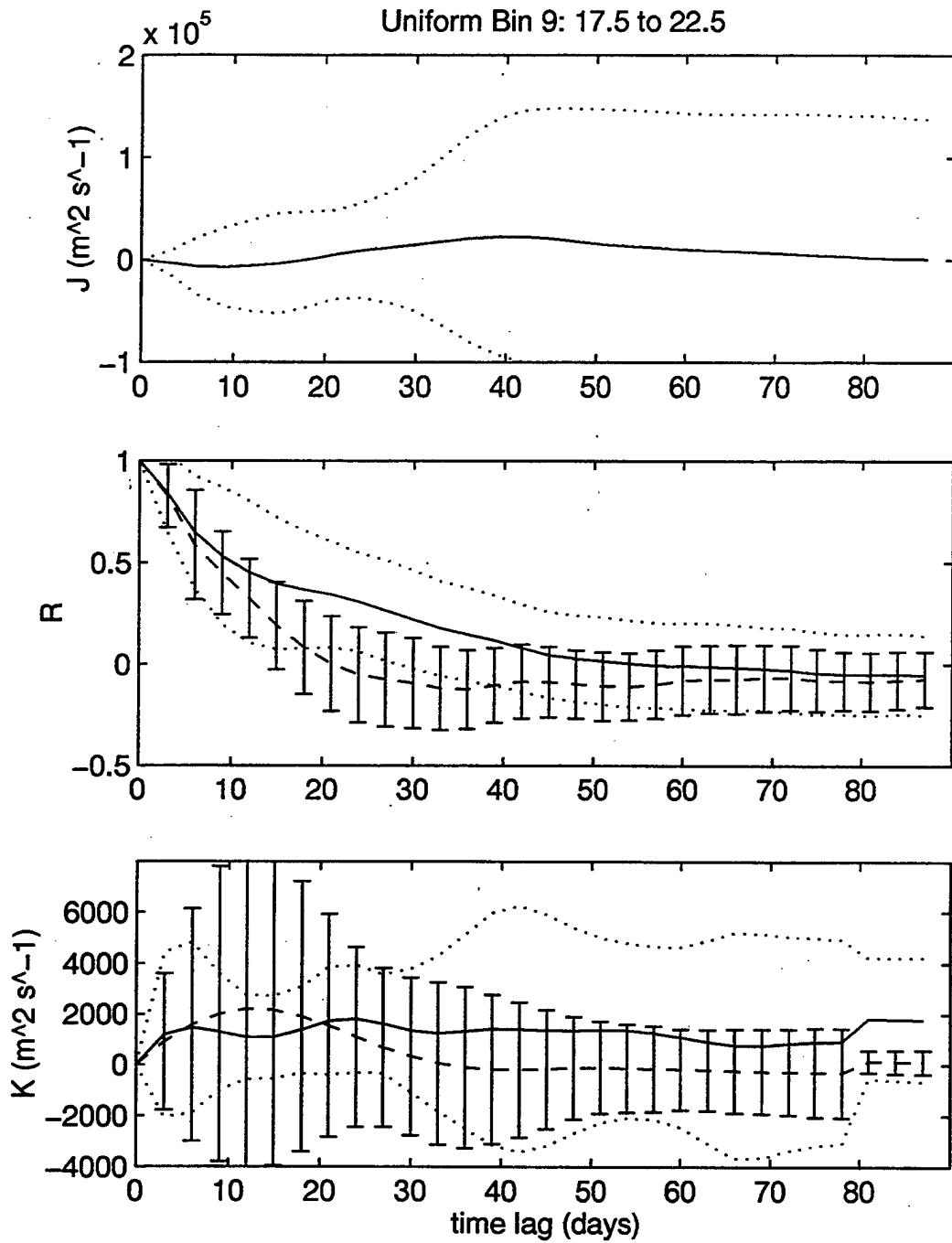


Figure 31. Uniform Deployments. Latitude Band 17.5°N - 22.5°N.

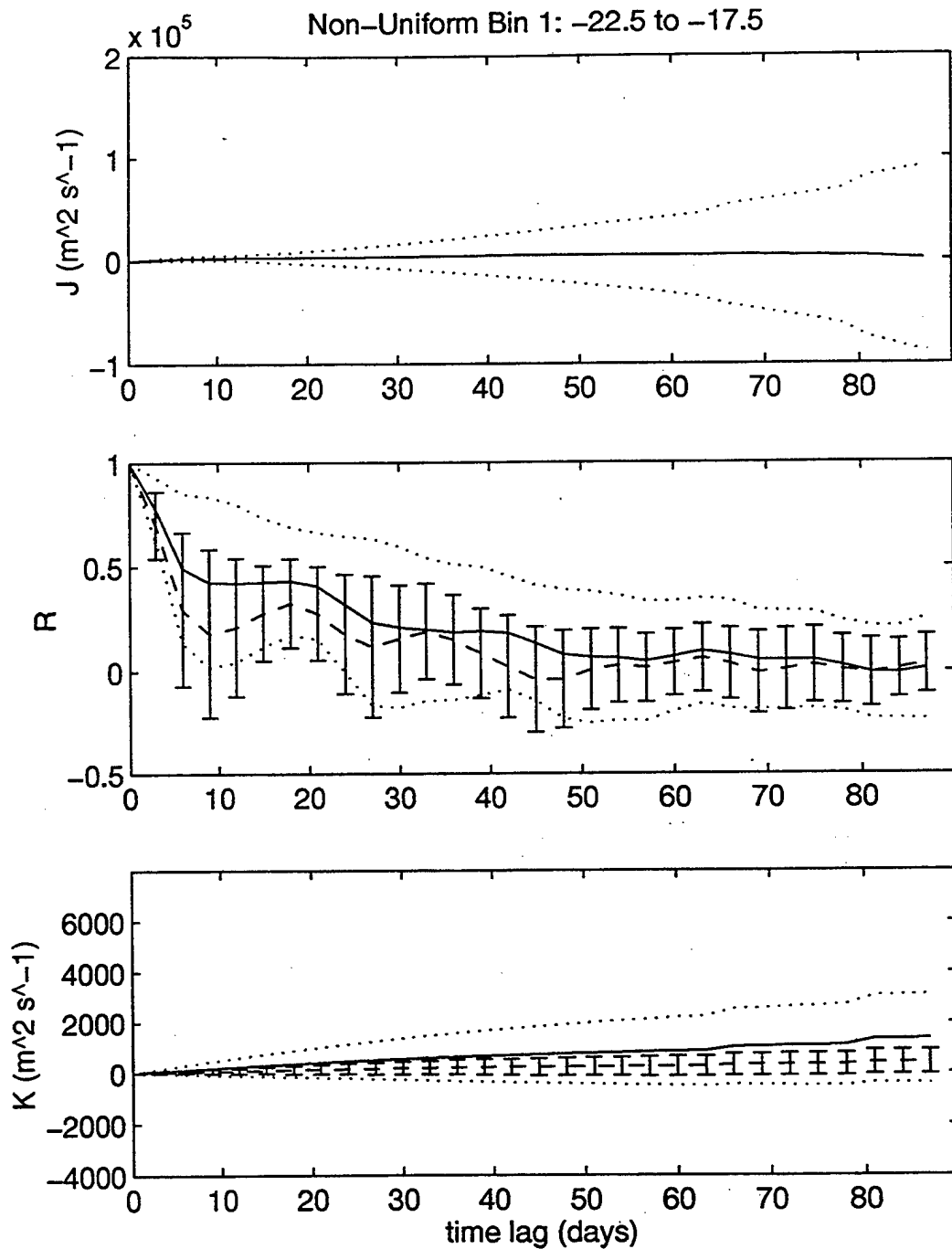


Figure 32. Ensemble Averaged Non-Uniform Deployments. Latitude Band 22.5°S - 17.5°S. Polarization ( $10^7 \text{ m}^2 \text{ s}^{-1}$ ) or measure of angular momentum  $J$  (top); autocovariance  $R_{uu}$  (solid line, error envelopes) and  $R_{vv}$  (dashed line, error bars) (center); diffusivity  $K_{uu}$  ( $\text{m}^2 \text{ s}^{-1}$ ) (solid line, error envelopes) and  $K_{vv}$  (dashed line, error bars) (bottom).

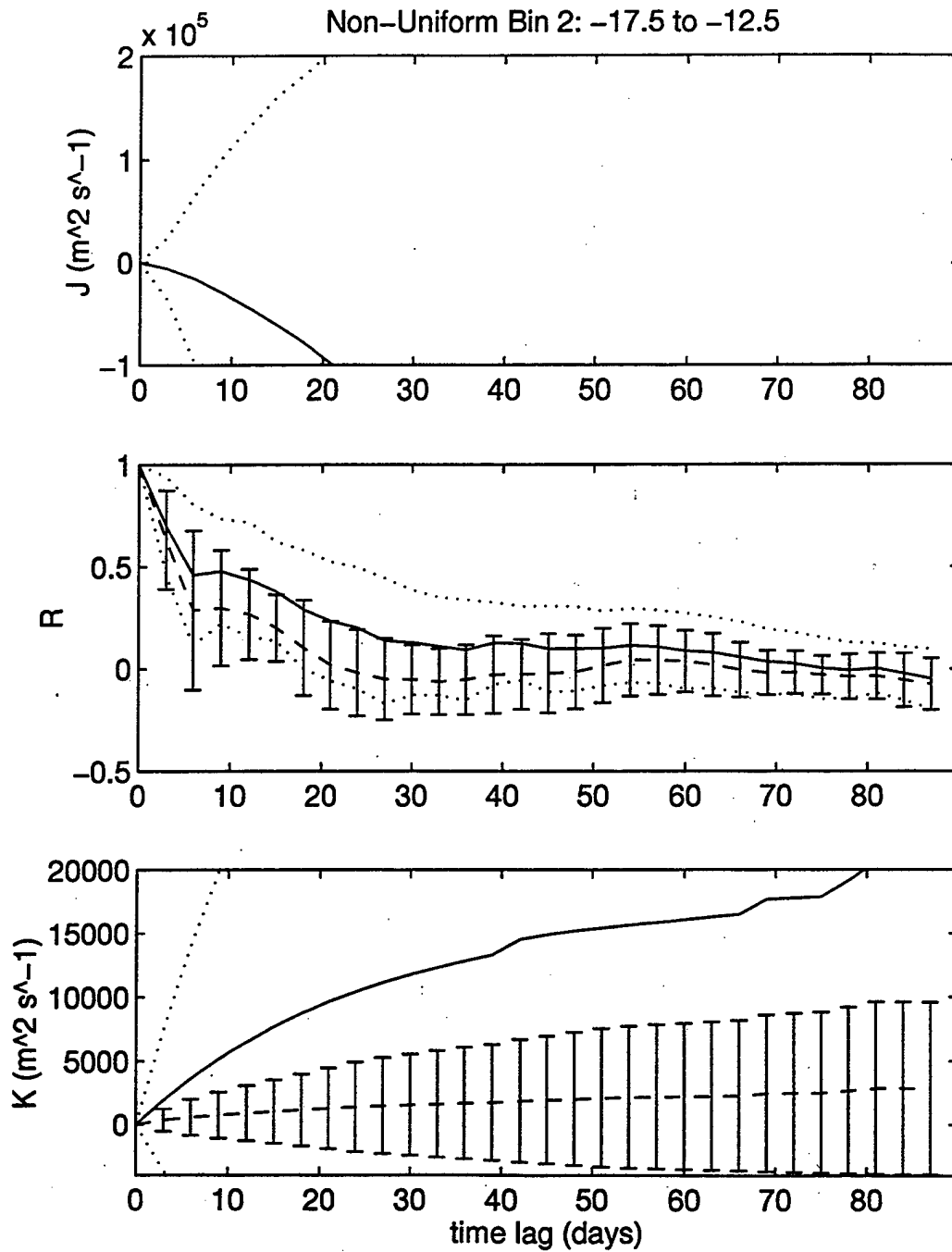


Figure 33. Non-uniform Deployments. Latitude Band 17.5°S - 12.5°S.

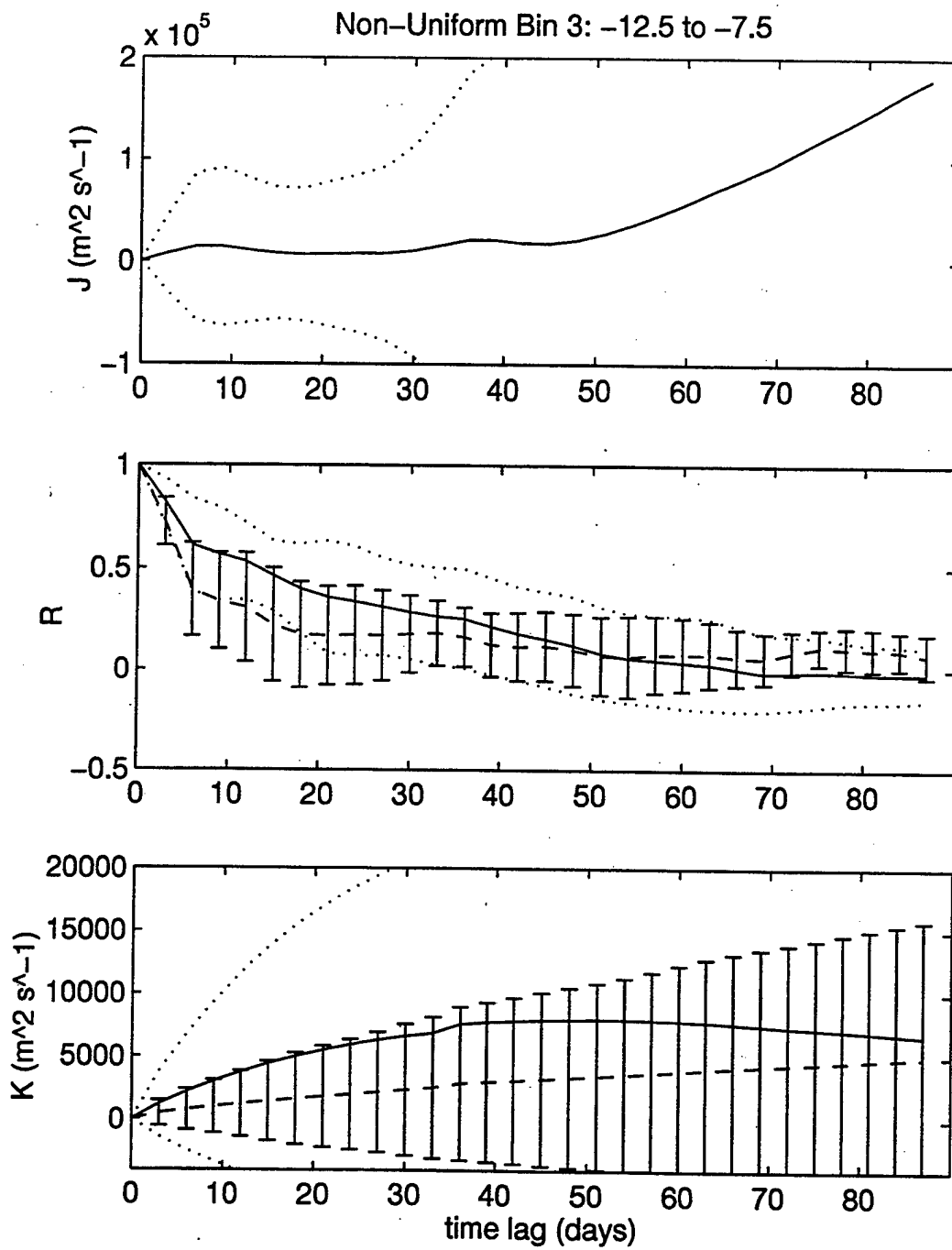


Figure 34. Non-uniform Deployments. Latitude Band 12.5°S - 7.5°S.

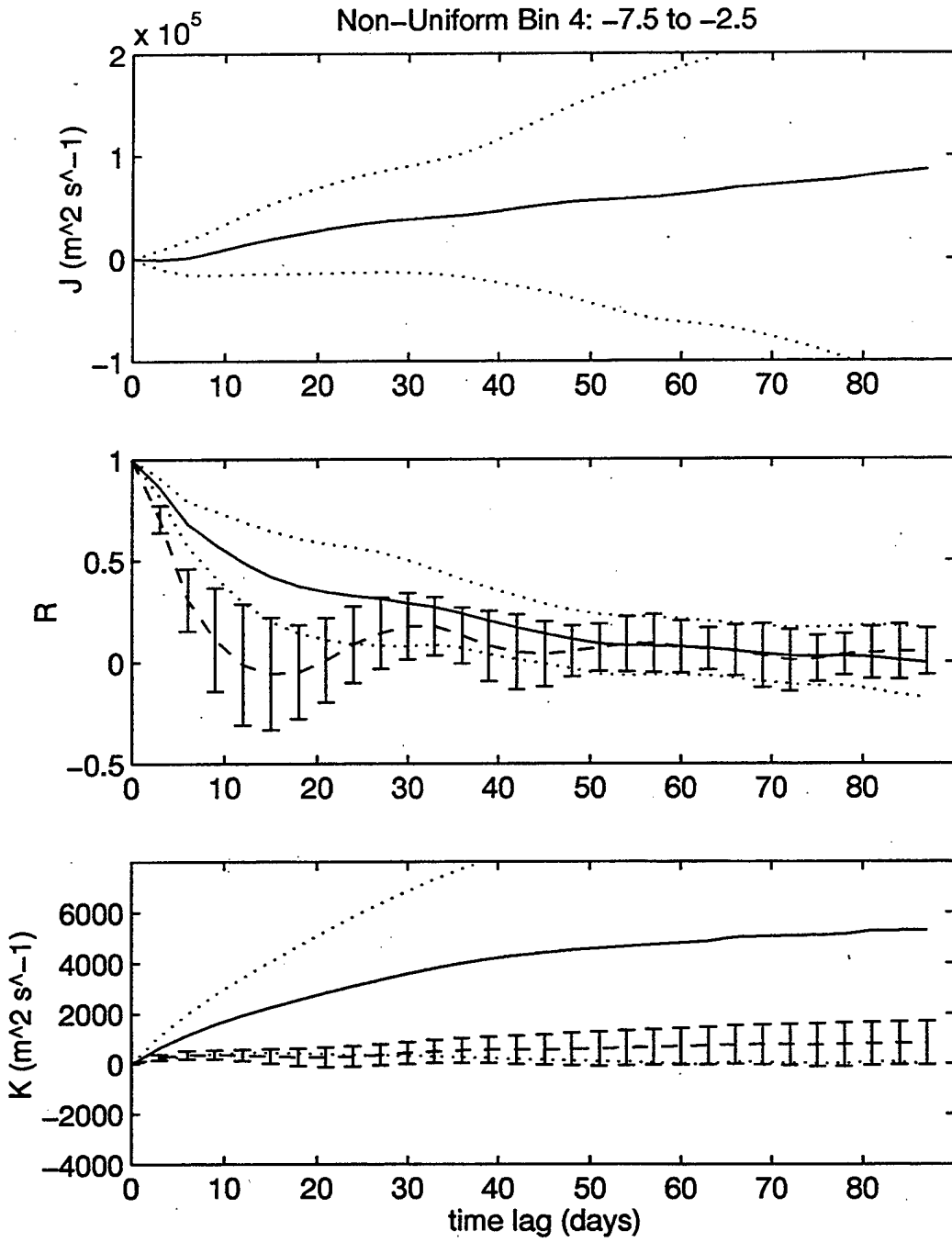


Figure 35. Non-uniform Deployments. Latitude Band 7.5°S - 2.5°S.

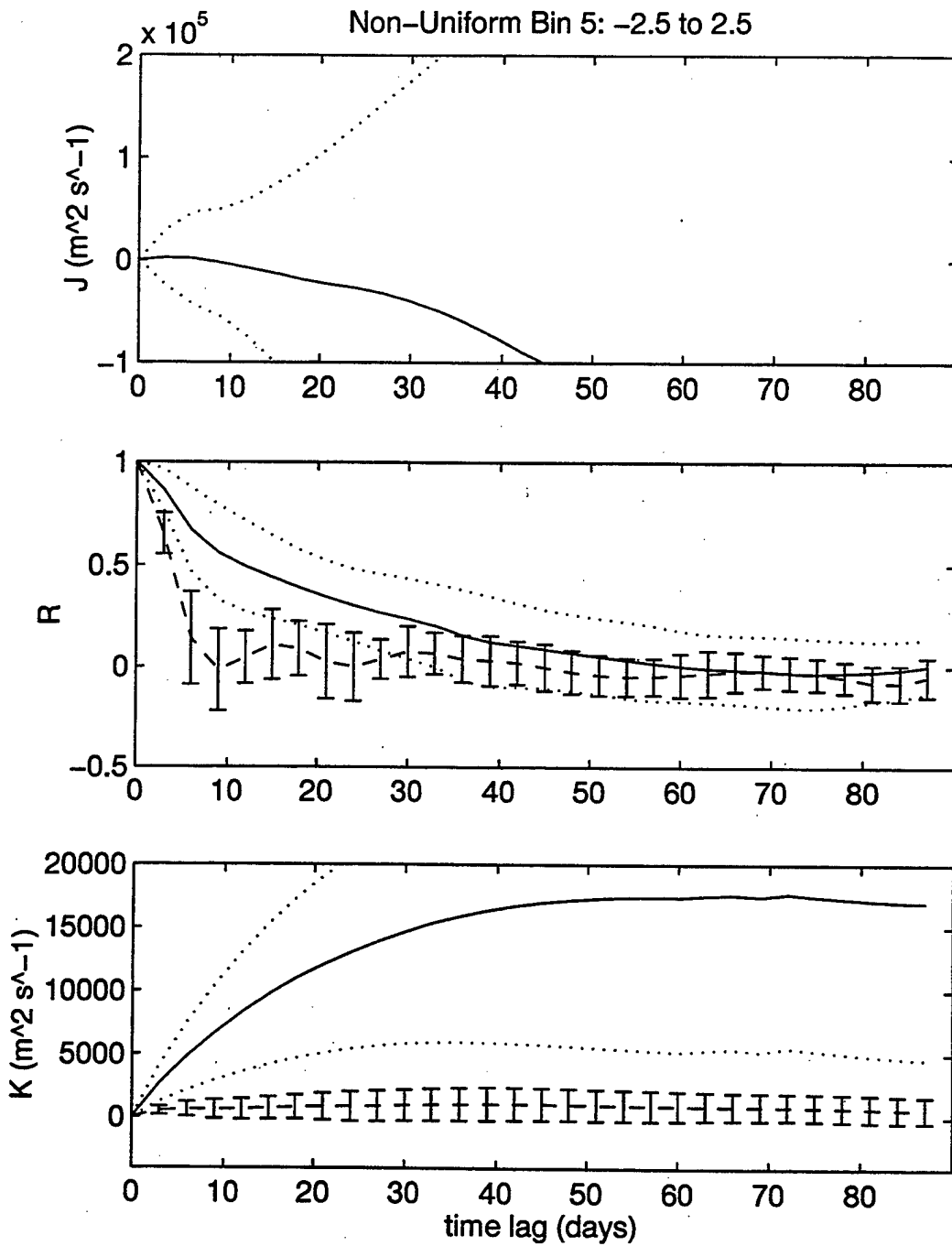


Figure 36. Non-uniform Deployments. Latitude Band 2.5°S - 2.5°N.

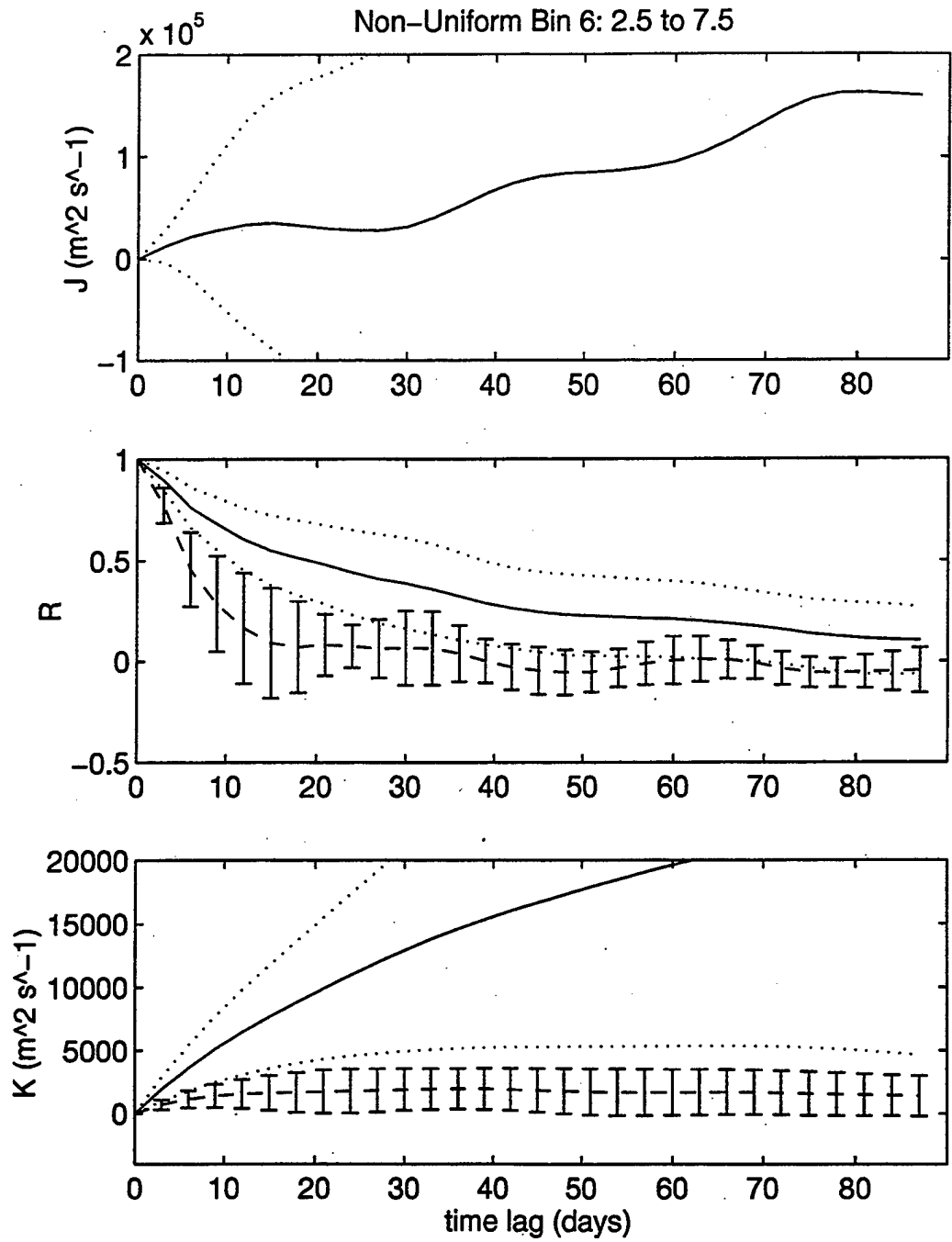


Figure 37. Non-uniform Deployments. Latitude Band 2.5°N - 7.5°N.

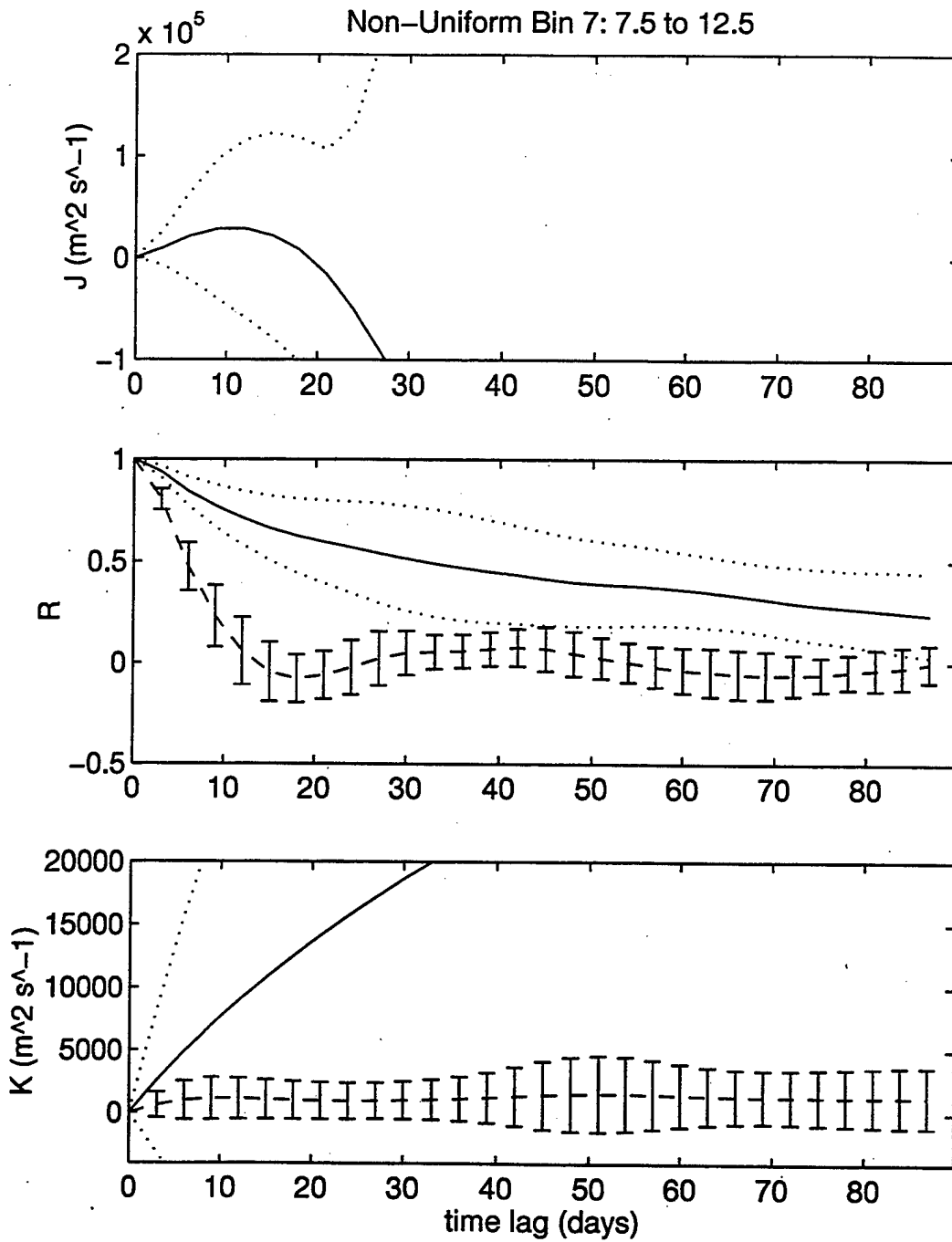


Figure 38. Non-uniform Deployments. Latitude Band 7.5°N - 12.5°N.

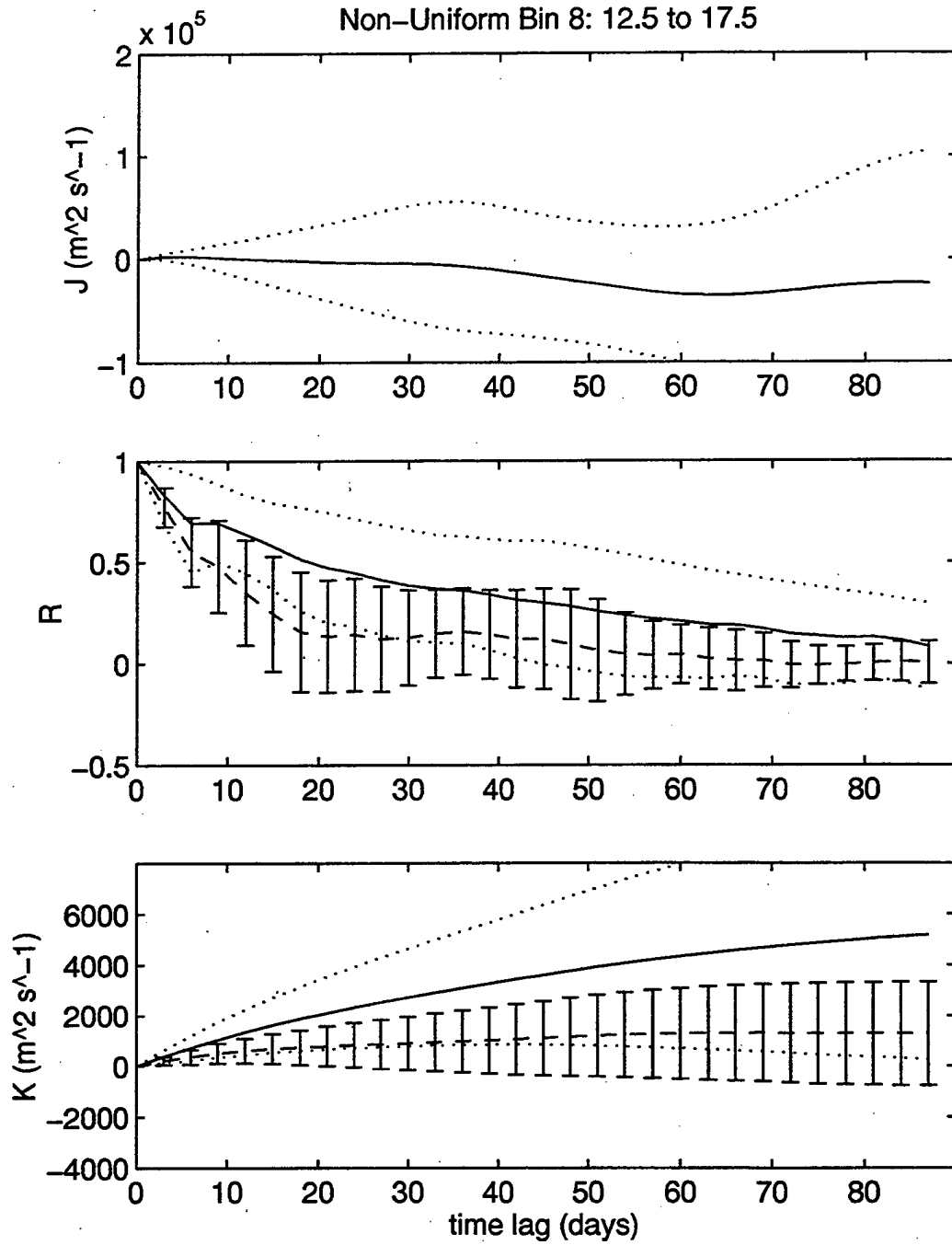


Figure 39. Non-uniform Deployments. Latitude Band 12.5°N - 17.5°N.

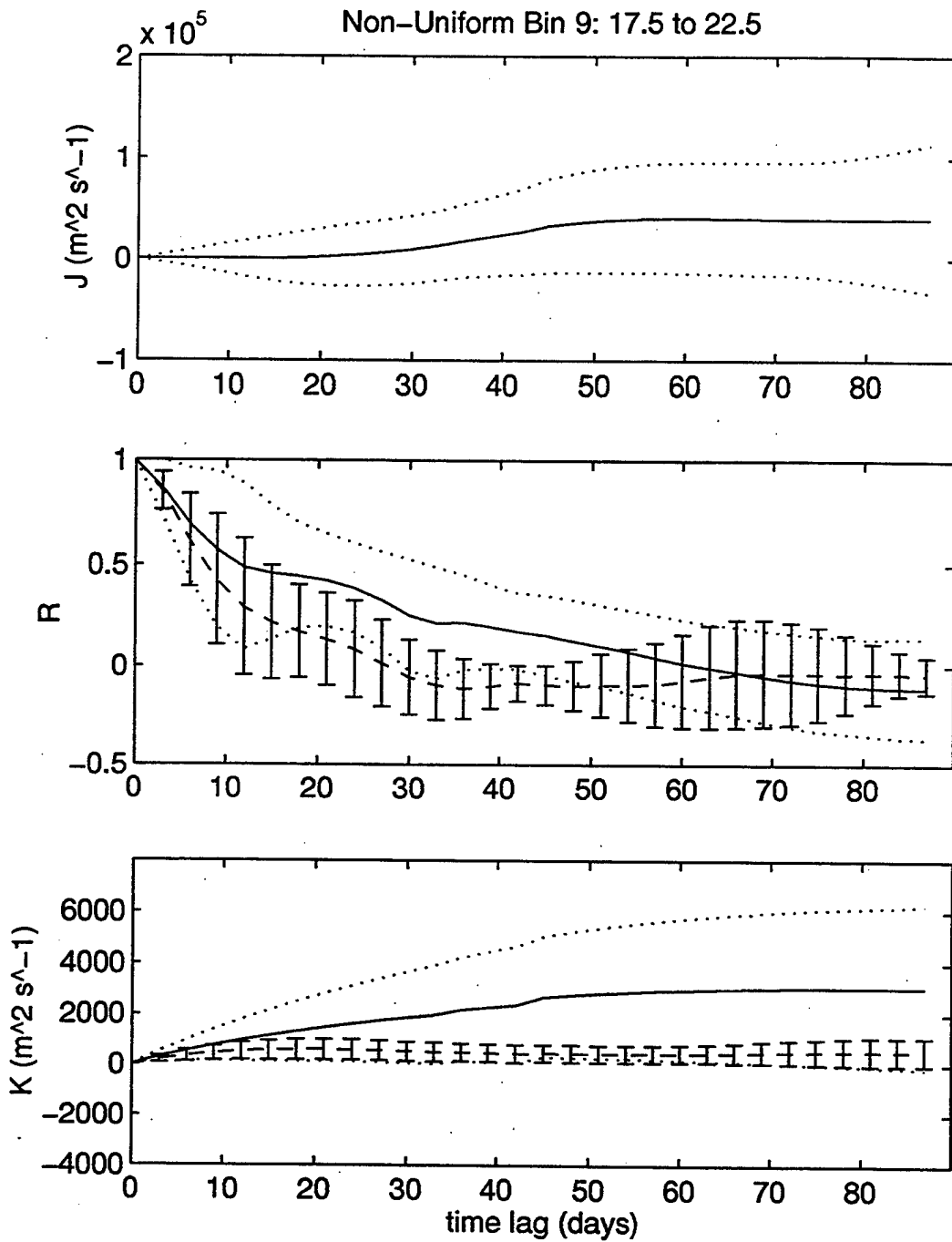


Figure 40. Non-uniform Deployments. Latitude Band 17.5°N - 22.5°N.

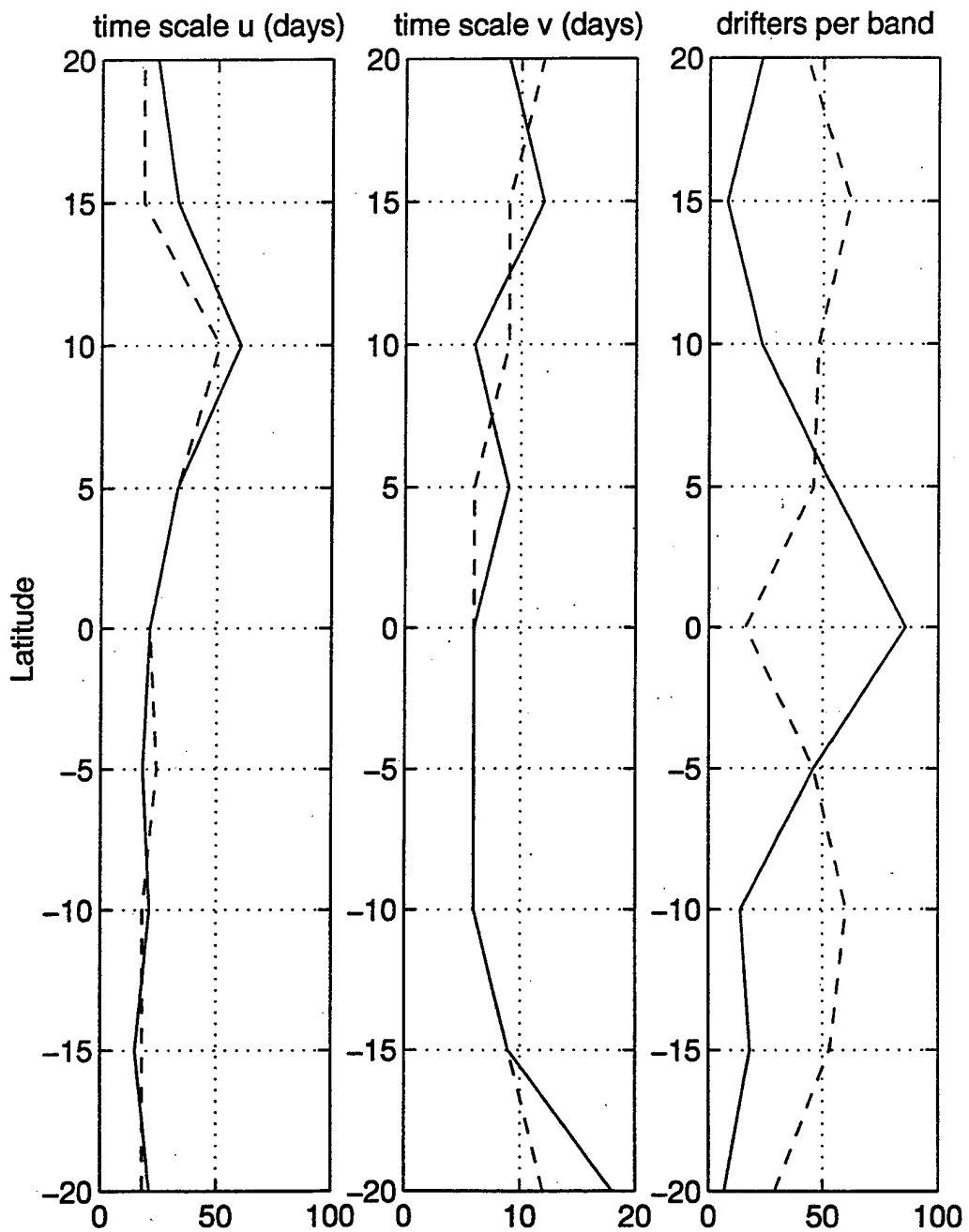


Figure 41. Meridional profiles of zonally averaged uniform (dashed line) and non-uniform (solid line) time scales.

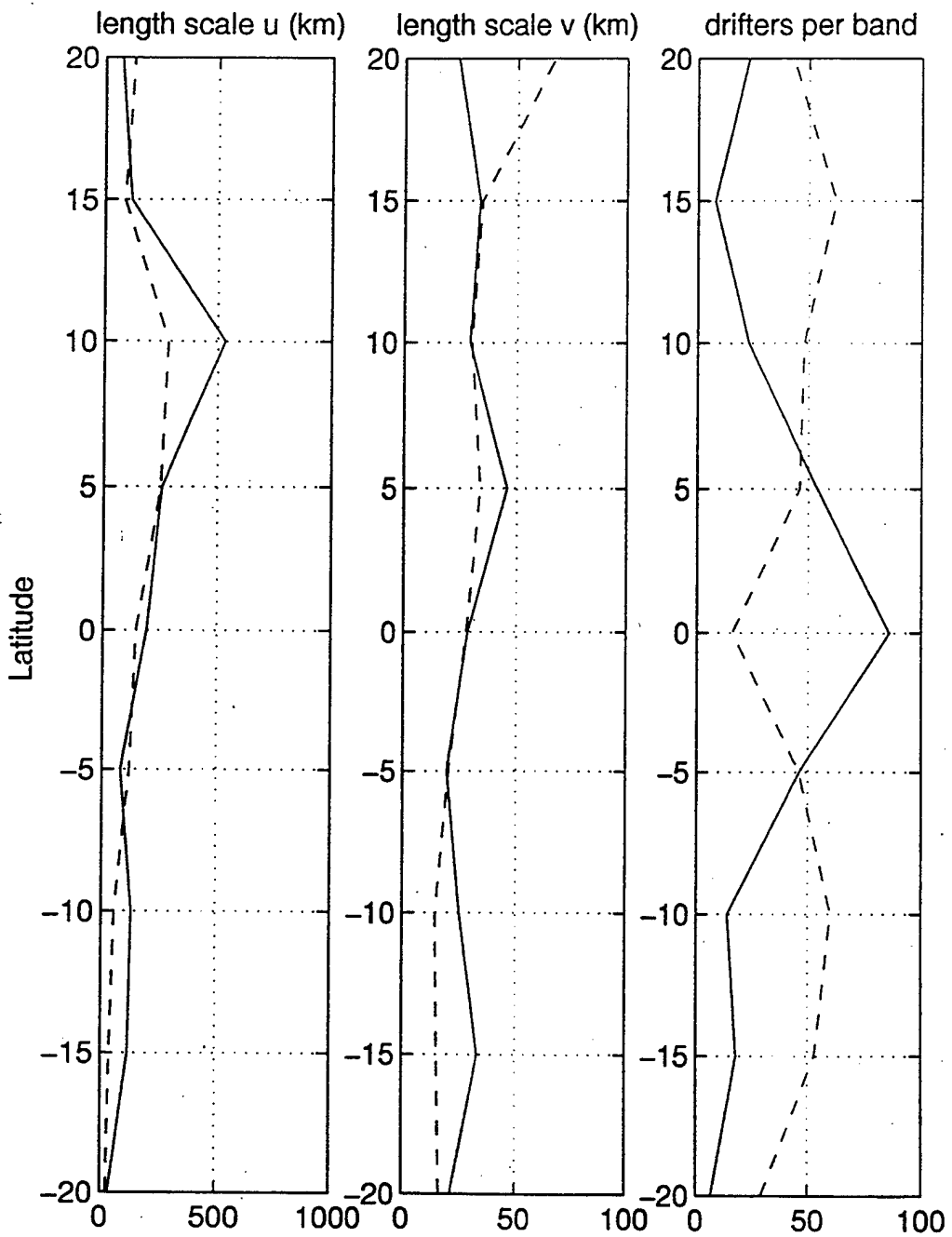


Figure 42. Meridional profiles of zonally averaged uniform (dashed line) and non-uniform (solid line) length scales.

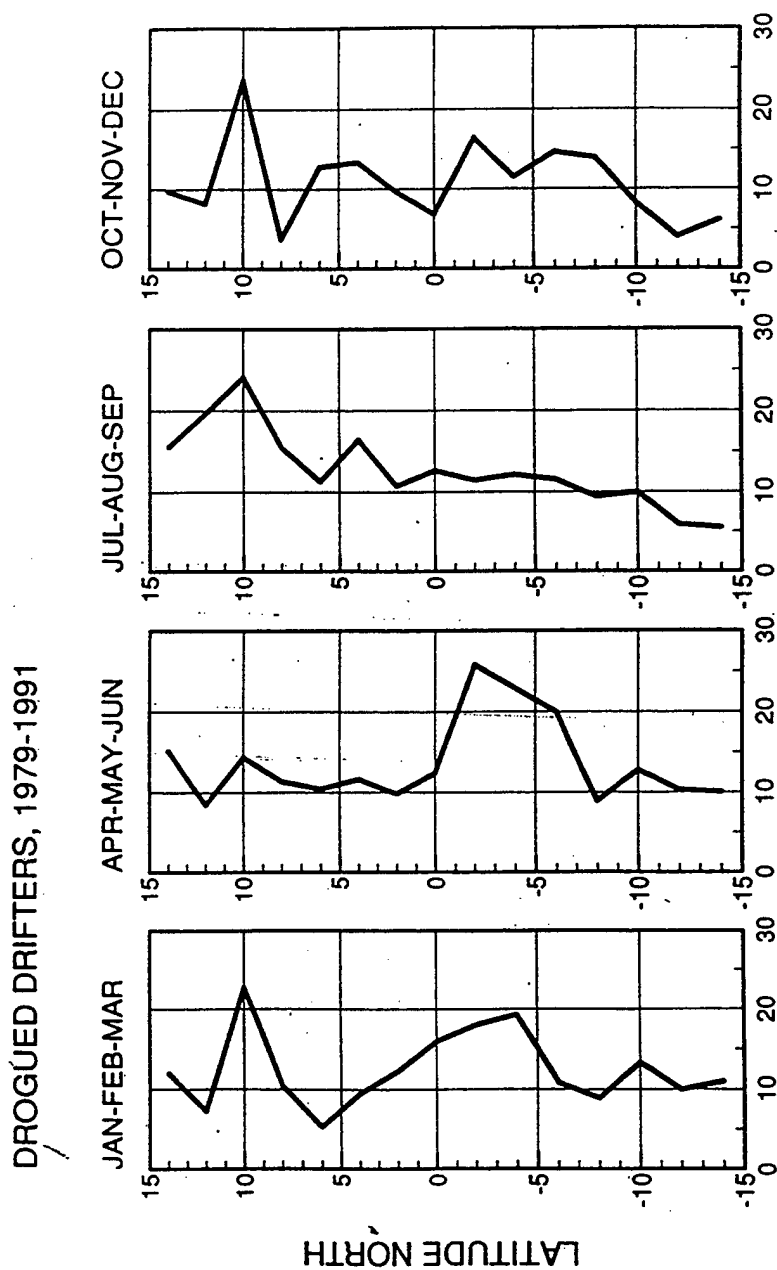


Figure 43. Zonal integral time scale  $T_{uu}$  (days) from drifter trajectories as a function of latitude ( $90^{\circ}\text{W}$  to  $160^{\circ}\text{W}$  at a resolution of  $2^{\circ}$  latitude) for the four seasons of the year. (P. Poulain, personal communication).

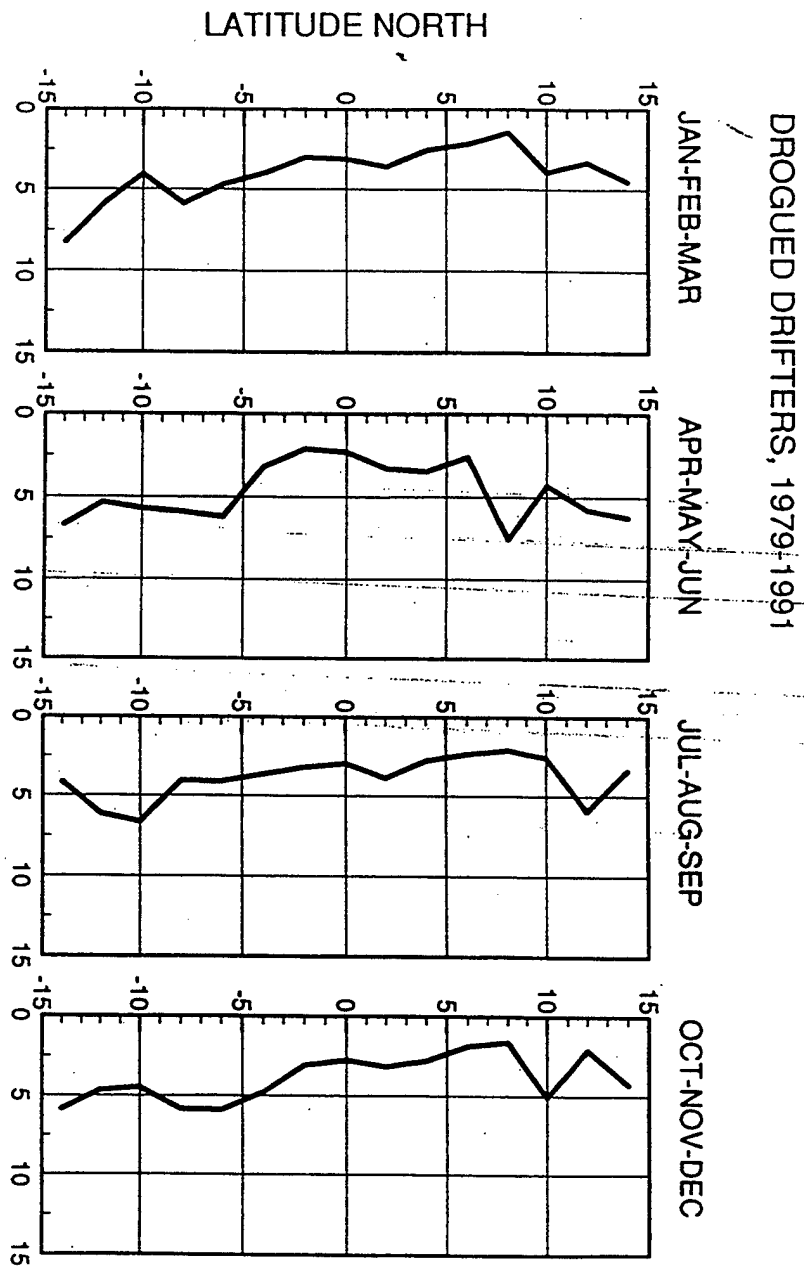


Figure 44. Meridional integral time scale  $T_{vv}$  (days) from drifter trajectories as a function of latitude ( $90^{\circ}\text{W}$  to  $160^{\circ}\text{W}$  at a resolution of  $2^{\circ}$  latitude) for the four seasons of the year. (P. Poulain, personal communication).

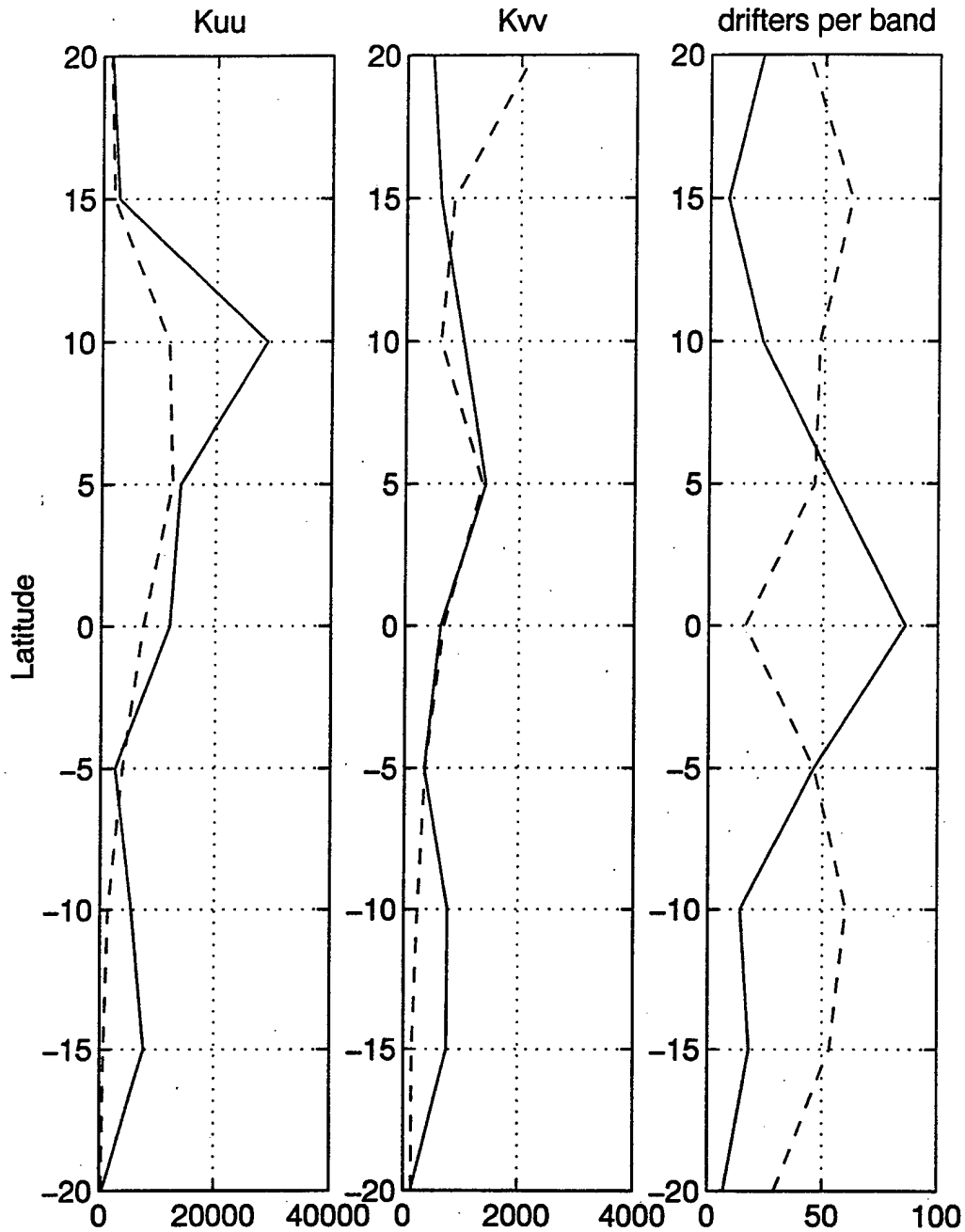


Figure 45. Meridional profiles of zonally averaged uniform (dashed line) and non-uniform (solid line) diffusivity ( $m^2 s^{-1}$ ), and number of drifters per zonal band.

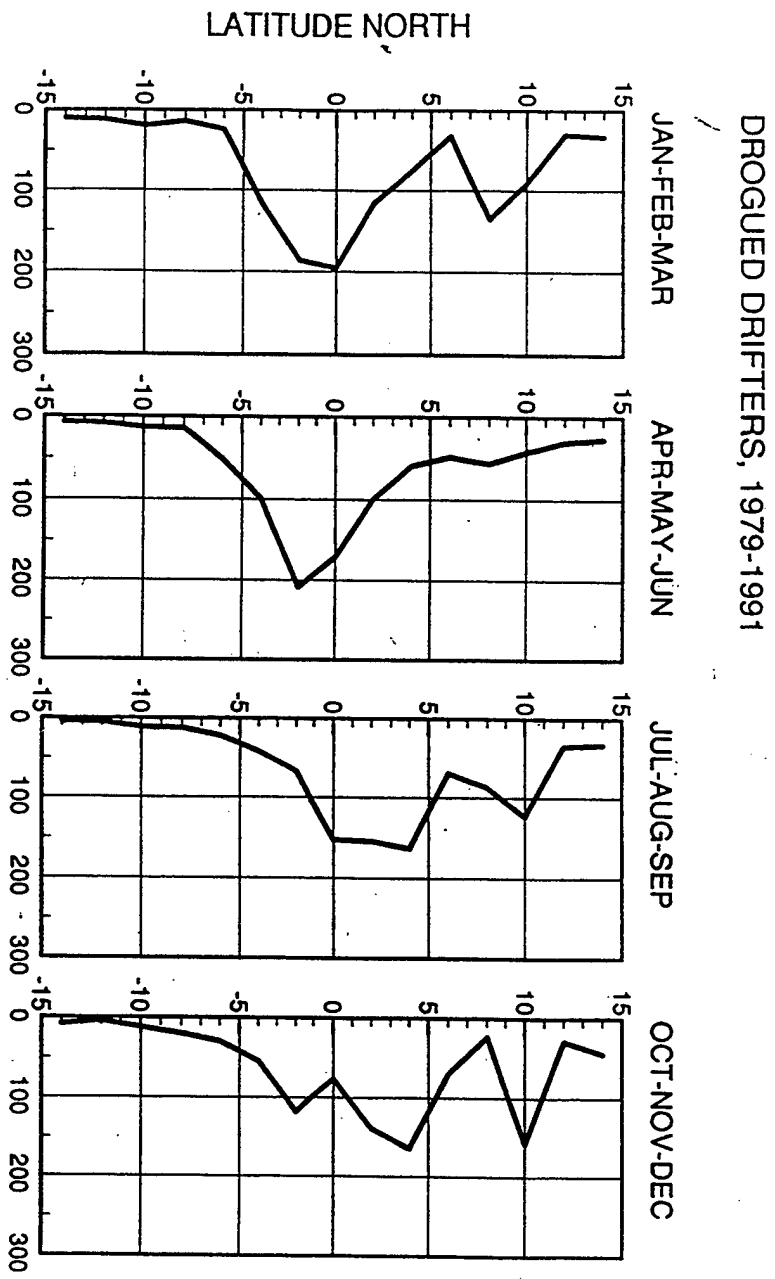


Figure 46. Zonal diffusivity  $K_{uu}$  ( $10^3 \text{ m}^2 \text{ s}^{-1}$ ) from drifter trajectories as a function of latitude ( $90^\circ\text{W}$  to  $160^\circ\text{W}$  at a resolution of  $2^\circ$  latitude) for the four seasons of the year. (P. Poulain, personal communication).

DROGUED DRIFTERS, 1979-1991

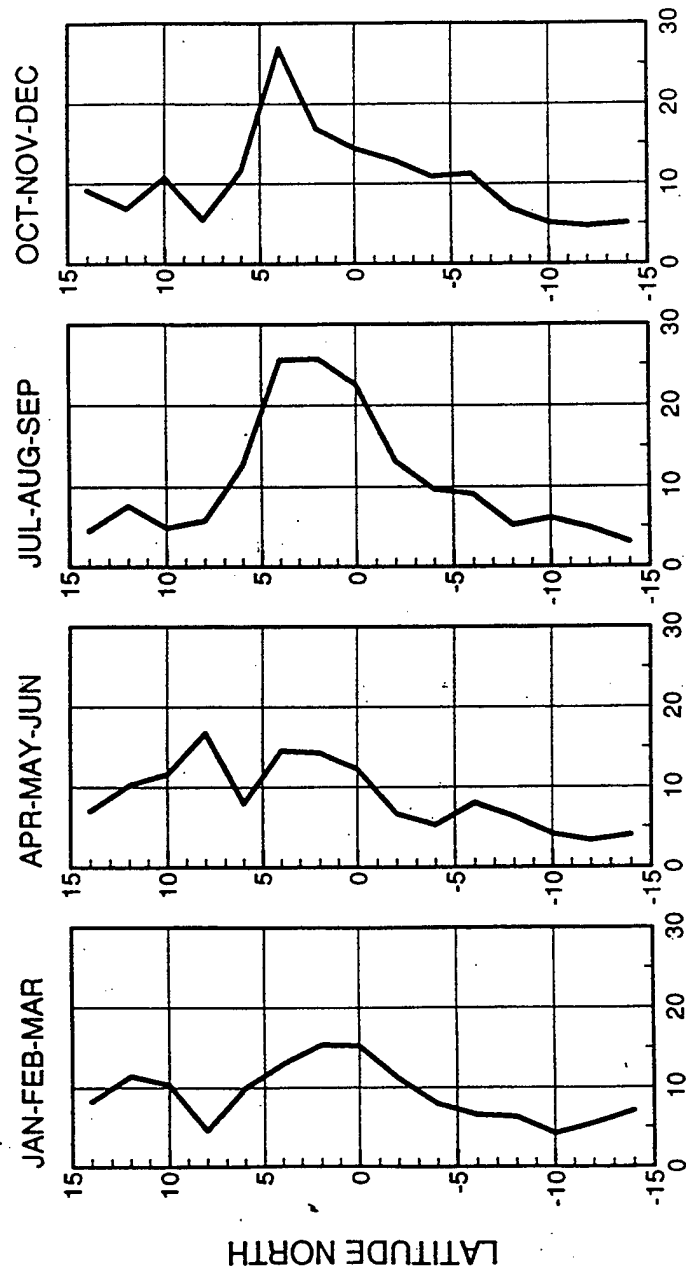


Figure 47. Meridional diffusivity  $K_{VV}$  ( $10^4 \text{ m}^2 \text{ s}^{-1}$ ) from drifter trajectories as a function of latitude ( $90^\circ\text{W}$  to  $160^\circ\text{W}$  at a resolution of  $2^\circ$  latitude) for the four seasons of the year. (P. Poulain, personal communication).

UNIFORM Model Field	Diffusivity		Time Scale		Length Scale	
	K11 (m <sup>2</sup> s <sup>-1</sup> )	K22 (m <sup>2</sup> s <sup>-1</sup> )	U (days)	V (days)	U (km)	V (km)
22.5°N to 17.5°N	1469 <b>1378</b> 1318	1574 <b>2211</b> 2162	6 <b>18</b> 36	6 <b>12</b> 15	43.4 <b>130.2</b> 260.4	33.4 <b>66.9</b> 83.6
17.5°N to 12.5°N	1527 <b>2044</b> 1794	670 <b>844</b> 935	9 <b>18</b> 42	6 <b>9</b> 15	44.6 <b>89.2</b> 208.2	23.0 <b>34.5</b> 57.5
12.5°N to 7.5°N	5209 <b>11766</b> 16395	506 <b>618</b> 676	18 <b>51</b> 87	6 <b>9</b> 12	100.2 <b>283.8</b> 484.1	19.9 <b>29.9</b> 39.8
7.5°N to 2.5°N	3341 <b>12428</b> 18698	854 <b>1356</b> 1725	6 <b>33</b> 66	3 <b>6</b> 12	46.1 <b>253.4</b> 506.8	16.9 <b>33.9</b> 67.8
2.5°N to 2.5°S	2704 <b>7441</b> 11490	513 <b>691</b> 691	6 <b>21</b> 45	3 <b>6</b> 6	42.2 <b>147.7</b> 316.5	13.9 <b>27.7</b> 27.7
2.5°S to 7.5°S	1909 <b>3850</b> 5741	265 <b>363</b> 363	9 <b>24</b> 51	3 <b>6</b> 9	45.3 <b>120.8</b> 256.8	10.1 <b>20.2</b> 30.2
7.5°S to 12.5°S	557 <b>1360</b> 3022	151 <b>238</b> 311	6 <b>18</b> 60	3 <b>6</b> 15	18.7 <b>56.1</b> 186.9	7.2 <b>14.4</b> 36.0
12.5°S to 17.5°S	355 <b>635</b> 1367	67 <b>145</b> 172	9 <b>18</b> 57	3 <b>9</b> 12	19.0 <b>38.0</b> 120.3	5.1 <b>15.2</b> 20.3
17.5°S to 22.5°S	92 <b>219</b> 371	82 <b>134</b> 188	6 <b>18</b> 45	6 <b>12</b> 21	8.1 <b>24.2</b> 60.4	8.1 <b>16.2</b> 28.4

Table I. Diffusivity, time and length scales for the uniform drifter distribution by latitudinal bands. Bold values are means, lower and upper values are plus and minus one standard deviation, respectively.

NON-UNIFORM Model Field	Diffusivity		Time Scale		Length Scale	
Latitude Band	K11 (m <sup>2</sup> s <sup>-1</sup> )	K22 (m <sup>2</sup> s <sup>-1</sup> )	U (days)	V (days)	U (km)	V (km)
22.5°N to 17.5°N	539 <b>1610</b> 2354	351 <b>456</b> 597	6 <b>24</b> 42	6 <b>9</b> 21	18.7 <b>74.6</b> 130.6	15.8 <b>23.7</b> 55.2
17.5°N to 12.5°N	1621 <b>2899</b> 4868	368 <b>604</b> 1111	15 <b>33</b> 75	6 <b>12</b> 45	53.4 <b>117.6</b> 267.2	16.7 <b>33.4</b> 125.2
12.5°N to 7.5°N	15734 <b>28869</b> 33240	1007 <b>1007</b> 1151	24 <b>60</b> 87	6 <b>6</b> 9	213.3 <b>533.3</b> 773.3	29.0 <b>29.0</b> 43.6
7.5°N to 2.5°N	7661 <b>13805</b> 20630	1151 <b>1416</b> 1635	15 <b>33</b> 66	6 <b>9</b> 15	117.5 <b>258.6</b> 517.1	30.6 <b>45.8</b> 76.4
2.5°N to 2.5°S	6693 <b>12073</b> 15905	512 <b>634</b> 634	9 <b>21</b> 36	3 <b>6</b> 6	83.0 <b>193.8</b> 332.2	14.2 <b>28.3</b> 28.3
2.5°S to 7.5°S	1561 <b>2545</b> 4162	350 <b>350</b> 364	9 <b>18</b> 39	6 <b>6</b> 9	41.2 <b>82.5</b> 178.7	19.4 <b>19.4</b> 29.1
7.5°S to 12.5°S	2178 <b>5499</b> 7987	774 <b>774</b> 2374	6 <b>21</b> 48	6 <b>6</b> 30	37.9 <b>132.8</b> 303.5	25.1 <b>25.1</b> 125.6
12.5°S to 17.5°S	1962 <b>7698</b> 11767	367 <b>757</b> 1037	3 <b>15</b> 30	3 <b>9</b> 15	23.8 <b>119.1</b> 238.2	11.1 <b>33.3</b> 55.5
17.5°S to 22.5°S	361 <b>414</b> 797	36 <b>126</b> 211	18 <b>21</b> 54	3 <b>18</b> 36	28.8 <b>33.6</b> 86.4	3.5 <b>21.2</b> 42.4

Table II. Diffusivity, time and length scales for the non-uniform drifter distribution by latitudinal bands. Bold values are means, lower and upper values are plus and minus one standard deviation, respectively.



## VI. CONCLUSIONS AND RECOMMENDATIONS

### A. CONCLUSIONS

The results of the present study have underscored the complementary use of drifter observations and numerical simulations for studying ocean circulation. Model successes can be attributed to very realistic physics and forcing at high resolution. The model simulates the mean surface circulation of the tropical Pacific quite well, as evidenced by the mean Eulerian velocity fields, reproducing observed flow patterns. The discrepancies are typically in magnitudes, primarily in the equatorial regions.

The model mean values exceed the observed values by as much as 50% in the equatorial region (Figures 9 and 10). The higher model mean values occur probably as a result of a lack of a mixed layer. Since the model is solely dependent on the Richardson-number formulation of Pacanowski and Philander (1981) for the vertical transfer of momentum and tracers, the Ekman drift is largely trapped in the upper layer, producing an artificially strong flow. The unrealistic representation of the SECC may be due to an inadequate representation of wind forcing.

Model variability (Figures 13 - 16) is about 20% less than the observed data in equatorial regions, and 50% less than the observed data poleward of 10°S and 10°N. The model

is not able to completely simulate variability in part due to a lack of an appropriate parameterization of mixed layer physics. The westward displacement of zonal variability maxima (Figure 13) may be due to inadequate representation of ECMWF winds in the western Pacific. Insufficient representation of variability has also been attributed to deficiencies in simulating the mean structure of the density field (Beckmann et al., 1994), which can inhibit the generation of barotropic / baroclinic instabilities, associated with the horizontal and vertical shear of zonal currents. Applying the 9-day running mean to the temperature field, for consistency with the velocity data, further reduced the temperature variability (Figure 16).

Relative vorticity (Figure 18) and divergence (Figure 19) are dominated by  $\partial\langle u \rangle / \partial y$  and  $\partial\langle v \rangle / \partial y$ , respectively; therefore, the structure of these fields reflects the distribution of the respective dominant mean flow component. The generally higher mean velocity values from the model output, compared to drifter data, also translates to higher divergence and relative vorticity values, relative to observations.

Both model- and drifter-based fields of  $u$  and  $v$  covariance (Figure 19) show generally negative values north of the equator and positive values south of the equator. The strong gradients in the eastern equatorial region, particularly in the north, are attributed to instability

waves. The covariance of velocity and SST (Figure 20) indicates convergence of heat toward the equator, with the strongest values just north of the equator, most likely from 20-30 day instability waves. The model extends the strong equatorial fluxes farther west and more symmetrically about the equator.

In comparing the Lagrangian results of the uniform distribution of model trajectories to observed values, model-based time scales are too slow by as much as a factor of 2, the length scales are as much as four times higher than observed values in the equatorial region (Reverdin et al., 1994; Hansen and Paul, 1984), and the diffusivities are too low by an order of magnitude. These differences can be attributed in part to the lack of model energy and to the overly large spatial scales used in the Lagrangian analyses. The results of the uniform and non-uniform sampling strategies used here show good agreement between diffusivities, length, and time scales; but this is misleading, since the latitude bands used to group the mean drifter positions for statistical analysis cover such a large, non-localized meridional scale and span different current regimes.

The low variability, longer spatial scales, low diffusivities, and longer time scales relative to observed values indicate that the model fields are missing high frequency processes. This is certainly due in part to the

form of the wind forcing (3-day averages of daily ECMWF fields interpolated onto the model grid from a 2.5° x 2.5° grid) and the use of the 9-day running average in addition to any real lack of mesoscale activity in the model.

## **B. RECOMMENDATIONS**

The most prominent model weaknesses are weak variability, as much as half of that in the observed data and excessive mean flows. This is a result of a combination of no surface mixed layer, lack of real heat and freshwater fluxes, too coarse of a grid resolution, and possibly a result of inadequate representation of wind forcing. The use of weighted model means, proportional to the number of drifter observations per latitude band, would remove some ambiguity in the interpretation of differences between model- and drifter-based statistics. Incorporation of a surface mixed layer would allow the model to achieve an exchange of momentum, heat, and freshwater between the ocean and atmosphere (represented here by the surface forcing), and is likely to be necessary to correctly simulate the observed seasonal cycles in velocity and SST (Stammer et al., 1996). (The most current POP version has implemented a mixed layer formulation known as the "K-profile parameterization" (KPP).)

Using real heat flux and evaporation - precipitation (E-P) values, i. e., ECMWF analysis and re-analysis, would allow

better simulation of the variability of thermohaline forcing, especially the annual cycle. Maltrud et al. (1997) state that more realistic surface currents and heat transport occur when the model is driven by heat and freshwater fluxes, rather than when it is restored to temperature and salinity climatology.

Finer grid resolution would allow better representation of points of separation by currents from coastlines, more accurate transports through narrow passages, and better realization of the baroclinic / barotropic instabilities associated with variability.

Finer grid resolution has been introduced in the North Atlantic POP simulation (M. Maltrud, personal communication), where  $1/10^\circ$  resolution and 37 levels produce very accurate means and variabilities. SSH variability from TOPEX/POSEIDON compares very well with the model output from this higher resolution grid.

The eddy heat flux in the covariance of velocity and SST fields is important for describing the heat balance and SST in the equatorial region. This may be a particularly useful diagnostic when evaluating the model's ability to simulate climate and climate change. The results obtained here point to the cold tongue and the northern instability wave regions in the eastern tropical Pacific as important locations upon which to focus heat budget calculations. A detailed heat budget of this region is needed to understand and balance the

equatorial cooling, induced by the divergent Ekman transport, against the equatorward heat flux by mesoscale eddies.

As is the case for the Eulerian comparisons described in this study, the Lagrangian statistics computed from model-derived trajectories also point to focus areas for further comparisons and model development.

Lagrangian time scales from the model trajectories are longer than observed and the diffusivities are smaller than observed. Since different techniques were used to determine the time scales in this study (e-folding times) versus studies based on the drifter data (zero crossing times), systematic differences are expected in these integral quantities. However, the expected bias between these two methods is for shorter time scales from the e-folding method, not longer time scales as this study found. More detailed computations of Lagrangian statistics are needed to verify these differences. On the model side, shorter trajectories with durations on the order of several integral time scales (a few months) should be used rather than the two-year long trajectories in this study. In this way, more trajectories would be available for ensembling and their mean positions would be more representative of the regional ensemble to which they were assigned. On the data side, combined global statistics should be computed for comparison with the model results rather than the separate seasonal statistics provide by Poulain (personal communication) for this study.

A great strength of the Lagrangian methods applied to model velocity fields is the ability to control the sampling strategy. More should be done to exploit this strength using shorter trajectories that will better highlight the differences between uniform and non-uniform deployments. This sampling flexibility is also ideal for the investigation of the effects of shear in the mean flow on the computation of Lagrangian quantities like integral time scales and diffusivities (Bauer et al., 1997) as well as Eulerian properties like velocity and divergence (Poulain, 1993) and mixed sampling problems like the array bias of mean current estimates due to non-uniform concentrations in the presence of diffusion (Davis et al., 1996).



## APPENDIX. RUNGE-KUTTA METHOD OF TRAJECTORY GENERATION

In this study we consider an initial value problem which consists of a first-order differential equation and a condition which the solution must satisfy (Nakamura 1991; Kreyszig 1986):

$$y' = f(y, t), \quad y(0) = y_0.$$

The estimate  $y_{n+1}$  at  $t_{n+1} = t_n + h$  with a known value of  $y_n$ , may be obtained by integrating over the interval  $[t_n, t_{n+1}]$ :

$$y_{n+1} = y_n + \int_{t_n}^{t_{n+1}} f(y, t) dt.$$

Following Press et al. (1992):

A practical method for solving initial value problems is the Runge-Kutta (RK) method, which propagates a solution over an interval by combining the information from several Euler-style steps (each involving one evaluation of the right hand  $f$ 's), and then using the information to match a Taylor's series expansion up to some higher order.

The formula for the Euler method is

$$y_{n+1} = y_n + hf(x_n, y_n).$$

which advances a solution from  $x_n$  to  $x_{n+1} = x_{n+h}$ . The practical value of the Euler method is limited, however, since it advances a solution through an interval  $h$ , but uses derivative information only at the beginning of that interval (Figure 48). The step's error, therefore, is only one power smaller than the correction, and the method is not as accurate as other methods, or as stable as is usually desired for practical use.

However, the Euler method is useful to take a trial step to the midpoint of an interval. Then the value of both  $x$  and  $y$  at that midpoint is used to compute the step across the interval (Figure

49). This symmetrization cancels out the first-order error term; the method is called the midpoint or second-order Runge-Kutta method.

In RK methods, the order of accuracy is increased by using intermediate points in each step interval  $h$ . Higher accuracy also implies that errors decrease more quickly than in lower-order accuracy methods when the step interval is reduced. The fourth-order RK method requires four evaluations of the right-hand side per step  $h$  (Figure 50), and is accurate to the fourth-order term of the Taylor expansion, so the local error is proportional to  $h^5$ .

For this specific problem, the implementation of the RK method using the simulation velocity field involves

$$x_{new} = x_{old} + u \Delta t, \quad y_{new} = y_{old} + v \Delta t, \quad \Delta t = 6 \text{ days}.$$

Using

$$k_1 = h u(x, y, t), \quad l_1 = h v(x, y, t)$$

$$k_2 = h u\left(x_n + \frac{k_1}{2}, y_n + \frac{l_1}{2}, t_n + \frac{h}{2}\right), \quad l_2 = h v\left(x_n + \frac{k_1}{2}, y_n + \frac{l_1}{2}, t_n + \frac{h}{2}\right)$$

$$k_3 = h u\left(x_n + \frac{k_2}{2}, y_n + \frac{l_2}{2}, t_n + \frac{h}{2}\right), \quad l_3 = h v\left(x_n + \frac{k_2}{2}, y_n + \frac{l_2}{2}, t_n + \frac{h}{2}\right)$$

$$k_4 = h u(x_n + k_3, y_n + l_3, t_n + h), \quad l_4 = h v(x_n + k_3, y_n + l_3, t_n + h)$$

the two-dimensional trajectories of the simulated drifters are computed using the fourth-order RK scheme, where  $x_{n+1}$  represents the new location of a particle that is advected

from a previous position  $x_n$ , by the velocity  $u$  or  $v$ , in a time interval  $\Delta t$ , and  $k_i$  and  $l_i$  represents the RK coefficients.

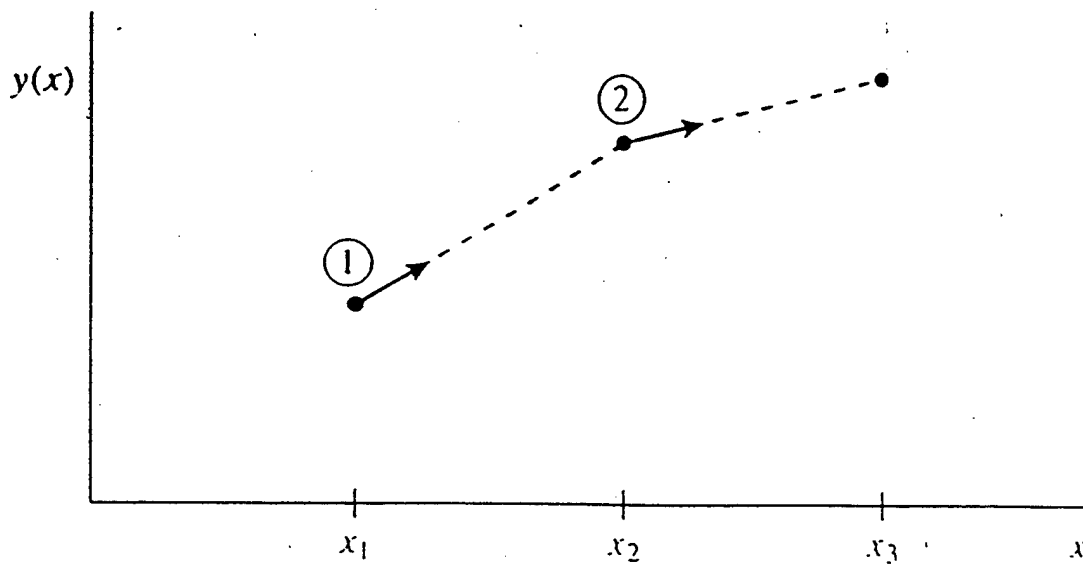


Figure 48. Euler's method. In this simplest (and least accurate) method for integrating an ODE, the derivative at the starting point of each interval is extrapolated to the next function value. The method has first-order accuracy. Figure 16.1.1 from Press et al., 1996.

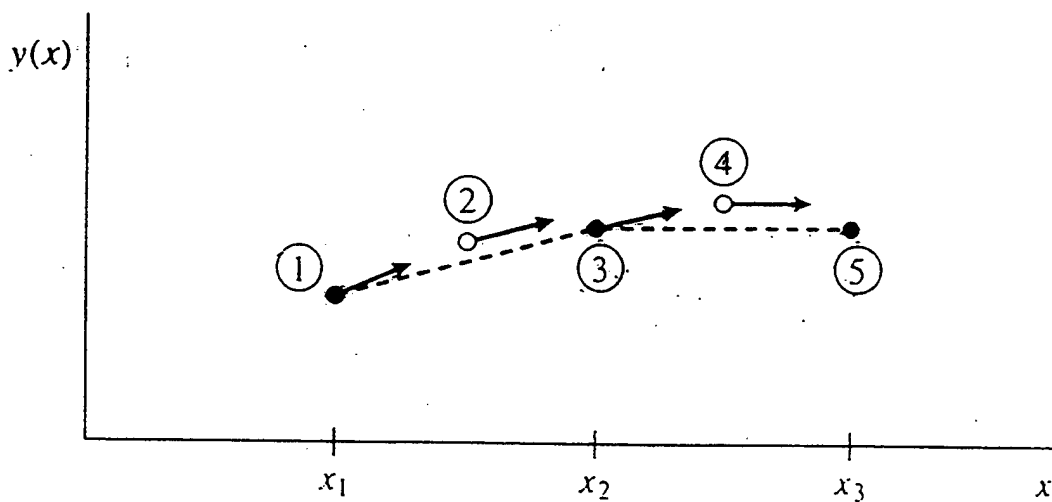


Figure 49. Midpoint method. Second-order accuracy is obtained by using the initial derivative at each step to find a point halfway across the interval, then using the midpoint derivative across the full width of the interval. In the figure, filled dots represent final function values, while open dots represent function values that are discarded once their derivatives have been calculated and used. Figure 16.1.2 from Press et al., 1996.

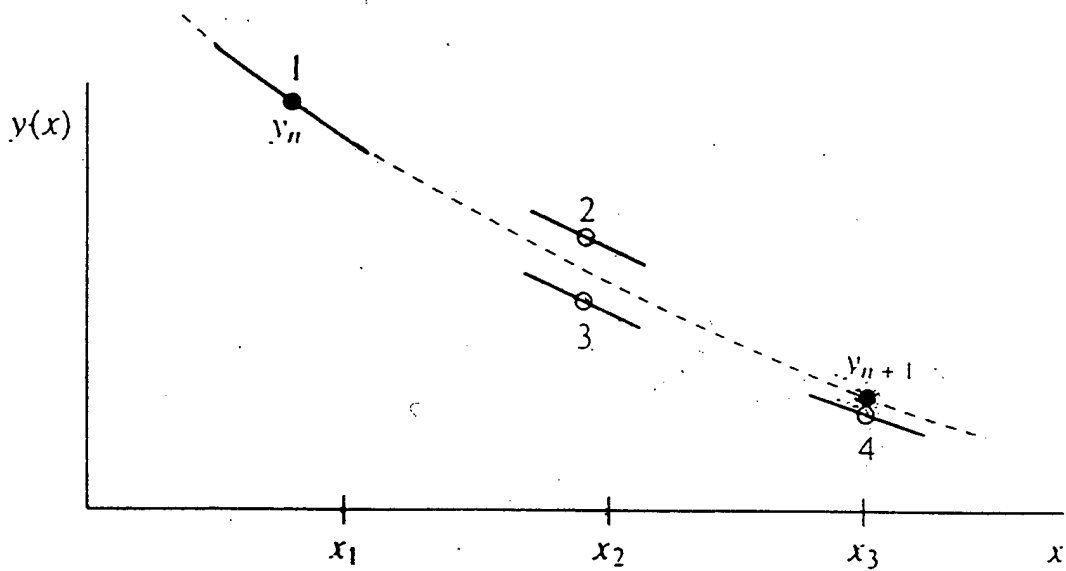


Figure 50. Fourth-order Runge-Kutta method. In each step the derivative is evaluated four times: once at the initial point, twice at trial midpoints, and once at a trial endpoint. From these derivatives the final function value (shown as a filled dot) is calculated. Figure 16.1.3 from Press et al., 1996.

## LIST OF REFERENCES

- Apel, J., 1987: *Principles of Ocean Circulation Physics*. Academic Press, San Diego. 634 pp.
- Bauer, S., M. Swenson, A. Griffa, A. Marianao, and K. Owens, 1997: Eddy-mean flow decomposition and eddy-diffusivity estimates in the tropical Pacific Ocean, *J. Geophys. Res.*, Submitted.
- Bearman, G., 1995: *Ocean Circulation*. Pergamon Press, Exeter, Great Britain. 238 pp.
- Beckmann, A., C. Bonong, B. Brugge, and D. Stammer, 1994: On the generation and role of eddy variability in the central North Atlantic Ocean, *J. Geophys. Res.*, **99**, 20381-20391.
- Bleck, R. and D. Boudra, 1986: Wind-driven spin-up in eddy-resolving ocean models formulated in isopycnic and isobaric coordinates, *J. Geophys. Res.*, **91**, 7611-7632.
- Bryan, K., 1969: A numerical method for the study of the circulation of the world ocean, *J. Comp. Physics*, **4**, 347-376.
- Bryan F., C. Boning, and W. Holland, 1995: On the midlatitude circulation in a high-resolution model of the North Atlantic, *J. Phys. Oceanogr.*, **25**, 289-305.
- Chatfield, C., 1996: *The Analysis of Time Series: An Introduction*. Chapman and Hall, London. 283 pp.
- Cox, M., 1970: A mathematical model of the Indian Ocean, *Deep-sea Res.*, **17**, 45-75.
- Cox, M., 1984: A primitive equation three dimensional model of the ocean. GFDL Ocean Group Technical Report No. 1, Geophysical Fluid Dynamics Laboratory / NOAA, 250 pp.
- Davis, R., 1991, Describing the general circulation with floats, *Deep-sea Res. Part A*, **38**, S531-S571.
- Davis, R., P. Killworth, and J. Blundell, 1996: Comparison of autonomous Lagrangian circulation explorer and fine resolution Antarctic model results in the south Atlantic, *J. Geophys. Res.*, **101**, 855-884.
- Dukowicz, J., and R. Smith, 1994: Implicit free-surface method for the Bryan-Cox-Semtner ocean model, *J. Geophys. Res.*, **99**, 7991-8014.
- Fieux, M., C. Andrie, P. Delecluse, A. Ilahude, A. Kartavtseff, F. Mantsi, R. Molcard, and J. Swallow, 1994: Measurements within the Pacific-Indian oceans throughflow region, *Deep-sea Res.*, **41**, 1091-1130.
- Freeland, H., P. Rhines, and T. Rossby, 1975: Statistical observations of the trajectories of neutrally buoyant floats in the North Atlantic, *J. Marine Res.*, **33**, 383-404.
- Fu, L., and R. Smith, 1996: Global ocean circulation from satellite altimetry and high-resolution computer simulation, *Bull. Am. Meteorol. Soc.*, **77**, 2625-2636.

- Frankignoul, C., F. Bonjean, and G. Reverdin, 1996: Interannual variability of surface currents in the tropical Pacific during 1987-1993, *J. Geophys. Res.*, **101**, 3629-3647.
- Godfrey, J., A. Hirst, and J. Wilkin, 1993: Why does Indonesian throughflow appear to originate from the North Pacific? *J. Phys. Oceanogr.*, **23**, 1087-1098.
- Hansen, D. V. and C. A. Paul, 1984: Genesis and effects of Long waves in the equatorial Pacific, *J. Geophys. Res.* **89**, 10431-10440.
- Hofmann, E., K. Hedstrom, J. Moisan, D. Haidvogel, and D. Mackas, 1991: Use of simulated drifter tracks to investigate general transport patterns and residence times in the coastal transition zone. *J. Geophys. Res.* **96**, 15041-15052.
- Hurlburt, H., A. Wallcraft, Z. Sirkes, and E. Metzger, 1992: Modeling of the Global and Pacific Oceans: On the path to eddy-resolving ocean prediction, *Oceanography* **5**, 9-18.
- Jayne, S., and R. Tokmakian, 1997: Forcing and sampling of ocean general circulation models: impact of high frequency motions, *J. Phys. Oceanogr.*, Submitted.
- Kreyszig, E., 1986: *Advanced Engineering Mathematics*, John Wiley & Sons, New York. 988 pp.
- Levitus, S., 1982: *Climatological Atlas of the World Ocean*, NOAA Professional Paper 13, U. S. Govt. Printing Office. 173 pp.
- Lukas, R. 1987: Horizontal Reynolds stresses in the central equatorial Pacific, *J. Geophys. Res.*, **92**, 9453-9463.
- Luther, D., and E. Johnson, 1990: Eddy energetics in the upper equatorial Pacific during the Hawaii-to-Tahiti Shuttle Experiment. *J. Phys. Oceanogr.*, **20**, 913-944.
- Maltrud, M., R. Smith, A. Semtner, and R. Malone, 1997: Global eddy-resolving ocean simulations driven by 1985-1994 atmospheric winds, *J. Geophys. Res.*, Submitted.
- McClellan, J., A. Semtner, and V. Zlotnicki, 1996: Mesoscale variability in the Semtner-Chervin 1/4° model, the LANL POP 1/6° model, and the TOPEX/POSEIDON data, *J. Geophys. Res.*, In Press.
- McNally, G., 1981: Satellite-tracked drift buoy observations of the near-surface flow in the eastern mid-latitude North Pacific, *J. Geophys. Res.*, **86**, 8022-8030.
- McNally, G. and W. Patzert, A. Kirwan, and A. Vastano, 1983: The near-surface circulation of the North Pacific using satellite-tracked drifting buoys, *J. Geophys. Res.*, **88**, 7507-7518.
- McPhaden, M., 1993: TOGA-TAO and the 1991-93 El Nino-Southern Oscillation Event, *Oceanography*, **6**, 36-44.
- Nakamura, S., 1991: *Applied Numerical Methods with Software*. Prentice Hall, Englewood Cliffs, NJ. 410 pp.

- Niiler, P., 1995: Global Drifter Program: measurements of velocity, SST, and atmospheric pressure, *International WOCE Newsletter* **20**, 3-6.
- Niiler, P., P. Poulain, and L. Haury, 1989: Synoptic three-dimensional circulation in an onshore-flowing filament of the California Current, *Deep-sea Res.*, **36**, 385-405.
- Niiler, P., D. Hansen, D. Olsen, P. Richardson, Y. DuPenhoat, G. Reverdin, and G. Cresswell, 1997: The pan-Pacific current study Lagrangian drifter measurements: 1988-1994, *J. Geophys. Res.*, Submitted.
- Pacanowski, R. and S. Philander, 1981: Parameterization of vertical mixing in numerical models of tropical ocean, *J. Phys. Oceanogr.* **11**, 1443-1451.
- Paduan, J. and P. Niiler, 1993: Structure of velocity and temperature in the northeast Pacific as measured with Lagrangian drifters in Fall 1987, *J. Phys. Oceanogr.*, **23**, 585-600.
- Pedlosky, J., 1996: *Ocean Circulation Theory*. Springer-Verlag, Berlin. 453 pp.
- Perigaud, C., 1990: Sea level oscillations observed with Geosat along the two shear fronts of the Pacific North Equatorial Current, *J. Geophys. Res.* **95**, 7329-7248.
- Philander, S., 1990: *El Nino, La Nina, and the Southern Oscillation*, Academic Press, San Diego. 293 pp.
- Philander, S., W. Hurlin, and R. Pacanowski, 1986: Properties of long equatorial waves in models of the seasonal cycle in the tropical Atlantic and Pacific oceans, *J. Geophys. Res.*, **91**, 14207-14211.
- Poulain, P., 1993: Estimates of horizontal divergence and vertical velocity in the equatorial Pacific, *J. Phys. Oceanogr.*, **23**, 601-607.
- Poulain, P., and P. Niiler, 1989: Statistical analysis of the surface-circulation in the California Current System using satellite tracked drifters, *J. Phys. Oceanogr.* **19**, 1588-1603.
- Press, W., S. Teukolsky, W. Vetterling, and B. Flannery, 1992: *Numerical Recipes in Fortran 77*, Cambridge University Press, London. 933 pp.
- Ralph, E., and P. Niiler. 1995: Lagrangian measurements of the mean wind-driven currents in the tropical Pacific, *International WOCE Newsletter*, **20**, 7-9.
- Reverdin, G., C. Frankignoul, E. Kestenare, and M. McPhaden, 1994: Seasonal variability in the surface currents of the equatorial Pacific, *J. Geophys. Res.*, **99**, 20323-20344.
- Richardson, P. 1983. Eddy kinetic energy in the North Atlantic from surface drifters. *J. Geophys. Res.*, **88**, 4355-4367.
- Semtner, A., 1974: An oceanic general circulation model with bottom topography. Tech. Report 9, Dept. Of Meteorology, Univ. Of Cal., Los Angeles. 99 pp.

- Semtner, A., 1997: Very high-resolution estimates of global ocean circulation, suitable for carbon-cycle modeling, *Proceedings of the 1993 Snowmass Global Change Institute on the Global Carbon Cycle*, T. Wigley, ed., Cambridge Univ. Press., 217 pp.
- Semtner, A., and R. Chervin, 1988: A simulation of the global ocean circulation with resolved eddies, *J. Geophys. Res.*, **93**, 15505-15522.
- Semtner, A., and R. Chervin, 1992: Ocean general circulation from a global eddy-resolving model, *J. Geophys. Res.*, **97**, 5493-5550.
- Smith, R., J. Doukowicz, and R. Malone, 1992: Parallel ocean general circulation modeling, *Physica D*, **60**, 38-61.
- Stammer, D., R. Tokmakian, A. Semtner, and C. Wunsch, 1996: How well does a  $1/4^\circ$  global circulation model simulate large-scale oceanic observations? *J. Geophys. Res.*, **101**, 25779-25811.
- Sybrandy, A. and P. Niiler, 1991: The WOCE/TOGA SVP Lagrangian drifter construction manual. SIO Ref. 91/6, WOCE Report No. 63/91, 58 pp.
- Tomczak, M, and J. Godfrey, 1994: *Regional Oceanography: an Introduction*. Pergamon Press, Tarrytown, NY. 422 pp.
- Yang, Y., T. Tang, and R. Weisberg, 1997: Basin-wide zonal wind stress and ocean thermal variations in the equatorial Pacific Ocean, *J. Geophys. Res.* **102**, 911-927.

INITIAL DISTRIBUTION LIST

	No. Copies
1. Defense Technical Information Center.....2 8725 John J. Kingman Rd., Ste 0944 Cameron Station Ft. Belvoir, VA 22060-6218	
2. Dudley Knox Library.....2 Naval Postgraduate School 411 Dyer Rd. Monterey, CA 93943-5101	
3. Superintendent.....1 Attn: Chairman, Department of Oceanography Code OC/BF Naval Postgraduate School Monterey, CA 93943-5000	
4. Superintendent.....1 Attn: Assistant Professor J. L. McClean Code OC/Mn Naval Postgraduate School Monterey, CA 93943-5000	
5. Superintendent.....1 Attn: Assistant Professor J. D. Paduan Code OC/Pd Naval Postgraduate School Monterey, CA 93943-5000	
6. Superintendent.....1 Attn: Assistant Professor P. M. Poulain Code OC/Pn Naval Postgraduate School Monterey, CA 93943-5000	
7. Superintendent.....1 Attn: Professor A. J. Semtner, Jr. Code OC/Se Naval Postgraduate School Monterey, CA 93943-5000	
8. Superintendent.....1 Attn: Dr. R. Tokmakian Code OC/Tk Naval Postgraduate School Monterey, CA 93943-5000	

- 9. Professor Pearn P. Niiler.....1  
Code 0230, Scripps Institution of Oceanography  
University of California, San Diego  
La Jolla, CA 92093-0230
  
- 10. Dr. Mathew Maltrud.....1  
MS B216  
Los Alamos National Laboratory  
Los Alamos, NM 87545
  
- 11. NOAA Library.....1  
7600 Sand Point Way N.E.  
Seattle, WA 98115